University of Southern Queensland
Faculty of Engineering & Surveying

THE DESIGN AND OPTIMISATION OF A PROTOTYPE SAILPLANE

A dissertation submitted by

Scott Kruger

In fulfilment of the requirements of

ENG4111 and ENG4112 Research Project

towards the degree of

Bachelor of Engineering (Mechanical)

Submitted: November, 2006

Abstract

The science of aerodynamics can be traced back thousands of years to its beginnings, however remarkably, only one human life span separates the first heavier-than-air aircraft flight from the present day. Unfortunately, during this time little information has been released on the design methods of the high performance aircraft that best utilise the aerodynamic theory. The sailplane is one such example.

This thesis seeks to investigate the theoretical foundation of un-powered aircraft design as well as implement computational methods to design and optimise a prototype sailplane based on its aerodynamic efficiency. The investigation considers the influence of a number of important features, including the airfoil, wing planform, fuselage and tail assembly geometries, and the inherent interference between these components. The overall aim of this study is to determine the appropriate combination of these components in order to provide the greatest L/D ratio over a range of intended flight speeds.

The results of the investigation found two possible optimal aircraft configurations. These configurations were each functions of differing geometric parameters and were both considered as valid solutions. It is hoped that the information contained within this thesis will further enhance sailplane design methods and consequently aid to the betterment of the aerodynamic field.

University of Southern Queensland
Faculty of Engineering and Surveying

ENG4111 Research Project Part 1 &
ENG4112 Research Project Part 2

Limitations of Use

The Council of the University of Southern Queensland, its Faculty of Engineering and Surveying, and the staff of the University of Southern Queensland, do not accept any responsibility for the truth, accuracy or completeness of material contained within or associated with this dissertation.

Persons using all or any part of this material do so at their own risk, and not at the risk of the Council of the University of Southern Queensland, its Faculty of Engineering and Surveying or the staff of the University of Southern Queensland.

This dissertation reports an educational exercise and has no purpose or validity beyond this exercise. The sole purpose of the course pair entitled "Research Project" is to contribute to the overall education within the student's chosen degree program. This document, the associated hardware, software, drawings, and other material set out in the associated appendices should not be used for any other purpose; if they are so used, it is entirely at the risk of the user.

Professor R Smith
Dean
Faculty of Engineering and Surveying

Certification

I certify that the ideas, designs and experimental work, results, analyses and conclusions set out in this dissertation are entirely my own effort, except where otherwise indicated and acknowledged.

I further certify that the work is original and has not been previously submitted for assessment in any other course or institution, except where specifically stated.

Scott Kruger

Student Number: W0009941

_____

Signature

_____

Date

Acknowledgements

“If I have seen further, it is by standing on the shoulders of giants.” Isaac Newton, 1676

The author gratefully acknowledges the effort and contribution of his project supervisor, Dr. Ruth Mossad. Her guidance, expertise, and above all her patience in answering any queries pertaining to this thesis have been indispensable.

A special thanks also to my girlfriend, family and friends for their continued encouragement and support throughout this academic undertaking.

Scott Kruger

University of Southern Queensland

October 2006

Contents

ABSTRACT ..... **i**

ACKNOWLEDGEMENTS ..... **iv**

LIST OF FIGURES ..... **viii**

LIST OF TABLES ..... **xii**

NOMENCLATURE ..... **xiii**

GLOSSARY ..... **xv**

CHAPTER 1 ..... **1**

INTRODUCTION

1.1 Introduction *1*
1.2 Background *1*
1.3 Research Purpose *3*
1.4 Research Objectives *4*
1.5 Conclusion *4*

CHAPTER 2 ..... **5**

LITERATURE REVIEW

2.1 Introduction *5*
2.2 Background *5*
2.3 Design Methods *6*
2.4 Conclusion *7*

CHAPTER 3 ..... **8**

BASICS OF AERODYNAMICS

3.1 Inviscid Incompressible Flow *8*
3.2 Lift … *13*
3.3 Induced Drag *17*
3.4 Viscous Effects and Boundary Layers *18*

CHAPTER 4 23

FLIGHT MECHANICS

4.1 Airfoil/Wing Geometry and Aerodynamic Coefficients 23
4.2 Influences of Airfoil/Wing Geometry and Aerodynamic Performance 30
4.3 Flight Performance and Stability 34
4.4 Aeroelasticity 39

CHAPTER 5 40

DESIGN REQUIREMENTS AND OPTIMISATION

5.1 Aerodynamic Design Requirements 40
5.2 Structural Design Requirements 60

CHAPTER 6 65

NUMERICAL ANALYSIS

6.1 Flow Equations 65
6.2 CFD Modelling 67
6.3 CFD Software Selection 68
6.4 XFOIL Overview 69
6.5 Fluent Overview 70
6.6 CFD Analysis 71
6.7 Structural Modelling 78
6.8 COSMOSWorks Overview 78
6.9 Static Analysis 79
6.10 Modal Analysis 81
6.11 Impact Analysis 81

CHAPTER 7 82

RESULTS AND DISCUSSION

7.1 Results Outline 82
7.2 Two-Dimensional 82
7.3 Three-Dimensional 90
7.4 Structural 115

CHAPTER 8 123

CONCLUSION

8.1 Achievement of Objectives 123
8.2 Study Outcomes 123
8.3 Recommendations for Future Work 125
8.4 Conclusion 125

REFERENCES 126

APPENDIX A

PROJECT SPECIFICATION

APPENDIX B

NUMERICAL CALCULATIONS

APPENDIX C

GEOMETRIC DATA

APPENDIX D

2D AERODYNAMIC DATA

APPENDIX E

3D AERODYNAMIC DATA

APPENDIX F

STRUCTURAL ANALYSIS

List of Figures

FIGURE 1.1: HIGH PERFORMANCE SAILPLANE 2
FIGURE 1.2: THERMAL GLIDING 3
FIGURE 3.1: FLOW FIELD NEAR AIRFOIL IN STEADY FLOW 10
FIGURE 3.2: RELATIONSHIP BETWEEN VELOCITY & STATIC PRESSURE 12
FIGURE 3.3: VELOCITY FIELD INDUCED BY 2D VORTEX 13
FIGURE 3.4: CIRCULATION AROUND A SYSTEM OF 2D VORTICES 14
FIGURE 3.5: LIFT PRODUCED BY SUPERPOSITION OF VORTEX SYSTEM 14
FIGURE 3.6: LIFT ON FINITE WING DUE TO CIRCULATION 15
FIGURE 3.7: VORTEX MODEL OF IDEALISED 2D WING 15
FIGURE 3.8: 3D WIND MODELLED WITH TRAILING VORTICES 16
FIGURE 3.9: LOCAL VELOCITY & FORCE VECTORS OF A CROSS SECTIONAL 3D WING 17
FIGURE 3.10: FLOW OVER FLAT PLATE 18
FIGURE 3.11: VELOCITY PROFILES & PARTICLE MOTIONS FOR LAMINAR, TURBULENT AND SEPARATED BOUNDARY LAYERS 19
FIGURE 3.12: BEHAVIOUR OF LAMINAR BOUNDARY LAYER FOR FULL SIZE AIRFOILS UNDER VARIOUS PRESSURE DISTRIBUTIONS AND REYNOLDS NUMBERS 20
FIGURE 3.13: PRESSURE DRAG DUE TO SEPARATION AND FRICTION DRAG DUE TO BOUNDARY LAYER 21
FIGURE 3.14: EFFECT OF SURFACE ROUGHNESS ON LAMINAR & TURBULENT BOUNDARY LAYERS 22
FIGURE 4.1: FORM, CAMBER LINE & GEOMETRY OF AIRFOIL 23
FIGURE 4.2: AIRFOIL GEOMETRIC PARAMETERS 24
FIGURE 4.3: TYPICAL WING PLANFORMS …..... 25
FIGURE 4.4: WING GEOMETRIC PARAMETERS 26
FIGURE 4.5: AERODYNAMIC FORCES & MOMENT ON AIRFOIL 27
FIGURE 4.6: LIFT & DRAG POLARS 28
FIGURE 4.7: AERODYNAMIC CENTRE & ZERO-LIFT MOMENT 28
FIGURE 4.8: LOCATION OF MEAN AERODYNAMIC CHORD 29
FIGURE 4.9: VARIOUS AIRFOILS 30
FIGURE 4.10: INFLUENCE OF THICKNESS ON MAXIMUM LIFT & MINIMUM DRAG COEFFICIENTS 31
FIGURE 4.11: EFFECT OF ASPECT RATIO ON LIFT DISTRIBUTION OVER RECTANGULAR WING 32
FIGURE 4.12: INDUCED DRAG AS A FUNCTION OF ASPECT RATIO 33
FIGURE 4.13: EFFECT OF TAPER RATIO ON LIFT DISTRIBUTION 33
FIGURE 4.14: BALANCE OF FORCES IN TRIMMED FLIGHT 34
FIGURE 4.15: RELATIONSHIP BETWEEN AIRSPEED & LIFT COEFFICIENT FOR VARIOUS WING LOADINGS 35
FIGURE 4.16: EQUILIBRIUM IN UN-ACCELERATED FLIGHT 36
FIGURE 4.17: PHUGOID & SHORT PERIOD MODES 37
FIGURE 4.18: LATERAL STABILITY DEFINITIONS 37
FIGURE 4.19: LOCATION OF AIRCRAFT NEUTRAL POINT AND CG IN STABLE CONFIGURATION 38

FIGURE 5.1: LIFT & DRAG POLARS 41
FIGURE 5.2: DESIRABLE AERODYNAMIC CHARACTERISTICS FOR SAILPLANE AIRFOILS 42
FIGURE 5.3: INDUCED DRAG COEFFICIENT VS. ASPECT RATIO FOR VARYING C_L 43
FIGURE 5.4: PARASITIC DRAG VS. ASPECT RATIO 43
FIGURE 5.5: EFFECT OF ASPECT RATIO & LIFT COEFFICIENT ON DRAG 44
FIGURE 5.6: VARIATIONS OF WING PLANFORMS 45
FIGURE 5.7: EFFECT OF SPAN, ASPECT RATIO & WING LOADING ON AVERAGE CROSS-COUNTRY SPEED 46
FIGURE 5.8: AVERAGE CROSS-COUNTRY SPEED AS A FUNCTION OF ASPECT RATIO, WING LOADING AND THERMAL MODEL 47
FIGURE 5.9: COMBINATION OF WING LOADING AND ASPECT RATIO YIELDING NEAR OPTIMUM AVERAGE CROSS-COUNTRY SPEED 47
FIGURE 5.10: OPTIMAL WING LOADING FOR VARIOUS SAILPLANES 48
FIGURE 5.11: VARIOUS WINGLET CONFIGURATIONS 48
FIGURE 5.12: VARIOUS LATERAL WING CONFIGURATIONS 49
FIGURE 5.13: TYPICAL TAPERED FUSELAGE 50
FIGURE 5.14: POSITION OF BOUNDARY LAYER TRANSITION AT VARIOUS SPEEDS 50
FIGURE 5.15: WING/FUSELAGE JUNCTION FOR MINIMUM INTERFERENCE DRAG 51
FIGURE 5.16: ESTIMATION OF INTERFERENCE DRAG 52
FIGURE 5.17: TYPICAL AILERON CONFIGURATIONS 53
FIGURE 5.18: EMPENNAGE ARRANGEMENTS 54
FIGURE 5.19: FORCE & MOMENT DEFINITIONS FOR LONGITUDINAL STABILITY 55
FIGURE 5.20: HORIZONTAL STABILIZER CONTRIBUTION TO STABILITY 56
FIGURE 5.21: EQUILIBRIUM CONDITIONS FOR MAXIMUM & MINIMUM WING LIFT COEFFICIENTS 57
FIGURE 5.22: INCREASE IN EFFECTIVE ASPECT RATIO DUE TO END PLATE EFFECT 58
FIGURE 5.23: COMPARISON BETWEEN WING STRUCTURAL WEIGHT FOR THICK & THIN AIRFOILS 60
FIGURE 5.24: STRESS DURING IMPACT 62
FIGURE 5.25: LOCATION OF CENTRE OF MASS FOR WING & EMPENNAGE 63
FIGURE 6.1: FLUENT PROGRAM STRUCTURE 70
FIGURE 6.2: COMPONENT ANALYSIS ORIENTATION 72
FIGURE 6.3: 3D PARAMETRIC MODEL OF RECTANGULAR WING 74
FIGURE 6.4: COMPUTATIONAL DOMAIN 75
FIGURE 6.5: MESH OF COMPUTATIONAL DOMAIN 75
FIGURE 6.6: BOUNDARY ZONES 76
FIGURE 6.7: MESH QUALITY SURROUNDING OPTIMISED SAILPLANE 76
FIGURE 6.8: OPTIMISED SAILPLANE GEOMETRY 79
FIGURE 6.9: MESH OF OPTIMISED SAILPLANE 79
FIGURE 6.10: LOAD & RESTRAINT CONDITIONS FOR STATIC ANALYSIS 80
FIGURE 6.11: IMPACT ORIENTATION 81
FIGURE 7.1: THICK & THIN AIRFOIL COMPARISON 83
FIGURE 7.2: CR 100SM, HQ 358 AND HQ 3510 COMPARISON AT 20 M/S 83
FIGURE 7.3: HQ 3510 WING ROOT - C_L vs. AOA and C_D vs. AOA 84

FIGURE 7.4: HQ 3510 WING ROOT - C_L/C_D vs. AOA and C_M vs. AOA 84
FIGURE 7.5: HQ 3510 WING TIP - C_L vs. AOA and C_D vs. AOA 85
FIGURE 7.6: HQ 3510 WING TIP - C_L/C_D vs. AOA and C_M vs. AOA 85
FIGURE 7.7: NACA 0009 STABILIZER ROOT - C_L vs. AOA and C_D vs. AOA 86
FIGURE 7.8: NACA 0009 STABILIZER ROOT - C_L/C_D vs. AOA and C_M vs. AOA 86
FIGURE 7.9: NACA 0009 STABILIZER TIP - C_L vs. AOA and C_D vs. AOA 87
FIGURE 7.10: NACA 0009 STABILIZER TIP - C_L/C_D vs. AOA and C_M vs. AOA 87
FIGURE 7.11: S9033 STABILIZER ROOT - C_L vs. AOA and C_D vs. AOA 88
FIGURE 7.12: S9033 STABILIZER ROOT - C_L/C_D vs. AOA and C_M vs. AOA 88
FIGURE 7.13: S9033 STABILIZER TIP - C_L vs. AOA and C_D vs. AOA 89
FIGURE 7.14: S9033 STABILIZER TIP - C_L/C_D vs. AOA and C_M vs. AOA 89
FIGURE 7.15: OPTIMAL WING (FIXED GEOMETRY) - Wing vs. L/D 93
FIGURE 7.16: OPTIMAL WING (FIXED GEOMETRY) - Wing vs. L/D 93
FIGURE 7.17: OPTIMAL WING (FIXED GEOMETRY) - Wing vs. L/D 93
FIGURE 7.18: OPTIMAL WING (VARIABLE GEOMETRY) - Wing vs. $\frac{L/D}{kg}$ 95
FIGURE 7.19: OPTIMAL WING (VARIABLE GEOMETRY) - Wing vs. $\frac{L/D}{kg}$ 95
FIGURE 7.20: OPTIMAL WING (VARIABLE GEOMETRY) - Wing vs. $\frac{L/D}{kg}$ 95
FIGURE 7.21: OPTIMAL WING (VARIABLE GEOMETRY) 96
FIGURE 7.22: OPTIMISED TAPERED WING WITH WINGLET - F_L vs. V 97
FIGURE 7.23: OPTIMISED TAPERED WING WITH WINGLET - F_D vs. V 97
FIGURE 7.24: OPTIMISED TAPERED WING WITH WINGLET - L/D vs. V 97
FIGURE 7.25: RECTANGULAR WING X VELOCITY CONTOURS AT 20 M/S 98
FIGURE 7.26: TAPERED WING X VELOCITY CONTOURS AT 20 M/S 98
FIGURE 7.27: TAPERED WING WITH WINGLET X VELOCITY CONTOURS AT 20 M/S 99
FIGURE 7.28: FUSELAGE - F_L vs. V 101
FIGURE 7.29: FUSELAGE - F_D vs. V 101
FIGURE 7.30: FUSELAGE - L/D vs. V 101
FIGURE 7.31: DYNAMIC PRESSURE CONTOURS ON FUSELAGE AT 20 M/S 102
FIGURE 7.32: TURBULENCE INTENSITY CONTOURS ON FUSELAGE AT 20 M/S 102
FIGURE 7.33: TAIL ASSEMBLY COMPARISON - F_L vs. AOA 104
FIGURE 7.34: TAIL ASSEMBLY COMPARISON - F_D vs. AOA 104
FIGURE 7.35: TAIL ASSEMBLY COMPARISON - L/D vs. AOA 104
FIGURE 7.36: SAILPLANE WITH DOUBLE TAPERED WING - F_L vs. V 106
FIGURE 7.37: SAILPLANE WITH DOUBLE TAPERED WING - F_D vs. V 106
FIGURE 7.38: SAILPLANE WITH DOUBLE TAPERED WING - L/D vs. V 106
FIGURE 7.39: SAILPLANE WITH TAPERED WING WITH WINGLET - F_L vs. V 107
FIGURE 7.40: SAILPLANE WITH TAPERED WING WITH WINGLET - F_D vs. V 107

FIGURE 7.41: SAILPLANE WITH TAPERED WING WITH WINGLET - L/D vs. V 107
FIGURE 7.42: SAILPLANE COMPARISON - F_L vs. V 108
FIGURE 7.43: SAILPLANE COMPARISON - F_D vs. V 108
FIGURE 7.44: SAILPLANE COMPARISON - L/D vs. V 108
FIGURE 7.45: REDUCTION IN LIFT DUE TO INTERFERENCE (SAILPLANE DOUBLE TAPERED WING) 109
FIGURE 7.46: INCREASE IN DRAG DUE TO INTERFERENCE (SAILPLANE DOUBLE TAPERED WING) 109
FIGURE 7.47: % DIFFERENCE IN AERODYNAMIC FORCES (SAILPLANE DOUBLE TAPERED WING) 109
FIGURE 7.48: REDUCTION IN LIFT DUE TO INTERFERENCE (SAILPLANE TAPERED WING) 110
FIGURE 7.49: INCREASE IN DRAG DUE TO INTERFERENCE (SAILPLANE TAPERED WING) 110
FIGURE 7.50: % DIFFERENCE IN AERODYNAMIC FORCES (SAILPLANE TAPERED WING) 110
FIGURE 7.51: DYNAMIC PRESSURE CONTOURS ON SAILPLANE AT 20 M/S 111
FIGURE 7.52: TURBULENCE INTENSITY CONTOURS ON SAILPLANE AT 20 M/S 111
FIGURE 7.53: FORCE AND MOMENT DEFINITIONS FOR LONGITUDINAL STABILITY 112
FIGURE 7.54: EQUILIBRIUM CONDITIONS FOR MAXIMUM AND MINIMUM WING LIFT COEFFICIENTS 113
FIGURE 7.55: VON MISES STRESS ON SAILPLANE AT 20 M/S 115
FIGURE 7.56: CLOSE UP OF WING STRESS AT 20 M/S 116
FIGURE 7.57: SECTIONAL VIEW THROUGH WING MID-PLANE 116
FIGURE 7.58: DESIGN CHECK 117
FIGURE 7.59: MODE 1 (1.5151 HZ) 118
FIGURE 7.60: MODE 2 (1.9698 HZ) 118
FIGURE 7.61: MODE 3 (4.6410 HZ) 119
FIGURE 7.62: MODE 4 (5.7783 HZ) 119
FIGURE 7.63: MODE 5 (7.3318 HZ) 119
FIGURE 7.64: VON MISES STRESS THROUGHOUT SAILPLANE DURING IMPACT 120
FIGURE 7.65: STRESS DISPERSAL INTO WINGS AND HORIZONTAL STABILIZER DURING IMPACT 121
FIGURE 8.1: SAILPLANE (DOUBLE TAPERED WING) 124
FIGURE 8.2: SAILPLANE (TAPERED WING WITH WINGLET) 124

List of Tables

TABLE 3.1: ICAO 1964 STANDARD ATMOSPHERE 9
TABLE 3.2: TYPICAL MODEL SAILPLANE REYNOLDS NUMBERS 11
TABLE 6.1: 1:6 PROTOTYPE SAILPLANE DETAILS 72
TABLE 6.2: REYNOLDS NUMBERS FOR WING AIRFOILS 73
TABLE 6.3: REYNOLDS NUMBERS FOR HORIZONTAL STABILIZER AIRFOILS 73
TABLE 6.4: REYNOLDS NUMBERS FOR VERTICAL STABILIZER AIRFOILS 73
TABLE 6.5: MODEL PARAMETERS 77
TABLE 6.6: MODEL BOUNDARY CONDITIONS 77
TABLE 7.1: BODY FORCES ON INDIVIDUAL WING PLANFORMS AT 10 M/S 90
TABLE 7.2: BODY FORCES ON INDIVIDUAL WING PLANFORMS AT 15 M/S 90
TABLE 7.3: BODY FORCES ON INDIVIDUAL WING PLANFORMS AT 20 M/S 91
TABLE 7.4: EFFECTIVE LIFT OF INDIVIDUAL WING PLANFORMS 92
TABLE 7.5: L/D RATIO OF INDIVIDUAL WING PLANFORMS 92
TABLE 7.6: L/D RATIO AND INDIVIDUAL NORMALISED BODY FORCES AT 10 M/S 94
TABLE 7.7: L/D RATIO AND INDIVIDUAL NORMALISED BODY FORCES AT 15 M/S 94
TABLE 7.8: L/D RATIO AND INDIVIDUAL NORMALISED BODY FORCES AT 20 M/S 94
TABLE 7.9: BODY FORCES ON TAPERED WING WITH WINGLET (VARIED GEOMETRY) . 96
TABLE 7.10: BODY FORCES ON FUSELAGE AT 10 M/S 100
TABLE 7.11: BODY FORCES ON FUSELAGE AT 15 M/S 100
TABLE 7.12: BODY FORCES ON FUSELAGE AT 20 M/S 100
TABLE 7.13: BODY FORCES ON TAIL ASSEMBLY AT 10 M/S 103
TABLE 7.14: BODY FORCES ON TAIL ASSEMBLY AT 15 M/S 103
TABLE 7.15: BODY FORCES ON TAIL ASSEMBLY AT 20 M/S 103
TABLE 7.16: BODY FORCES ON SAILPLANE WITH DOUBLE TAPERED WING 105
TABLE 7.17: BODY FORCES ON SAILPLANE WITH TAPERED WING WITH WINGLET 105
TABLE 7.18: FIRST 5 RESONANT FREQUENCIES 118
TABLE 8.1: SAILPLANE (DOUBLE TAPERED WING) 124
TABLE 8.2: SAILPLANE (TAPERED WING WITH WINGLET) 124

Nomenclature

AR	Aspect Ratio	
C_D	Drag Coefficient	
C_{D_i}	Induced Drag Coefficient	
C_{D_0}	Drag Coefficient at Zero Lift	
C_L	Lift Coefficient	
$C_{L_{MAX}}$	Maximum Lift Coefficient	
C_M	Moment Coefficient	
C_{M_0}	Moment Coefficient at Zero Lift	
C_p	Pressure Coefficient	
$\frac{dC_{L_w}}{d\alpha_w}$	Lift Curve Slope Wing	
$\frac{dC_{L_H}}{d\alpha_H}$	Lift Curve Slope H. Stabilizer	
$\frac{dC_{L_V}}{d\beta_V}$	Lift Curve Slope V. Stabilizer	
F_D	Lift Force	N
F_L	Drag Force	N
$\frac{L}{D}$	Lift to Drag Ratio	
M	Mach Number	
Re	Reynolds Number	
S	Reference Area	m^2
T	Thrust	N
V_∞	Freestream Velocity	m/s
V_H	Horizontal Stabilizer Volume Coefficient	
V_w	Wing Volume Coefficient	
V_V	Vertical Stabilizer Volume Coefficient	
V_s	Sink Velocity	m/s
$\frac{W}{S}$	Wing Loading	daN/m^2
W	Weight	N
b	Wing Span	m
c	Chord	m

c_k	Chord at Taper Change Point	m
c_{root}	Chord (Root)	m
c_{tip}	Chord (Tip)	m
c_μ	Mean Chord	m
e	Oswald Efficiency Factor	
f	Camber	%
g	Gravitational Acceleration	9.81 m/s^2
h	Height above Sea Level	m
l	Characteristic Length	m
ℓ_H	Horizontal Stabilizer Moment Arm	m
ℓ_V	Vertical Stabilizer Moment Arm	m
p_∞	Freestream Static Pressure	Pa
q_∞	Freestream Dynamic Pressure	Pa
s	Semi-Span	m
t	Chord Thickness	m
$\frac{t}{c}$	Sectional Thickness to Chord Ratio	
x_{AC}	Longitudinal Location of Wing Aerodynamic Centre	m
x_{CG}	Longitudinal Location of Aircraft Centre of Gravity	m
x_N	Longitudinal Location of Aircraft Neutral Point	m
x_f	Location of Maximum Camber	m
x_t	Location of Maximum Sectional Thickness	m

Greek

α_e	Effective Angle of Attack	deg.
α_g	Geometric Angle of Attack	deg.
α_i	Induced Angle of Attack	deg.
ρ	Fluid Density	kg/m^3
λ	Taper Ratio	
γ	Glide Angle	deg.
υ	Kinematic Viscosity	m^2/s

Glossary

Aerodynamic

Drag

Drag is a mechanical force generated though the interaction and contact of a fluid with a solid body tending to oppose its forward movement. Drag is composed of two main types; induced drag and parasitic drag.

Induced Drag

Induced drag results from the turbulence and vortices imparted to the air by a moving body. On an aircraft wing this drag occurs because the flow near the wing tips is distorted spanwise as a result of the pressure difference from the top to the bottom of the wing. Swirling vortices are formed at the wing tips, which produce a downwash of air behind the wing which is very strong near the wing tips and decreases toward the wing root. This additional force is called the *induced drag* because it has been "induced" by the action of the tip vortices. It is also called "drag due to lift" because it only occurs on finite, lifting wings. The magnitude of induced drag depends on the amount of lift being generated by the wing and on the wing geometry. Long, thin wings have low induced drag; short, thick wings have high induced drag.

Parasitic Drag

Parasitic drag results from the shape and size of the body, and from the mere fact that it is being pushed through the air. It will occur whenever a body is moved through a fluid. Parasitic drag itself is composed of several sub-types; including skin friction (the friction that results from the moving air molecules over the solid surface) and pressure drag (the energy transferred to the air in the action of displacing it to move a body through it).

The magnitude of the drag force (measured in *Newton's*) that will be developed by a body is characterized by the non-dimensional parameter, the *Coefficient of Drag,* C_D. If C_D is known, the drag force may be calculated using the relationship,

$$F_D = C_D \frac{1}{2} \rho V^2 A$$

where A is the projected area of the body (For a wing it is the planform area), V is the relative velocity of the fluid and ρ is the fluid density .

Additionally, with respect to aircraft wings, if the coefficient of drag is unknown it can be calculated by,

$$C_D = C_{D_0} + \frac{C_L^2}{\pi \cdot AR \cdot e}$$

where C_{D_0} is the drag coefficient at zero lift, C_L is the coefficient of lift, AR is the aspect ratio of the wing and e is the efficiency factor. A typical efficiency factor for a rectangular wing is 0.70 .

Lift

Lift is a mechanical force generated though the interaction and contact of a fluid with a solid body that acts perpendicular to the flow direction and directly opposes the body's weight. Lift occurs whenever a moving flow of fluid is deflected by a solid object. The flow is turned in one direction, and the lift is generated in the opposite direction, according to *Newton's Third Law* of action and reaction. For an aircraft wing, both the upper and lower surfaces contribute to the flow turning and this is known as the *Coanda Effect*. Lift is characterized by the non-dimensional parameter, the *Coefficient of Lift*, C_L. Like drag, if C_L is known, lift force can be calculated through:

$$F_L = C_L \frac{1}{2} \rho V^2 A$$

L/D Ratio

Because lift and drag are both aerodynamic forces, the ratio of lift to drag is an indication of the aerodynamic efficiency of a vehicle. Aerodynamicists call this the *L/D ratio*, pronounced "L over D ratio." An aircraft has a high L/D ratio if it produces a large amount of lift or a small amount of drag.

Pressure

Pressure is the force per unit area exerted by a fluid on a body or surface. It is mathematically defined as $Pressure = \frac{Force}{Area}$, and is measured in Pascals (Pa), where one Pascal is equal to one Newton per square meter. Pressure is usually measured from one of two reference points:

Absolute zero pressure: This gives the total force over the affected area. When pressure is measured from this point the value is called *Absolute Pressure*, P_{abs}. And,

Atmospheric pressure (P_{atm}): This gives the nett useable force over the affected area. This is called *Gauge Pressure*, P_{gauge}.

These referenced points are mathematically related through: $P_{abs} = P_{atm} + P_{gauge}$

Additionally, pressure can be classified under two main categories, Static and Dynamic.

Static Pressure

Static Pressure is a measure of the potential ("pressure") energy of the air particles. It is the pressure that is measured by an instrument moving with the flow.

Dynamic Pressure

Dynamic Pressure is a measure of the kinetic energy of the air particles in the flow field. It is the pressure that is measured by an instrument moving with the body and not with the flow. A classic example of this is the *Pitot tube* (pronounce pea-toe) that can be used to determine the airspeed of an aircraft.

These pressures are mathematically related through: $P_{Total} = P_{Static} + P_{Dynamic}$

Streamlines

Streamlines are lines drawn in a flow field so that at a given instant they are tangential to the direction of flow at every point in the flow field. By this definition, since the streamlines are tangential to the velocity vector at every point in the flow field, there can be no flow across a streamline. Put simply, a streamline is the path in which an individual fluid particle travels. Streamlines can be effectively illustrated in computer simulations (Figure 1.1) and in wind tunnel tests (Figure 1.5).

Laminar Flow

Laminar flow is one in which the fluid particles move in a smooth motion, and is diagrammatically represented by smoothly-curved or straight, near-parallel streamlines. Neighboring layers of laminar flow do not mix but can flow at different velocities.

Turbulent Flow

Turbulent flow is one in which the neighboring fluid particles move with irregular local velocities causing macroscopic mixture. Turbulent flow can be diagrammatically represented by a single streamline that breaks up into many tangled pieces.

Reynolds Number

Reynolds Number is the non-dimensional parameter that can be used to determine whether a flow field is laminar or turbulent. It is mathematically defined by:

$$\mathrm{Re} = \frac{\rho V D}{\mu}$$

where ρ and μ is the density and absolute viscosity of the fluid, V is the relative velocity, and D is the characteristic dimension of the body. If the Reynolds Number for a particular fluid is above a certain critical value $\left(\mathrm{Re}_{critical}\right)$, the flow is deemed turbulent, while if it is below, the flow is considered laminar. It must be mentioned that $\mathrm{Re}_{critical}$ is dependent on the geometry of both the flow field and the body.

Separation

Under certain conditions, the flow over a body may become *separated* from the bodies' surface. Separated flow is often characterized by large scale, un-steady turbulence that, in the case of an aircraft wing, reduces lift drastically.

Reattachment

After a flow has separated from a body, a large, drag-inducing turbulent wake is produced in the space previously occupied by un-separated air. However, through the clever design of surface and/or body geometry, the separated flow may be *reattached*. This allows the resumption of smooth, low-drag, laminar flow, shown in Figure 1.7.

Turbulence

Turbulence is an instability within the atmosphere that disrupts the flow of air, causing gusty, unpredictable air currents.

Boundary Layer

The *boundary layer* associated with viscous fluid flow is that layer adjacent to a stationary surface, in which there exists a shear stress between adjacent particles, and therefore, a velocity gradient extending away from the surface.

Stagnation Point

The *stagnation point* is a point in a fluid flow where the velocity is zero. On any solid body fully immersed in potential flow there will always be two stagnation points. The shape of the body (in this case an aerofoil) will dictate the position of the stagnation points.

Angle of Attack

The *angle of attack* is the acute angle between the direction of airflow and the line linking the leading and trailing edges of an aircrafts' wing.

Vortex

A *vortex* is a swirling mass of turbulent fluid that generally has negative side effects including drag and instability.

Inviscid Flow

Inviscid Flow assumes that that the flow field extends to the surface of the body, with no decrease in velocity as the surface is approached.

Viscous Flow

In reality, a boundary layer exists adjacent to the body in which the velocity diminishes from the local flow velocity down to zero at the surface. This is known as *Viscous Flow*.

Compressible Fluid

A *Compressible Fluid* is a fluid that can be compressed and therefore its density, ρ, is dependent on the local pressure.

Incompressible Fluid

An *Incompressible Fluid* is a fluid with the inability to be compressed and therefore its density, ρ, remains constant.

Aircraft

As well as the aerodynamic terms, there are also a number of terms used with respect to the sailplane.

Aerofoil

The aerofoil or airfoil is the cross-sectional shape of an aircrafts wing that that acts on the air to provide lift.

Ailerons

Ailerons are the hinged flaps on the trailing edge of an aircrafts wing which are used to control turning movements.

Angle of Incident

The *angle of incident* is the apparent angle between the wing profile and the aircrafts fuselage.

Aspect Ratio

The *aspect ratio* is the ratio of the length of an aircraft's wing to the mean distance between the front and back edge of the wing. High performance sailplanes generally have aspect ratios of 30-40.

Chord

The *chord* is the shortest distance between the leading and trailing edges of an aerofoil.

1.7.5 Cockpit

The *cockpit* is the foremost passenger space of an aircraft and the area in which the pilot controls the aircraft.

Dihedral Angle

The *dihedral angle* is the angle between an upwardly inclined aircraft wing and the horizontal axis. This angle greatly effects the stability of an aircraft.

Fuselage

The *fuselage* is the main cabin, or body of the aircraft. Generally the fuselage has a cockpit section at the front end, where the pilot controls the aircraft, and a cabin section. In sailplanes the fuselage is usually nothing more than a minimal hollow structure connecting the wings, tail, and cockpit.

Wings

The *wings* are the large flat surfaces fixed to the sides of an aircraft's body that provide the main source of lift. All aircraft, by definition, have wings.

Tail Assembly

The *tail assembly* is attached to the rear of the fuselage and consisting of the vertical and horizontal stabilizers, a rudder; and elevators. The components of the tail assembly are collectively referred to as the *empennage.*

Stabilizers

The *stabilizers* serve to help keep the aircraft stable while in flight and are located in the tail assembly. They consist of aerofoil structure, much the same as a wing, which aid in keeping an aircraft aligned with the direction of flight.

Rudder

The *rudder* is at the trailing edge of the vertical stabilizer and is used by the aircraft to help control turns. An aircraft actually turns by banking, or moving its wings laterally, but the rudder helps to keep the turn coordinated by serving much like a boat's rudder to move the nose of the aircraft left or right. Moving an aircrafts' nose left or right is known as a yaw motion.

Elevators

Elevators are control surfaces at the trailing edge of the horizontal stabilizers. The elevators control the up-and-down motion, or pitch, of the aircrafts' nose. Moving the elevators up into the air stream will cause the tail to go down and the nose to pitch up and vice versa.

Wing Planform

The *wing planform* is the basic shape of wing viewed from above. Common planforms include rectangular and elliptical.

Winglets

Winglets are small aerodynamic surfaces extending upwards from the wingtips. According to the simplest theory, this allows some of the wing vortices to continue into the winglet where it is then trailed away from the plane of the wing. Winglets are used to reduce induced drag by preventing the trailing vortices coming into contact with the wings' surfaces.

Chapter 1

Introduction

This chapter outlines the background, purpose and objectives of this thesis as well as provides an introduction into the necessity of this study.

1.1 Introduction

With air travel becoming more and more important in our every day lives, steps must be continually taken in order to optimise flight performance. With these efforts frequently centered on the aerodynamic properties of the aircraft, it seems obvious that by taking a step back and placing more emphasis on optimising the aerodynamic properties of un-powered aircraft, limitless possibilities may be realised in the powered sector. While the aerodynamic theory behind flight efficiency has existed for many years, little information exists or is released on the design methods of the high performance aircraft that best utilise this theory. One such example is that of the sailplane.

This thesis seeks to investigate the theoretical foundation of un-powered aircraft design as well as implement computational methods to design and optimise a prototype sailplane.

1.2 Background

A sailplane is essentially a heavier-than-air aircraft that remains aloft as a result of the aerodynamic forces acting upon it. In form, sailplanes resemble ordinary aircraft incorporating all the fundamental components such as the wings, fuselage and tail assembly. However, comparatively sailplanes and ordinary aircraft are much different. While sailplanes appear relatively simple, the design of such an un-powered aircraft to fly efficiently in any given weather condition is quite challenging. This is largely due to the fact that in flying cross country, sailplane's must be able to climb effectively in thermals at low speeds, as well as being able to glide efficiently between thermals at high speeds. Thus, a successful design must balance the conflicting requirements of climbing and cruising over a broad range of possible soaring conditions.

In order to help satisfy these requirements, sailplane's exhibit several key characteristics. Typically, a modern sailplane is extremely light in weight, has very slender wings and a streamlined body capable of slicing through air. These characteristics enable the aircraft to exploit a number of atmospheric conditions in order to stay aloft.

Fig. 1.1: High performance sailplane

To clarify, the term sailplane is actually reserved for a particular type of glider. In general, there are three main types:

- *Primary gliders* which are used entirely for instruction purposes, consisting of little more than girder framework to which the wings and the stabilizing surfaces are attached.
- *Secondary gliders*, or *Sailplanes*, which are built like ordinary airplanes and are designed for maximum aerodynamic efficiency, and
- *Cargo gliders*, which are used for military or peacetime purposes; these large aircraft are designed to carry heavy loads.

Since by definition sailplanes have no means of propulsion they must be launched through other methods. Sailplanes can be launched by an elastic shock cord or more commonly towed into the sky by a tow plane. Once into the sky, sailplanes use gravity and updrafts to keep aloft; slope soaring relies on wind rising off dunes or hillsides, while thermal soaring exploits convection currents in the air. In soaring, the sailplane is repeatedly manoeuvred through updrafts to reach altitudes as high as 14,000 m. Using this ability to stay aloft, sailplanes can travel as much as 800 km.

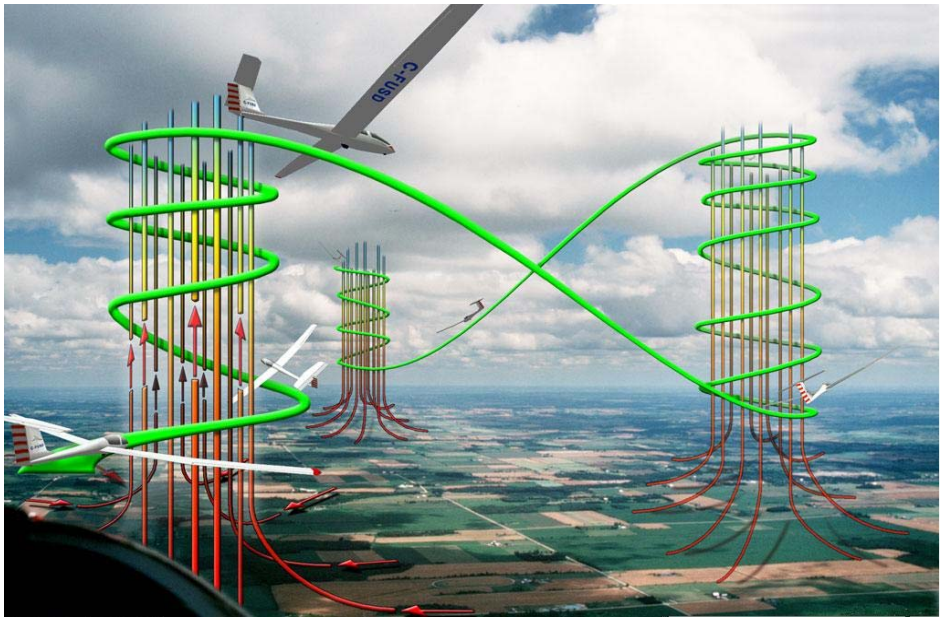

Fig. 1.2: Thermal Gliding

Although sailplanes are primarily used for competition, they are also used for recreational purposes. In either instance the sailplane design needs to be highly optimised in order to successfully complete the intended purpose. While modern sailplanes have already reached a high level of perfection, significant improvements are still possible with continued research. Unfortunately however, in recent years this research and its documentation have been extremely limited. Despite this, progression towards the optimal design must be continued in order to develop breakthroughs in not only sailplane design, but also in other aerodynamic fields.

1.3 Research Purpose

Due to the lack of sailplane design methods available and the limitations of current technology, sailplane progression has somewhat plateaued. At this stage, significant improvements are only possible with considerable research and development of the techniques necessary to optimise sailplane designs. In doing so, not only will the un-powered sector benefit, but additionally the powered sector also has the potential to gain from the discoveries. Therefore, the overall purpose of this study is to aid to the improvement of sailplane design and ultimately to the betterment of the aerodynamic field.

1.4 Research Objectives

The primary objective of this project is to design and optimise a prototype sailplane based on its aerodynamic efficiency. In order to achieve this, background information regarding the basics of aerodynamics and sailplane design must first be researched. Once completed and documented, this information will be combined to develop a number of potentially optimal aircraft components. These components include the airfoil, wing planform, fuselage and tail assembly geometries. To accomplish this, two forms of computational software will be utilised; computational fluid dynamics and stress analysis. Since this project is primarily based on the aerodynamic characteristics of the prototype, the majority of the study, including the optimisation process, will be based on the CFD analysis. The stress analysis will be used to ensure the aerodynamically optimised design can withstand the aerodynamic loads and subsequent stresses associated with normal operation. Using the CFD software, the components will be analysed and evaluated on various aspects in order to determine the appropriate combination to make up the prototype. In this way, the study will identify the effectiveness of each of the different components and eventually lead to an optimal design.

1.7 Conclusion

This thesis aims to develop and utilise a design method to optimise a prototype sailplane with respect to aerodynamic efficiency. The study is expected to determine the specific configuration of sailplane components to provide optimal performance. A review of the relevant literature is provided in the following chapters in order to identify the research has been carried out thus far as well as the necessary research that is still required in order to complete the previously mentioned objectives. The outcome of this study is hoped to provide further improvement in the aerodynamic field specific to this study hopefully resulting in more optimal sailplane designs for the future.

Chapter 2

Literature Review

This chapter contains a summarized version of the information previously researched and documented by others in the aerodynamic field. This information is provided to further illustrate the necessity and relevance of this study.

2.1 Introduction

In order to fulfil the requirements of the objectives previously stated, a detailed literature review was conducted in order to investigate the background information, design methods and previous research methods employed in both sailplane design and numerical aircraft analysis. To accomplish this, a variety of information resources were accessed including databases, websites, on-line texts, books and journals. After reviewing this information, the salient aspects were recorded and detailed.

2.2 Background

The information contained within this section provides the relevant background information necessary to understand and fully appreciate this thesis.

2.2.1 Basics of Aerodynamics

Because of the complexity associated with the flow about an aircraft, it was necessary to research and document the relevant information pertaining to fluid-solid interaction. This information was contained within numerous texts and allowed the easy attainability of the basic, yet relevant information necessary to complete this study.

Anderson (1991), Kuethe and Chow (1986), Fox, McDonald and Pritchard (2004) each provided comprehensive information with regard to basic aerodynamics. This information detailed the fundamental equations of fluid flow and provided significant information on Reynolds number and boundary layer phenomenon.

Thomas (1984) provided a broad range of information concerning two-dimensional and three-dimensional wing theory. This information was pertinent to the understanding of the fundamental differences between two-dimensional and three-dimensional wings. In addition, this text was one of the very few that provide information regarding the surface quality of aircraft structures and its affects.

Only the most relevant texts have been highlighted here; for further sources of information regarding the basics of aerodynamics refer to the reference page at the conclusion of this thesis.

Because of the fundamental importance of this information, further details highlighting the specific information relevant to this study has been provided in the chapter three.

2.2.2 Flight Mechanics

In addition to the basics of aerodynamics, flight mechanics was also thoroughly researched. Flight mechanics is the information specific to the aircraft geometry and the influences of the fluid flow on it.

Drela (1989) and Eppler (1990) significantly researched the influences of airfoil and wing geometry on lift and drag properties of sailplanes. This information was vital in understanding the results obtained from the numerical analysis. Both researchers' are considered as leading visionaries by the wider aerodynamic community for their respective contributions in the aerodynamic field.

Holighaus (1971) extensively researched the influence of wing planform and airfoil geometry. This research provided the basis for the wing planform designs later discussed in chapter six.

Pamadi and Bandu (1998) investigated the stability and control methods of aircraft. This information was used to determine both the static and dynamic stability of the final sailplane design.

Potkanski (1986) provided comprehensive details regarding the wing flutter of light aircraft. This research was pertinent to the determination of the aeroelastic behaviour of the final sailplane design.

Again, this information has been further detailed in chapter four to aid in the understanding of this thesis.

2.3 Design Methods

The literature relevant to prototype sailplanes is minimal at best. Fortunately, the same principles which apply to full size aircraft can also be applied to smaller models without significant lost in generality. This section details the significant contributors to sailplane design methods.

2.3.1 Design Requirements and Optimisation

Drela (1989), Eppler (1990) and Selig (1995) all extensively researched and provided significant information on subsonic airfoil and wing design. These researchers were some of the very few that actually documented the design methods through which to obtain optimal performance. These design methods were used to determine the optimal airfoil geometry.

Drela, M., Mortara, K. & Maughmer (1993) researched and provided information on the design methods of winglet design. This information was used to create the simplest and most appropriate winglet design in order minimise induced drag.

Thomas (1984) documented the information relevant to optimal wing loading. Unfortunately however, the design methods through which to obtain this were severely lacking. In contrast, information regarding the design methods of the fuselage and wing/fuselage junctions was extensively detailed. This information was employed to determine the appropriate fuselage and wing/fuselage geometry.

Because of the sever lack of design method information available chapter five contains comprehensive details of the research mentioned here.

2.3.2 Numerical Analysis

Drela (1989, 1990, 2001), Eppler (1990) and Ferziger and Peric (1998) all investigated and performed detailed numerical analyses on subsonic isolated airfoils and wings. This information extensively detailed the computational design methods necessary to obtain the optimal design. Of particular relevance to this study was Eppler and Drela's computational fluid flow programs. These programs calculate the aerodynamic properties of isolated subsonic airfoils and display the results in an interactive window. Due to the relative easy and accuracy of Drela's program, XFOIL, it was employed for this investigation.

2.4 Conclusion

It was found that although there was numerous amounts of literature detailing the specifically what is necessary for optimal performance, little information existed on the actual design methods themselves. Of the literature reviewed, Drela (1989,1990), Eppler (1990) and Thomas (1984) provided the most comprehensive details on design optimisation and the methods through which to obtain this. The information presented this chapter is designed to provide a brief overview of the previous research and aid in the understanding of the study topic.

Chapter 3

Basics of Aerodynamics

This chapter provides a brief introduction to the fundamentals of aerodynamics. Only the most relevant details associated to this thesis are outlined. This information is provided to aid in the understanding of the following chapters.

3.1 Inviscid Incompressible Flow

3.1.1 Physical Properties of the Atmosphere

The flow of air around a sailplane in flight is determined by the laws of fluid mechanics. The state of the air is defined by a number of physical properties such as pressure, density, temperature, compressibility, kinematic viscosity, and relative humidity. As a result of gravity, the properties of the atmosphere vary with altitude. Properties such as pressure, density, and temperature all decrease with rising altitude. Solar radiation and topography also cause considerable variation in the atmospheric properties. This effect is especially pronounced at low altitudes.

To account for these variations, several standard atmospheric models are used to evaluate aircraft data at different altitudes. The values presented in Table 3.1 summarise some data of interest from the 1964 ICAO (International Civil Aviation Organisation) Standard Atmosphere, a commonly used standard that represents an atmosphere free from meteorological influences. Other idealised models also exist, however the results presented throughout this thesis are based on the 1964 ICAO model.

It should be emphasised that this standard atmospheric model and others like it, are idealisations based on empirical data and/or simplified mathematical models. The pressure, p, density, ρ, and absolute temperature, T, of an ideal gas are related to one another through the *ideal gas law:*

$$p = \rho RT \qquad (1)$$

where R is the specific gas constant for the gas or mixture of gases.

Therefore, it can be deduced that an increase in pressure results in an increase in density and/or air temperature. The process of thermal formation, familiar to all sailplane pilots, is governed by this physical law. Thermal formation occurs when solar radiation increases the temperature near the earth, leading to a local reduction in air density. The affected parcel of air becomes more buoyant than the surrounding air and climbs skyward as a thermal. This will be discussed further in later chapters.

Table 3.1: ICAO 1964 Standard Atmosphere

Altitude h m	Pressure p [hPa]	Density ρ $[kg/m^3]$	Temp. T ^oK	Kinematic Viscosity v $10^{-5}[m^2/s]$	Speed of Sound c $[m/s]$
0	1013.3	1.225	288.2	1.46	340.3
500	954.6	1.167	284.9	1.52	338.4
1000	898.7	1.112	281.7	1.58	336.4
1500	845.6	1.058	278.4	1.65	334.5
2000	795.0	1.007	275.2	1.71	332.5
2500	746.8	0.957	271.9	1.79	330.6
3000	701.1	0.909	268.7	1.86	328.6
4000	616.4	0.819	262.2	2.03	324.6
5000	540.2	0.736	255.7	2.21	320.5
8000	356.0	0.525	236.2	2.91	308.1
11000	226.3	0.364	216.7	3.91	295.1
15000	120.4	0.194	216.7	7.34	295.1
20000	54.7	0.088	216.7	16.15	295.1
30000	11.7	0.018	226.7	81.95	301.8

3.1.2 Basics of Fluid Mechanics

The equations governing the flow about an aircraft are extremely complicated. Air particles flowing past an aircraft are accelerated, compressed, and sheared against one another leading to inertial, elastic and viscous forces respectively. The relationship between these forces and the geometric form of the aircraft is defined by the *Navier-Stokes equations*, the fundamental equations of fluid mechanics. Given the geometric shape of a body, for example an airfoil, the Navier-Stokes equations may be used to calculate the velocity and pressure distributions in the resulting flow.

The flow field is defined by the local velocity (speed and direction) and pressure at each point in the field. As will be discussed later, the pressure and velocity at a given point are directly related to one another. The local velocity is the sum of the freestream velocity

V_∞ (the velocity of the undisturbed flow far upstream of the object) and local perturbations due to the presence of the body. The latter decrease in magnitude as the distance from the object increases (Fig. 3.1).

Incidentally, it does not matter whether a body is placed in a stream of flowing air, for example in a wind tunnel, or moves with constant velocity through a mass of still air. In both cases the flow field is identical [11].

Note: The Navier-Stokes equations can be reviewed in more detail in Chapter 6.

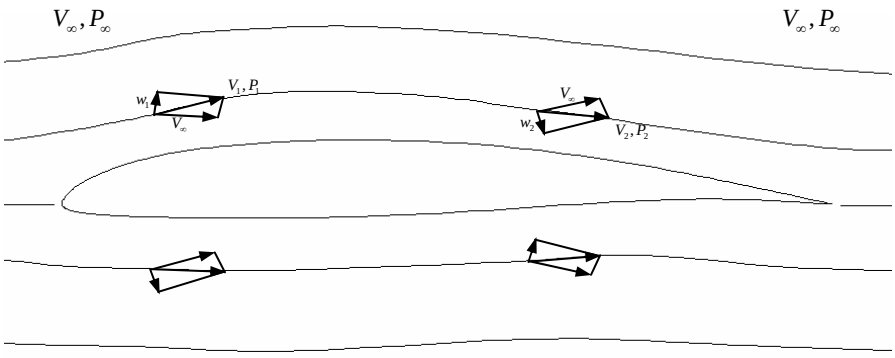

Fig. 3.1: Flow field near airfoil in steady flow

V_∞	**freestream velocity**
$V_{1,2}$	**local velocities**
$w_{1,2}$	**local perbutation velocities**
$P_{1,2}$	**local pressures**
P_∞	**freestream pressure**

3.1.3 Reynolds Number and Boundary Layer

Due to their complexity, the Navier-Stokes equations do not easily lend themselves for use in calculating the aerodynamic characteristics of model sailplanes. Fortunately, the nature of model sailplane aerodynamics allows these equations to be simplified considerably. The primary simplification results from the fact that, throughout most of the flow field, the inertial forces are considerably more significant than the viscous forces. For a given flow field, the relationship between these forces is characterised by the *Reynolds number*, defined as follows:

$$\mathrm{Re} = \frac{V_\infty l}{\upsilon} = \frac{Inertial\ Forces}{Viscous\ Forces} \qquad (2)$$

Where V_∞ is the freestream velocity [m/s], l is the characteristic length [m] of the body (for example the airfoil chord or the fuselage length), and υ the kinematic viscosity of the fluid [m^2/s]. The Reynolds number itself is dimensionless.

Table 3.2: Typical model sailplane Reynolds numbers. Based on kinematic viscosity $v = 1.5\times10^{-5}\ m^2/s$ and a range of wing chords.

Freestream Velocity V_∞	Chord c [m]	Reynolds Number Re [-]
$10\ m/s$ $(36\ km/h)$	0.30	0.20×10^6
	0.25	0.17×10^6
	0.20	0.13×10^6
	0.15	0.10×10^6
$20\ m/s$ $(72\ km/h)$	0.30	0.40×10^6
	0.25	0.33×10^6
	0.20	0.27×10^6
	0.15	0.20×10^6

Typical Reynolds numbers for model sailplane airfoils are shown in Table 3.2. The data indicates that the inertial forces in the flow field about a model sailplane are around one quarter of a million times larger than the viscous forces. For this reason, the viscous forces can be neglected throughout most of the field, allowing for the use of the simpler inviscid flow equations. It should be noted that viscous forces only become significant in a relatively thin layer near the surface of the aircraft, known as the *boundary layer*. The higher the Reynolds number, the thinner the boundary layer becomes relative to the characteristic length of the body.

An important phenomenon to note is that airfoil drag and maximum lift coefficients are strongly affected by boundary-layer. On the other hand, the effect on pressure distribution and lift is relatively insignificant. So, when determining the pressure distribution and lift (with the exception of the maximum lift) one may assume inviscid flow without introducing significant errors [11].

3.1.4 Bernoulli's Equation

A more intimate understanding of the interactions between solid and fluid in the flow field is gained though Bernoulli's equation. This states that in steady, incompressible, inviscid flow, the total pressure, p_{Total} (*i.e.* the sum of the static pressure *p* and the dynamic pressure *q*), remains constant along a streamline. This means, for example, that the sum of the static and dynamic pressures far upstream of an aircraft (p_∞ and q_∞, respectively) is equal to the sum of the local static and dynamic pressure p_1 and q_1 at any arbitrary point on the aircraft (Fig. 3.2).

From this interpretation, it can be seen that Bernoulli's equation is an expression of the law of conservation of energy. An increase in the local kinetic energy (*i.e.* local velocity) is accompanied by a corresponding reduction in potential energy (static pressure). As will be discussed, this exchange between pressure and velocity is of particular significance to the production of lift [11].

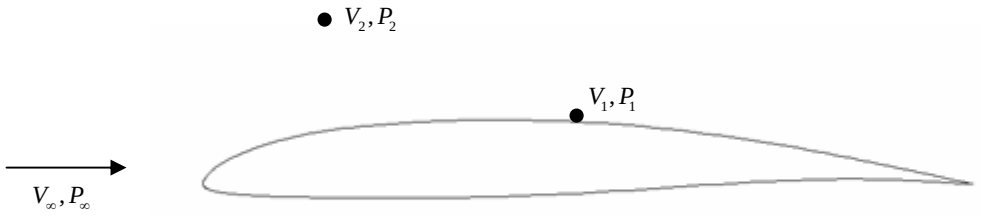

$$p_{Total} = \frac{\rho}{2}V_\infty^2 + p_\infty = \frac{\rho}{2}V_1^2 + p_1 = \frac{\rho}{2}V_2^2 + p_2$$

Fig. 3.2: Relationship between velocity and static pressure (Bernoulli's Equation)

3.1.5 Mach Number and Incompressible Flow

A further simplification results from the fact that model sailplane airspeeds are relatively small compared to the speed of sound (c = 340m/s at sea level). The ratio of the airspeed to the speed of sound is known as the *Mach number*.

$$M = \frac{V_\infty}{a} = Mach\ Number \qquad (3)$$

At low Mach numbers (M less than around 0.3), the elastic forces in the air flow can be neglected, *i.e.* the air can be considered incompressible without significant error. In this case the density, ρ, becomes a constant, no longer dependent on the pressure. Given that model sailplanes fly with Mach number well below 0.3, this thesis will use incompressible flow throughout.

3.2 Lift

3.2.1 Circulation

The primary purpose of the wing is to provide lift. Central to the production of lift is the relationship between the wing geometry (airfoil and planform) and the distribution of lift over its surface. This relationship can be expressed in several different ways. One method involves using point vortices and a derived quantity known as *circulation* [11].

To provide an in-depth explanation of the circulation theory a basic knowledge of vortices must first be established. An individual vortex is associated with a radially symmetric velocity field having circular streamlines centered around the vortex location (Fig. 3.3).

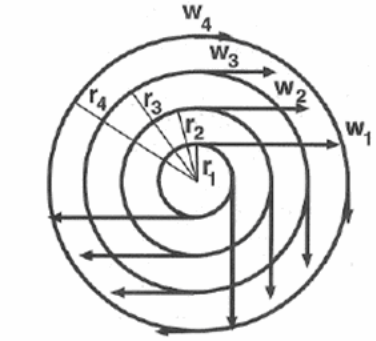

Fig. 3.3: Velocity field induced by two-dimensional vortex of strength Γ [26].

$$\Gamma = 2\pi r_1 w_1 = 2\pi r_2 w_2 = 2\pi r_3 w_3 = 2\pi r_4 w_4$$

The velocity *v* is constant along any given streamline, but decreases with the distance from the vortex center. Multiplying the velocity *v* by the circumference of the vortex yields the derived quantity, circulation given as:

$$\Gamma = 2\pi r v(r) \tag{4}$$

When considering the circulation about any closed path system of vortices the total circulation of the system is equal to the sum of the circulations due to each individual vortex (Fig. 3.4):

$$\Gamma = \oint v \cos\theta ds \tag{5}$$

$$\Gamma = \Gamma_1 + \Gamma_2 + \Gamma_3 + \Gamma_4 + \Gamma_5 \tag{6}$$

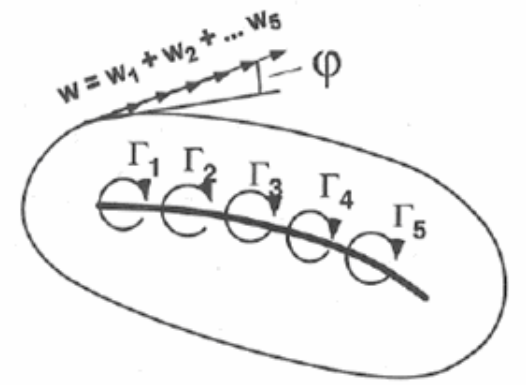

Fig. 3.4: Circulation around a system of two-dimensional vortices [26].

By superimposing a system of vortices on a uniform flow field the affects of the resulting velocity field can be illustrated. Above the vortex system, the velocity due the vortices is added to the freestream velocity V_∞, resulting in an increased total velocity equal to $V_\infty + v$. On the other hand, below the vortex system the velocity contribution from the vortices opposes the freestream velocity, resulting in a reduced total velocity of $V_\infty - v$. Therefore, according to Bernoulli's equation, the static pressure above the vortex system, p_{upper}, is lower than the freestream pressure, p_∞, and below the vortex system the static pressure, p_{lower}, is higher than the freestream pressure (Fig. 3.5).

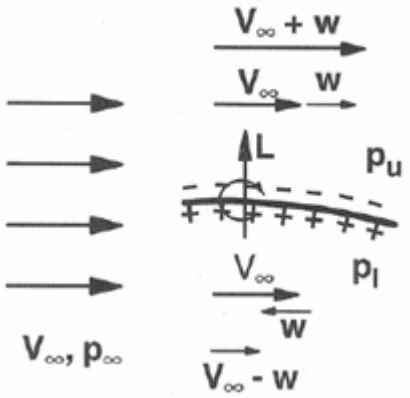

Fig. 3.5: Lift produced by superposition of vortex system [26].

Therefore, applying this to an airfoil, this pressure differential results in an upwards force, *L*, perpendicular to the freestream velocity, V_∞. By convention, the force acting perpendicular to the direction of flow is defined as lift, and the force along the direction of flow is defined as drag.

The lift, *L*, is proportional to the total circulation Γ of the vortex system, the freestream velocity V_∞, the density ρ, and the span *b* (Fig. 3.6):

$$L = b\rho V_\infty \Gamma \qquad (7)$$

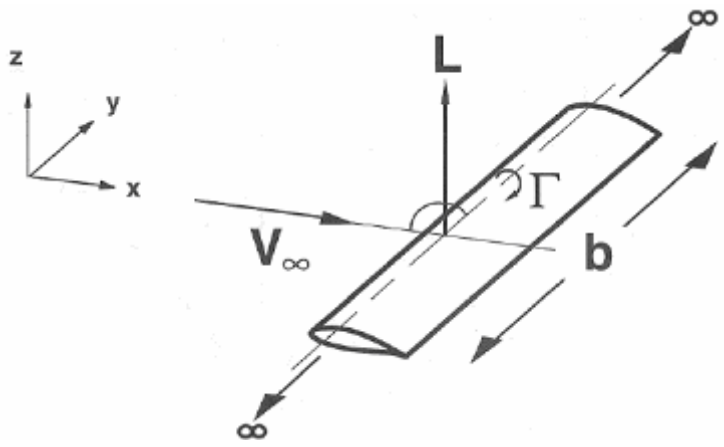

Fig. 3.6: Lift on finite wing due to circulation [26].

3.2.2 Two-Dimensional and Three-Dimensional Theory

For a two-dimensional wing, the vortex model consists of a system of infinitely long vortex filaments distributed along the chord of the wing (Fig. 3.7). The two dimensional wing extends to infinity in the y-direction; that is, perpendicular to the freestream velocity and direction of lift. The flow field is thus identical in any plane defined by y = constant. Airfoil geometry and pressure distribution are functions of x and z only, hence the term “two-dimensional” wing or “airfoil theory”.

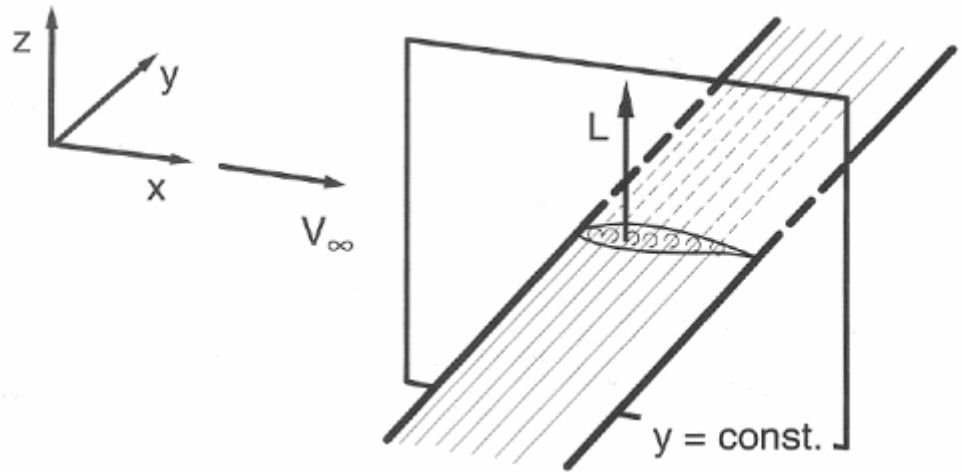

Fig. 3.7: Vortex model of idealised two-dimensional wing [26].

The vortex model for a finite span wing is considerably more complicated. According to the *Helmholtz vortex theorem*, individual vortices in an inviscid three dimensional flow field neither begin nor end in the fluid; they must either be infinitely long or form a

closed path [26]. Therefore, the vortex filaments cannot simply come to an end at the wingtips, but instead bend around them in accordance with Bernoulli's theorem (i.e. from p_{lower} to p_{upper}) and extend downstream to infinity. While these so-called tip vortices are particularly strong near the wingtips they gradually dissipate downstream of the wing due to viscous effects (Fig. 3.8).

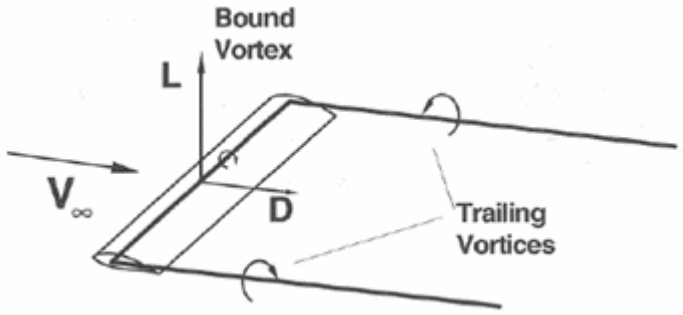

Fig. 3.8: Three-dimensional wing modelled with trailing vortices [26].

3.3 Induced Drag

Induced drag is an inevitable consequence of the production of lift on any finite-span wing. It is generated by the airflow circulation around the wing, as high pressure air particles joins low pressure air particles at the trailing edge and wingtips. As was discussed previously, the resulting vortices deflect the air particles downwards at these locations, causing a reaction known as *downwash*. As a result, the local angle of attack of the wing is increased and an additional, downstream-facing component to the aerodynamic force over the wing is created (Fig. 3.9). This additional force is called the induced drag because it has been "induced" by the action of these vortices. As the air pressure differential increases with an increase in angle of attack, larger vortices form and consequently induced drag increases [8, 11].

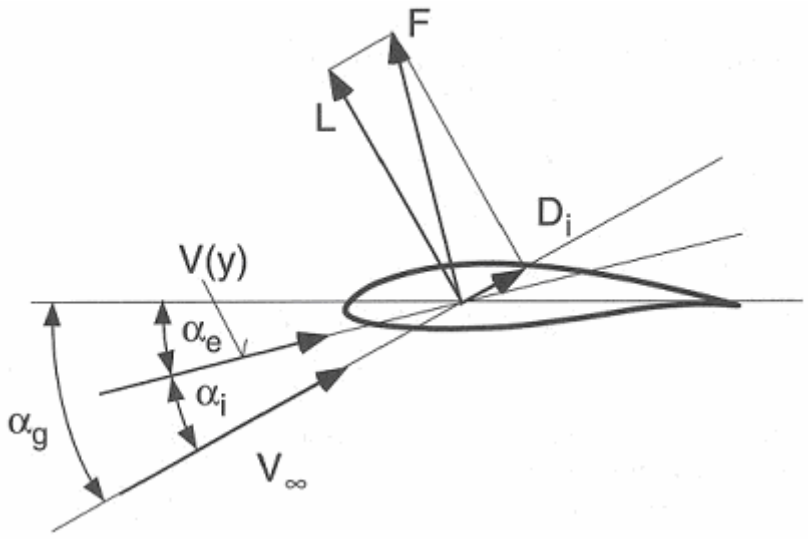

Fig. 3.9: Local velocity and force vectors of a cross sectional three-dimensional wing [26].

α_g	geometric angle of attack
α_e	effective angle of attack
α_i	induced angle of attack
D_i	induced drag
L	lift

3.4 Viscous Effects and Boundary Layers

3.4.1 Reynolds Number and Boundary Layer

Although the boundary layer is very thin and extends over only a small portion of the flow field around the aircraft, it plays an important roll in determining a number of aerodynamic characteristics. Drag and separation-related phenomena such as the maximum lift coefficient can be explained only with reference to the boundary-layer theory.

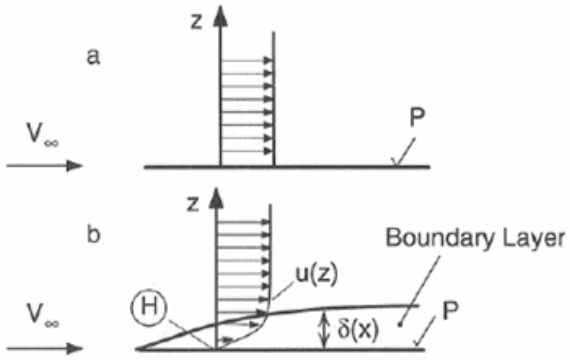

Fig. 3.10: Flow over flat plate [17].

(a) inviscid flow
(b) viscous flow
(H) no slip condition
δ(x) boundary-layer thickness
u(z) velocity profile within boundary layer

As discussed earlier, inviscid flow assumes that the flow field extends to the surface of the body, with no decrease in velocity as the surface is approached. In reality, a boundary layer exists adjacent to the body in which the velocity diminishes from the local flow velocity down to zero at the surface (Fig. 3.10). This so-called *no-slip condition* results from the fact that the air can interact with the surface at a molecular level, even when the surface is highly polished. Starting at zero velocity at the surface, within the boundary layer, the velocity gradually increases from zero at the surface to the velocity predicted by inviscid potential flow. The velocity distribution within the boundary layer is known as the *velocity profile.* The *boundary-layer thickness* is defined as the distance from the surface to the location at which the velocity reaches 99% of its local potential-flow value.

Boundary layers are classified as *laminar, turbulent,* and *separated.* In a laminar boundary layer, the air particles travel along smooth streamlines parallel to the surface.
The velocity varies within the boundary layer, giving rise to shear stresses and loss of kinetic energy in the flow (Fig. 3.11).

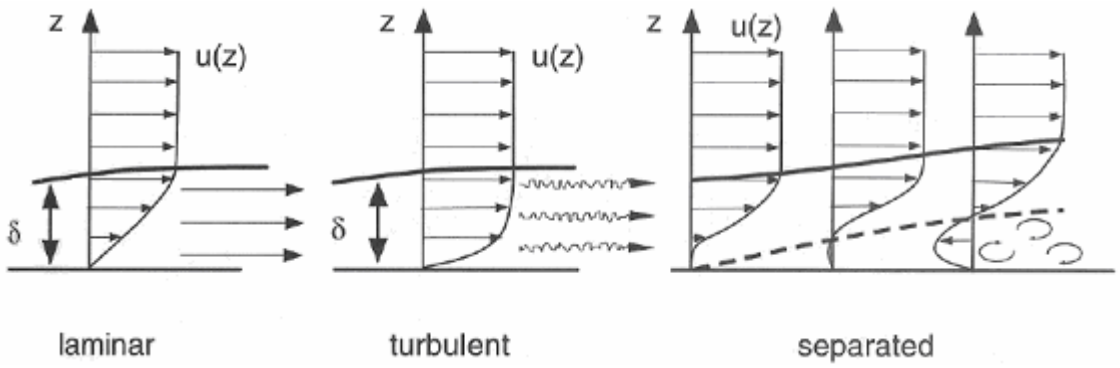

Fig. 3.11: Velocity profiles and particle motions for laminar, turbulent, and separated boundary layers [26].

In a turbulent boundary layer, the air particles undergo additional high-frequency velocity variations of a random nature. Although these variations are small compared to the average velocity, they contribute to the energy exchange between the boundary layer and the external flow, as well as within the boundary layer itself. The velocity profile in a turbulent boundary layer is thus "fuller" than that of a laminar boundary layer, exhibiting higher velocities near the surface and a steeper velocity gradient at the surface itself. With increased velocity gradients comes increased shear stresses, so that in general, turbulent boundary layers produce higher skin friction than laminar boundary layers [17].

3.4.2 Separated Flow

In the presence of an adverse pressure gradient, the boundary layer may separate from the surface of the body. This is a result of the kinetic energy differential between the inner and outer segments of the boundary layer. Given this, even a small increase of pressure may cause the fluid particles near the wall to stop and consequently turn back to form a recirculating flow region. When this happens, the flow travels away from the surface in a chaotic fashion, at a position defined as the *separation point*. Separated flow is often characterised by large-scale unsteady turbulence with no clearly defined streamlines.

Separation is largely a function of the airfoil geometry and angle of attack. It is always present on wings at high angles of attack and significantly limits the maximum attainable lift. At the same time, the airfoil drag increases due to changes in the static pressure distribution [29].

3.4.3 Boundary-layer Transition

Generally, the boundary layer on most airfoils begins as laminar and attached, and may then progress in sequence to laminar/separated, turbulent, or turbulent/separated. This process evolves because laminar flow is only stable under certain conditions, and so as a result of change to these conditions, the boundary layer will translate to a turbulent state after a certain distance.

As discussed previously, both laminar and turbulent boundary layers may separate in the presence of an adverse pressure gradient. However, since turbulent boundary layers are characterised by increased energy transfer with the flow outside the boundary layer, they are better able to overcome adverse pressure gradients without separation. Laminar boundary layers, on the other hand, may separate in the presence of relatively small adverse pressure gradients.

The exact position of this phenomenon or in fact whether it occurs at all is dependent on a large number of parameters. Such parameters include airfoil geometry, angle of attack, Reynolds number, freestream conditions and surface quality (Fig. 3.12). Since large drag penalties are incurred due to separation, care must be taken to ensure that the transition from laminar to turbulent occurs as far back on the airfoil as possible and before the conditions for boundary-layer separation are reached. This is usually accomplished by tailoring the airfoil geometry so that the boundary-layer remains laminar at both low and high angles of attack as well as throughout a range of Reynolds numbers [5].

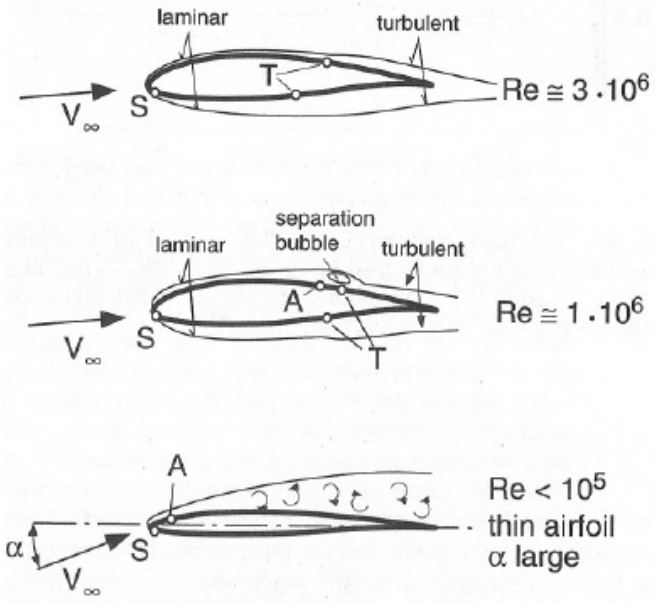

Fig. 3.12: Behaviour of laminar boundary layer for full size airfoils under various pressure distributions and Reynolds numbers [17].

3.4.4 Friction Drag and Pressure Drag

The shear stresses associated with the boundary layer act in a direction parallel to the local surface, and when integrated over the entire surface of a body, they yield the quantity known as *friction drag.* Friction drag is present with both laminar and turbulent boundary layers and is a result of the interaction between air particles and solid bodies. Because of this interaction, it is found that the magnitude of the friction drag is inversely proportional to the fluid velocity. For example, at low Reynolds numbers the boundary-layer is laminar and thus the drag experienced is almost entirely due to friction. On the other hand, at high Reynolds the boundary-layer becomes turbulent providing less interaction between the fluid particles and the solid body, and thus lower amounts of friction drag.

Another additional stress acting perpendicular to a body's surface is caused by the local static pressure. The resulting effect of this stress yields a quantity known as *pressure drag*. Pressure drag is due to variances in the fluid pressure surrounding a body. As a body travels through a fluid, or a fluid travels around a body, the fluid is displaced due to the inability of the body and fluid to occupy the same space. As a result, the fluid velocity decreases as it approaches the body. Due to Bernoulli's principle, this creates an area of high pressure. As the fluid particles continue around the body their velocity rapidly increases to match that of the freestream flow. As discussed previously, when the pressure gradient between the inner and outer edges of the boundary-layer becomes too great, separation occurs. As a result of this separation, a thick turbulent wake is created behind the body. The resulting pressure differential between the low pressure turbulent wake and the high pressure area at the front of the body causes a vacuum like situation whereby the low pressure wake acts to suck the body back consequently opposing its forward motion [11, 26].

Fig. 3.13:Pressure drag due to separation (cylinder) and friction drag due to boundary layer (flat plate) [17].

3.4.5 Importance of Surface Quality

Surface roughness is essentially a field of small amplitude irregularities. These irregularities affect laminar and turbulent boundary layers in different ways.

In a laminar boundary layer, irregularities exceeding a certain maximum height may cause the flow to become turbulent. This maximum tolerable roughness is termed the *critical roughness* and is a function of the Reynolds number and pressure distribution. Put simply, if the surface roughness remains below the critical value the laminar boundary-layer will remain unaffected and thus no drag penalties will be incurred (Fig. 3.14).

For turbulent boundary layers, drag begins to increase as soon as the roughness exceeds a value known as the *permissible roughness.* The permissible surface roughness is also a function of the Reynolds number. If the roughness is less than the permissible roughness, the surface is considered *hydraulically smooth*, however if the roughness is greater than the permissible roughness, the drag varies directly with the degree of surface roughness [19].

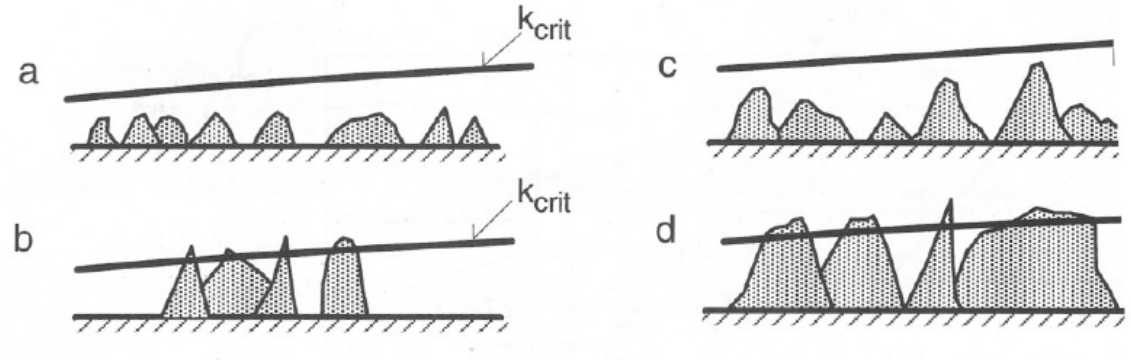

Fig. 3.14: Effect of surface roughness on laminar (a,b) and turbulent (c,d) boundary layers [26].

a) no effect
b) transition due to roughness
c) hydraulically smooth
d) increased drag due to roughness

Chapter 4

Flight Mechanics

This chapter outlines the specific information relevant to the aircraft geometry and defines a number of critical equations used throughout the design process.

4.1 Airfoil/Wing Geometry and Aerodynamic Coefficients

4.1.1 Airfoil Geometry

Since an airfoil is the cross sectional representation of a wing, its geometry is only defined in terms of the coordinates *x* and *y*. Typically, airfoil geometry is presented as a table or figure of chord wise locations, *x*, and corresponding upper and lower coordinates, z_{upper} and z_{lower}. In order to make this information independent to the size of the airfoil, the coordinates are normalized to the airfoil chord, *c*, to produce a non-dimensional or "percentage" value. Therefore, the coordinates are presented as x/c and z/c, the values of which range from zero to unity (Fig. 4.1).

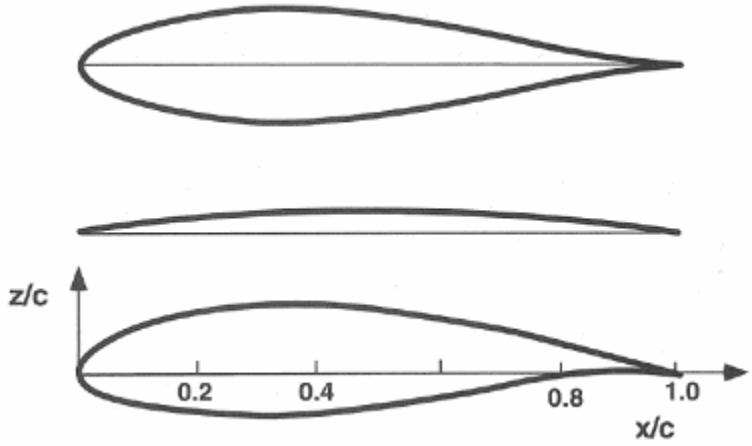

Fig. 4.1: Form, camber line and geometry of airfoil [9].

There are several essential terms used in defining airfoil geometry:

The *chord* is the shortest distance between the leading and trailing edge and the connection of which is known as the *chord line*.

The *mean camber line* is the line that is equidistant at all points between the upper and lower surfaces of the airfoil.

The *camber* is the maximum distance between the chord line and the mean camber line.

The *thickness* is the maximum distance between the upper and lower surfaces of the airfoil.

Although a fairly large set of coordinates are required to accurately specify airfoil geometry, airfoils can, to a certain extent, be characterized using just a few parameters. These parameters are illustrated in Fig. 4.2.

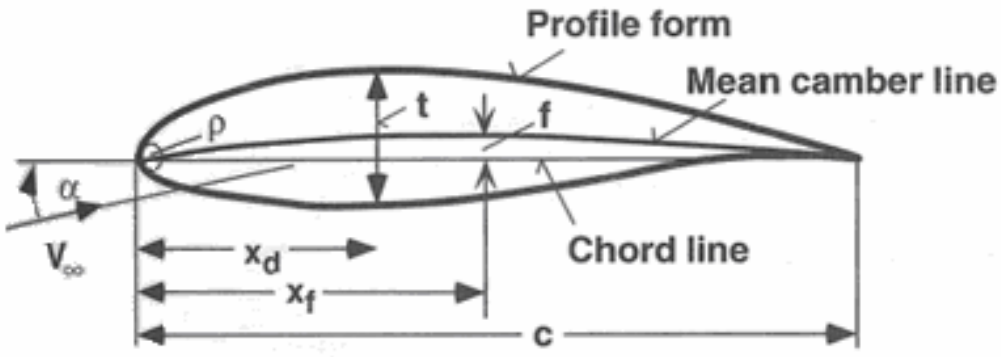

Fig. 4.2: Airfoil geometric parameters [9].

t	thickness
x_d	location of maximum thickness
f	camber
x_f	location of maximum camber
ρ	leading-edge radius
c	chord

4.1.2 Wing Geometry

A complete description of the wing includes not only the airfoil geometry, but the wing planform and the spanwise airfoil variation as well. In most cases, the leading and trailing edges of sailplane wings consist of straight line segments when viewed from above. Thus, the basic sailplane wing planforms are rectangular, tapered, rectangular/ tapered, and double or triple tapered in shape (Fig. 4.3).

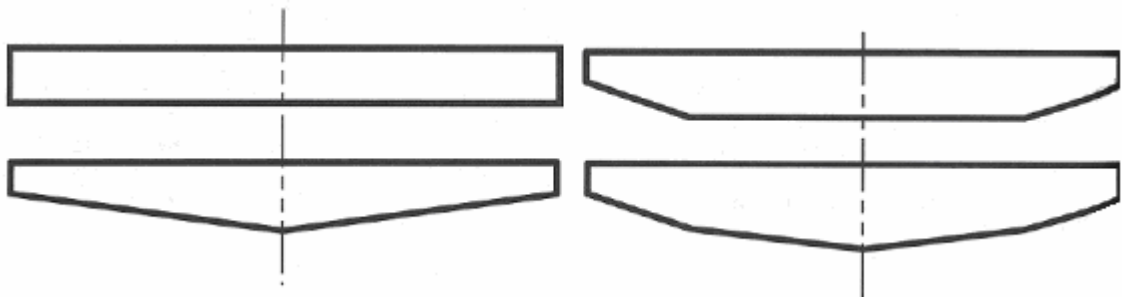

Fig. 4.3: Typical wing planforms [26].

Additionally, elliptical wing planforms are available, although seldom used in modern sailplane design. For most purposes wing planform can be defined by two geometric parameters; the aspect ratio and the taper ratio, defined as follows:

$$AR = \frac{b^2}{S} = \frac{b}{c} \qquad \text{Aspect Ratio} \qquad (8)$$

$$\lambda = \frac{c_{tip}}{c_{root}} \qquad \text{Taper Ratio} \qquad (9)$$

where b is the wing span and c, c_{root} and c_{tip} is the chord, wing root chord and wing tip chord, respectively. In the case of rectangular-tapered and double-tapered wings, these calculations become slightly more complex and extra information is generally needed to complete the wing definition.

Other important characteristic parameters include the *dihedral angle*, the angle between the wing and the *z* axis, and the wing *twist*, the spanwise variation of the geometric angle of attack. The dihedral angle, which will be discussed later in this chapter, is the used to provided lateral stability, while the wing twist aids in the generation of lift by controlling the angle of attack throughout the spanwise direction of the wing. It should be noted that the geometry of the tail surfaces are defined using similar parameters [12, 26].

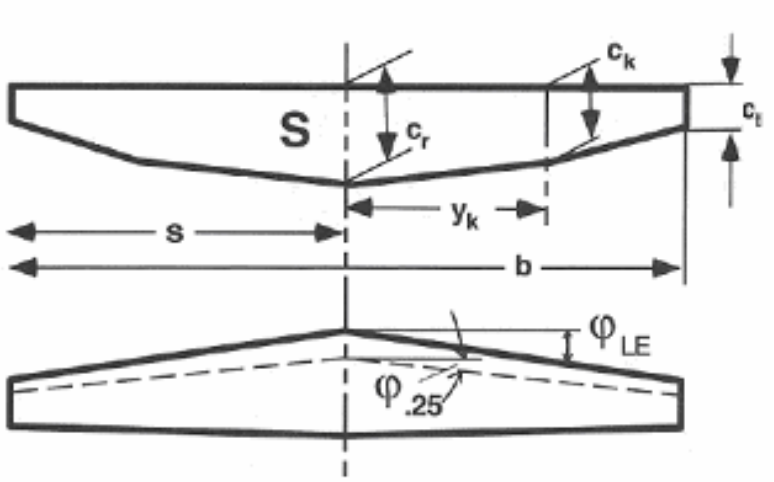

Fig. 4.4: Wing geometric parameter [].

b	span
s	semispan
c_r	root chord
c_t	tip chord
φ_{LE}	leading-edge sweep angle
$\varphi_{.25}$	sweep angle of 1/4-chord line
S	wing area
y_k	spanwise location of taper change
c_k	chord at taper change point

4.1.3 Pressure Coefficient

The aerodynamic performance of airfoil can be studied most easily by reference to the distribution of pressure over its surface. When considering this distribution, it is useful to present the pressure as a non-dimensional term known as the *pressure coefficient*. The pressure coefficient is the differential pressure between the static pressure, p_1, at a particular location in the flow field and the static pressure, p_∞, far upstream of the aircraft, normalized to the dynamic pressure q_∞. The pressure coefficient, C_P, is used primarily to represent calculated or measured airfoil pressure distributions and is expressed by the following equation:

$$C_P = \frac{p_1 - p_\infty}{q_\infty} = \frac{p_1 - p_\infty}{\frac{1}{2}\rho V_\infty^2} \qquad (10)$$

4.1.4 Aerodynamic Coefficients

The total aerodynamic force acting on a wing or airfoil can be resolved into components perpendicular and parallel to the flow, together with a moment about a prescribed reference point. These three quantities are the *lift, drag,* and *pitching moment* and are typically resolved at a point one quarter of the chord length (Fig. 4.5). It should be mentioned that if the pitching moment tends to increase the angle of attack of the wing (i.e. rotates the airfoil upwards), it is defined as positive, or "nose-up" moment. As with the pressure coefficient, the lift, drag, and pitching moment of a two-dimensional airfoil can be expressed as non-dimensional coefficients given by,

$$C_L = \frac{L}{\frac{1}{2}\rho V^2 A_p} \qquad \text{Lift Coefficient} \qquad (11)$$

$$C_D = \frac{D}{\frac{1}{2}\rho V^2 A_p} \qquad \text{Drag Coefficient} \qquad (12)$$

$$C_M = \frac{M_{c/4}}{\frac{1}{2}\rho V^2 A_p} \qquad \text{Moment Coefficient} \qquad (13)$$

where ρ and V_∞ is the density and freestream velocity of the fluid respectively and A is the planform area of the wing.

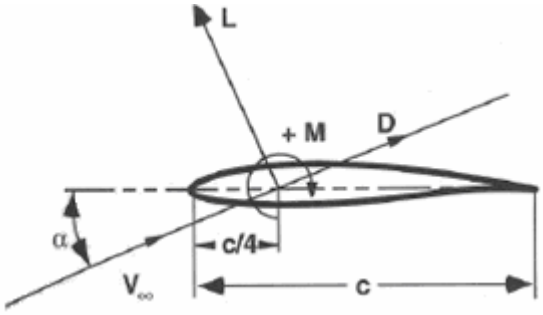

Fig. 4.5: Aerodynamic forces and moment on airfoil [26].

Experimental and theoretical aerodynamic characteristics are typically presented in a format such as Fig. 4.6 in order to highlight the variation of the aerodynamic coefficients with the angle of attack. It can be seen that as the angle of attack increases the lift coefficient also steadily increases until a maximum is reached. Further increase in the angle of attack produces a sudden decrease in C_L, known as *stall*. Accompanying this rapid decrease in C_L is a sudden rise in C_D. This is a result of the movement of the minimum pressure point and the accentuation of the pressure gradient around the airfoil caused by the increasing angle of attack.

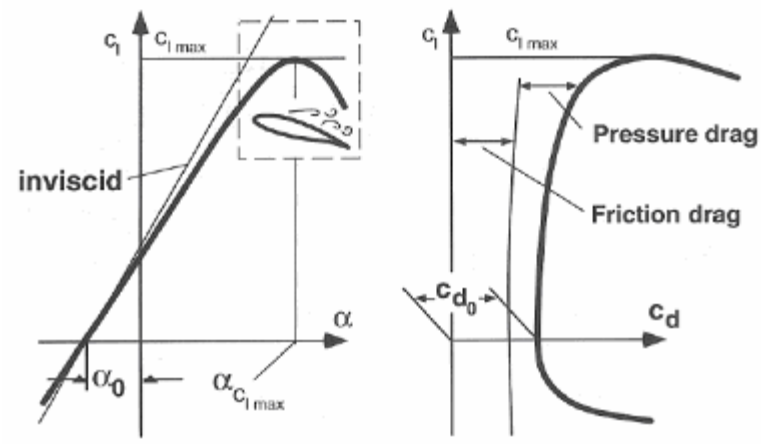

Fig. 4.6: Lift and drag polars [26].

In the case of most aircraft, little attention is paid to the moment coefficient as specific airfoils are usually selected based on their performance and stall characteristics. The negative or positive pitching moments in these aircraft are tolerated as necessary evils. The reason for this is because horizontal stabilizers with large moment arms can be easily used to neutralize these moments [26].

4.1.5 Aerodynamic Centre

Between the leading and trailing edges there exists a particular reference point about which the aerodynamic moment remains almost constant as the angle of attack varies. This reference point, the *aerodynamic center,* is located at approximately one quarter of the chord length back from the leading edge.

Since the moment about the aerodynamic center does not vary with angle of attack, the aerodynamic forces on an airfoil can be broken down into a constant pitching moment and a lift force applied at the aerodynamic center (Fig. 4.7). Although in practice the aerodynamic centre may vary slightly from the one quarter chord location, it remains of particular interest to the study of aircraft stability and control.

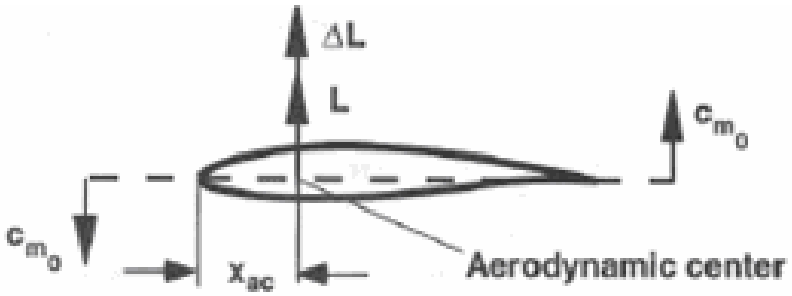

Fig. 4.7: Aerodynamic centre and zero-lift moment [26].

4.1.6 Mean Aerodynamic Chord

The *mean aerodynamic chord* is simply the average of the root and tip chord. Therefore, the mean aerodynamic chord of a rectangular wing is simply the chord. However, for a swept or tapered wing it is a little more complex and can be defined mathematically as follows or geometrically as per Fig. 4.8.

$$m.a.c = c_{\mu} = \frac{1}{S}\int_{-S}^{+S} c^2(z)\,dz \qquad (14)$$

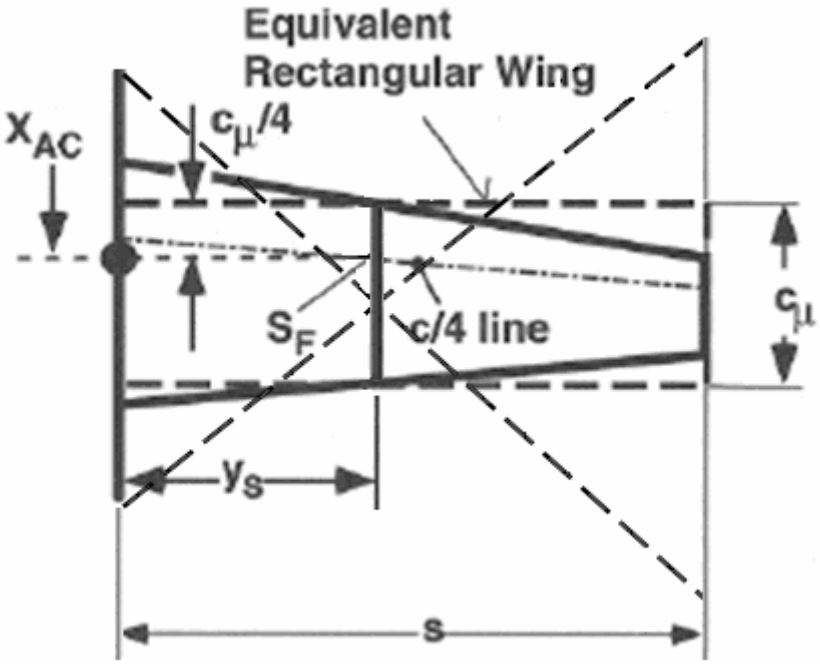

Fig. 4.8: Location of mean aerodynamic chord [32].

c_μ	mean aerodynamic chord
x_{AC}	location of wing aerodynamic center
S_F	center of mass of c/4-line, assuming local mass loading proportional to local chord
s	wing semi-span

4.2 Influences of Airfoil/Wing Geometry and Aerodynamic Performance

4.2.1 Airfoil Families

The aerodynamic properties of an airfoil are functions of its geometry, angle of attack, Reynolds number, and surface quality. The large number of geometric parameters allows the definition of a virtually unlimited variety of airfoil shapes. Because of this, designers are often faced with the difficult task of selecting airfoils based on various operational requirements, and it is therefore useful to classify airfoils systematically according to certain characteristics. To provide this system a number of *airfoil families* have been defined and their geometric and aerodynamic data tabulated in airfoil catalogues.

Over the years, several profile series have been of particular significance to sailplane designers, however many of these are now of only historical importance. Airfoils specifically intended for sailplane use were developed by a number of key contributors such as R. Eppler and F. X. Wortmann. These airfoils led to tremendous improvements in sailplane performance and quickly replaced virtually all earlier profiles.

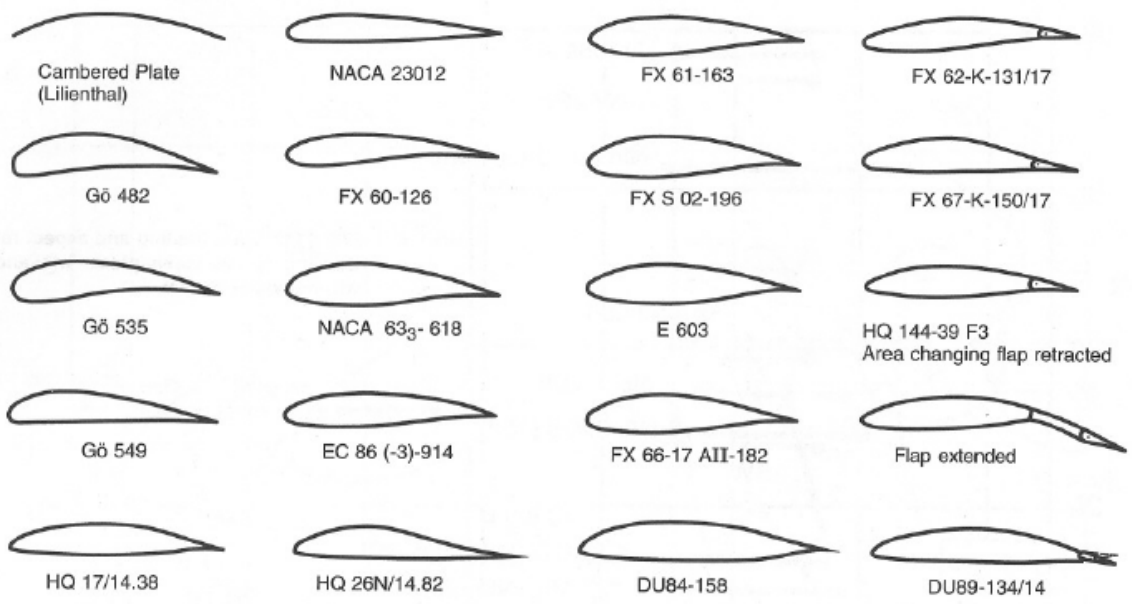

Fig. 4.9: Various airfoils [26].

4.2.2 Influence of Airfoil Geometry

Airfoil selection is critical to sailplane design, and proper airfoil selection in turn necessitates a fundamental understanding of the effects of individual airfoil geometric parameters. Two parameters of particular importance are the airfoil thickness and camber.

The effects of varying airfoil thickness are most apparent in the drag polar. Thick airfoils exhibit relatively high amounts of drag as opposed to thin airfoils where drag is considerably smaller. Thicker airfoils also increase the likelihood of boundary-layer separation, particularly as the angles of attack increases. Additionally, below around 10% thickness the maximum lift coefficient decreases as the leading edge becomes sharper, and as a result flow tends to separate at this location (Fig. 4.10).

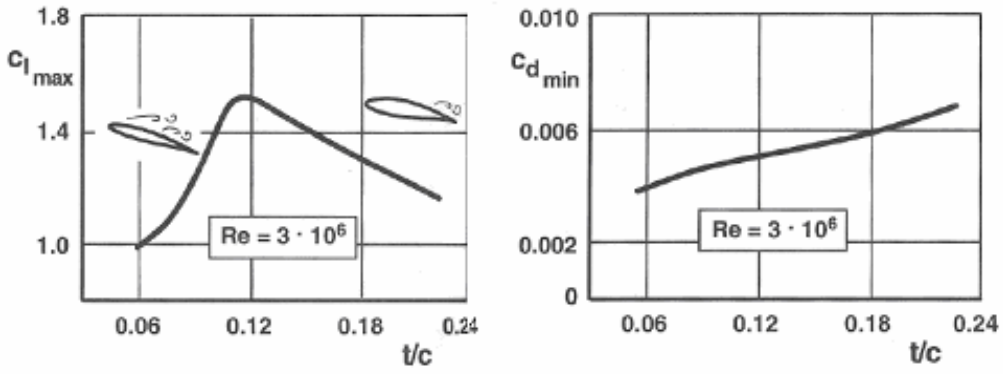

Fig. 4.10: Influence of thickness on maximum lift and minimum drag coefficients [9].

If the airfoil is cambered, the resulting asymmetry gives rise to differences in pressure distribution over the upper and lower surfaces. As the camber increases so too does the lift coefficient. Unlike the airfoil thickness, the degree of camber and the chordwise location of maximum camber have a very strong influence on the pitching moment.

4.2.3 Influence of Angle of Attack

As mentioned previously, the angle of attack can both positively and negatively affect the lift and drag distribution. Generally, increasing the angle of attack leads to the lift coefficient steadily increasing until a maximum is reached. Further increase in the angle of attack produces a sudden decrease in C_L, known as *stall*. Accompanying this rapid decrease in C_L is a sudden rise in C_D. Generally, higher angles of attack produce greater amounts lift. However, an important point to note is that particular care must be taken when determining the angle of incident, the angle of the wing relative to the fuselage. To avoid stall as a result of small instantaneous permutations, designers should ensure that the angle of incident is sufficiently lower than that of the stall angle. This phenomenon subsequently places an upper limit on the effective angle of attack and an accompanying limit on the effectiveness of the airfoil itself.

4.2.4 Influence of Aspect Ratio and Wing Taper

Aspect ratio and wing taper have a pronounced effect on lift and drag distribution. Figure 4.11 illustrates the effects of aspect ratio by comparing the lift distributions for rectangular wings of various aspect ratios.

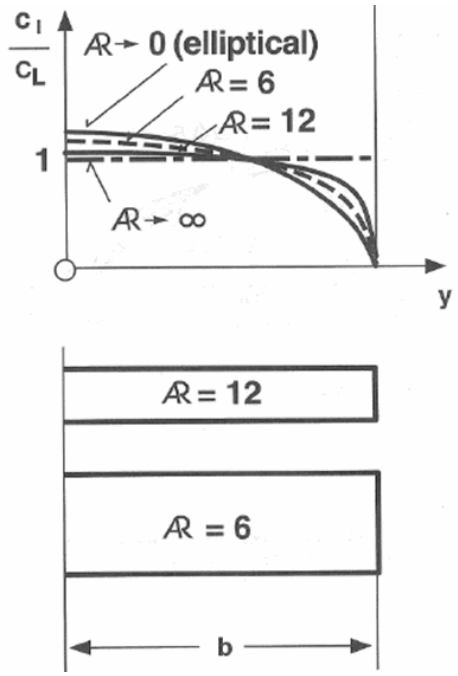

Fig. 4.11: Effect of aspect ratio on lift distribution over a rectangular wing [12].

It follows that as the aspect ratio increases the lift distribution gradually becomes elliptical (i.e. ideal lift distribution). Additionally, this same increase in aspect ratio is accompanied by a corresponding decrease in induced drag (Fig. 4.12).

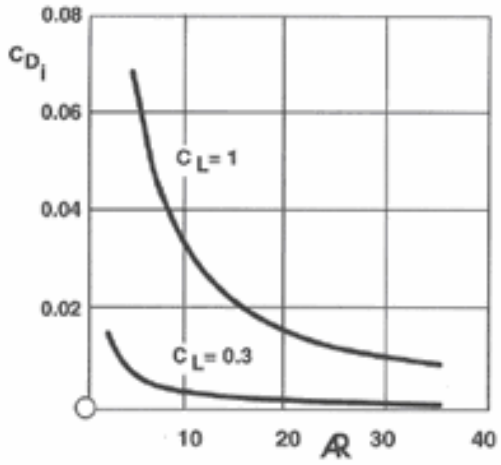

Fig. 4.12: Induced drag as a function of aspect ratio [12].

Figure 4.13 shows the influence of taper on lift distribution. The sharp increase in the lift coefficient observed near the tip of the highly tapered wing indicates that the stall will develop first in this region. For this reason, moderately tapered wings are used to ensure stall initiates near the wing root [12, 26].

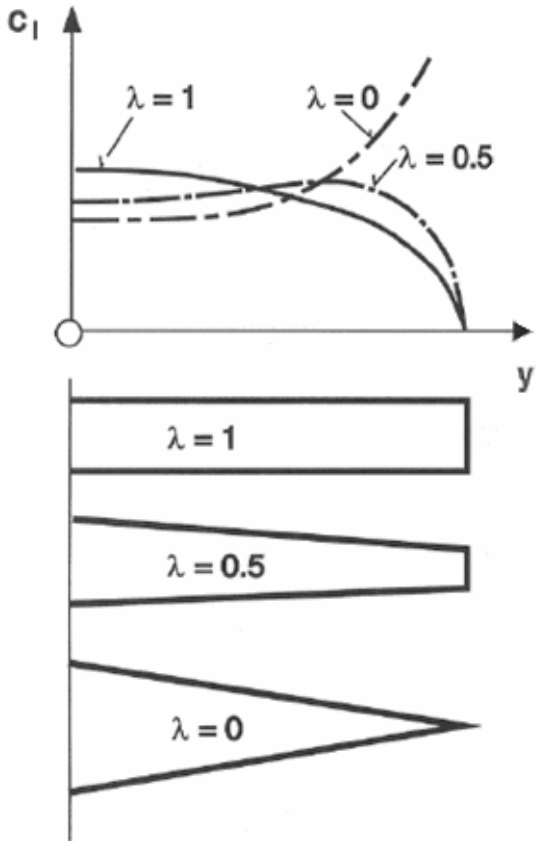

Fig. 4.13: Effect of taper ratio on lift distribution [12].

4.3 Flight Performance and Stability

4.3.1 Airspeed and Sink Rate

The aerodynamic forces acting on the sailplane may be resolved into components perpendicular to the flight path (lift) and parallel to the flight path (drag) and are expressed as:

$$L = \tfrac{1}{2} C_L \rho V_\infty^2 S \quad (15)$$

$$D = \tfrac{1}{2} C_D \rho V_\infty^2 S \quad (16)$$

In order to maintain steady level flight, the lift must equal the aircraft's weight, and a thrust, T, must be provided to balance out the drag. Since a sailplane is by definition un-powered, the thrust is equal to zero and a steady trim condition is only possible in a descending glide.

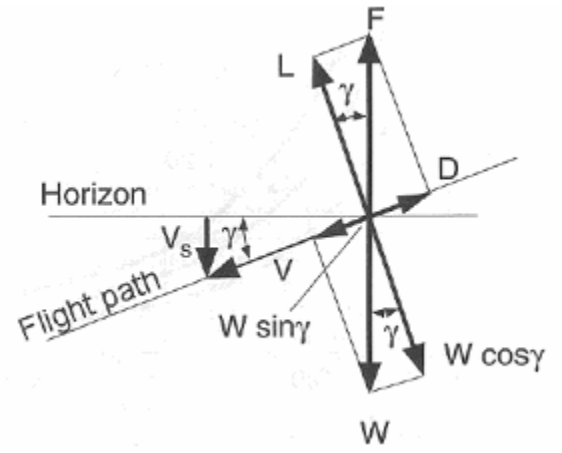

Fig. 4.14: Balance of forces in trimmed flight [2].

L	lift
D	drag
W	weight
F	resultant airload
V	flight velocity
γ	glide angle
V_S	= V sin γ

As with the aerodynamic forces, the weight of a gliding sailplane may be resolved into components perpendicular and parallel to the path of flight. In a trimmed glide at constant airspeed, the flight path angle, γ, is the angle that provides equilibrium among the individual forces (Fig. 4.14):

$$L = W \cos\gamma \quad (17)$$

$$D = W \sin\gamma \quad (18)$$

The flight path angle in a steady state glide is known as the *glide angle.* From Fig. 4.14 it follows that the lift-to-drag ratio, also known as the *glide ratio*, may be expressed as:

$$\frac{L}{D} = \frac{C_L}{C_D} = \frac{1}{\tan\gamma} \tag{19}$$

Provided most sailplanes have maximum glide ratios between 20 and 50 the corresponding glide angles lie between approximately 3^o and 1^o.

Calculating the airspeed in a steady glide is obtained by introducing the expression for the lift, Eq. 15, in the equilibrium equation, Eq. 17:

$$W\cos\gamma = \tfrac{1}{2} C_L \rho V_\infty^2 S \tag{20}$$

Sailplane glide ratios are usually so large, and the flight path angles γ so small, that one may assume $\cos\gamma = 1$ with negligible error. Introducing this small angle assumption into the previous equation leads to:

$$V = \sqrt{\frac{2}{\rho}\frac{W}{S}\frac{1}{C_L}} \tag{21}$$

This equation, which relates the airspeed to the wing loading, W/S, and the lift coefficient C_L, is of fundamental importance to sailplane performance analysis. Figure 4.15 graphically illustrates this equation. It should be noted that at high speed, a small change in lift coefficient corresponds to a large change in airspeed, and at low speed, a large change in lift coefficient corresponds to a small change in airspeed. These relationships are extremely important when selecting airfoils for specific conditions.

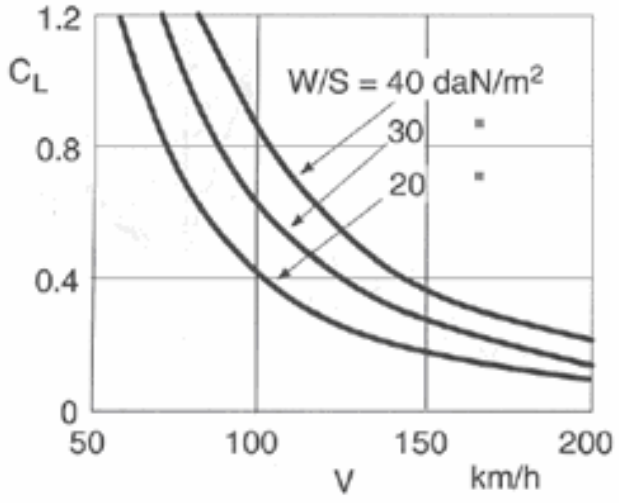

Fig. 4.15: Relationship between airspeed and lift coefficient for various wing loadings [26].

Another important equation illustrates the sink speed, V_s, of the sailplane and is obtained from the glide angle and the flight velocity:

$$V_s = V \sin\gamma \tag{22}$$

Introducing the expression for V into this equation as well as the usual small angle assumptions, $\sin\gamma = \tan\gamma = C_D/C_L$, leads to the sink speed in steady gliding flight:

$$V_s = \frac{C_D}{C_L^{3/2}}\sqrt{\frac{2W}{\rho S}} \tag{23}$$

This equation clearly illustrates that the sink rate is directly affected by changes in the wing loading.

4.3.2 Stability

A sailplane in steady level flight is said to be in equilibrium. That is, the lift and drag exactly balance the components of weight, and all the moments about the center of gravity sum to zero (Fig. 4.16).

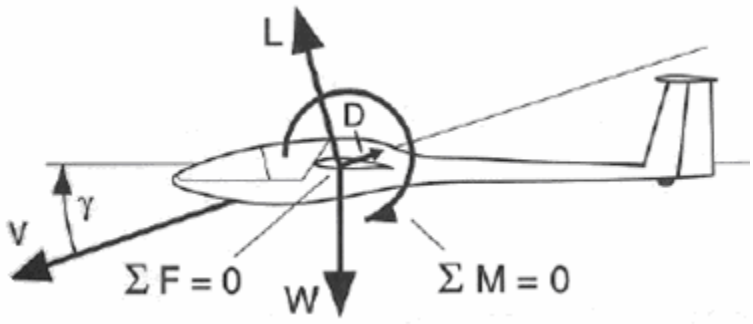

Fig. 4.16: Equilibrium in un-accelerated flight [21].

A sailplane's behaviour can thus be classified under two régimes, *Static stability* and *Dynamic stability*. Static stability is present if a disturbance in the equilibrium condition results in a restoring force, that is, a force that immediately opposes the disturbance. Dynamic stability, on the other hand, requires that the subsequent motion after the disturbance is stable, that is, it is gradually dampened out (Fig. 4.17). It is important to note that an aircraft may exhibit dynamic instability even if it is statically stable.

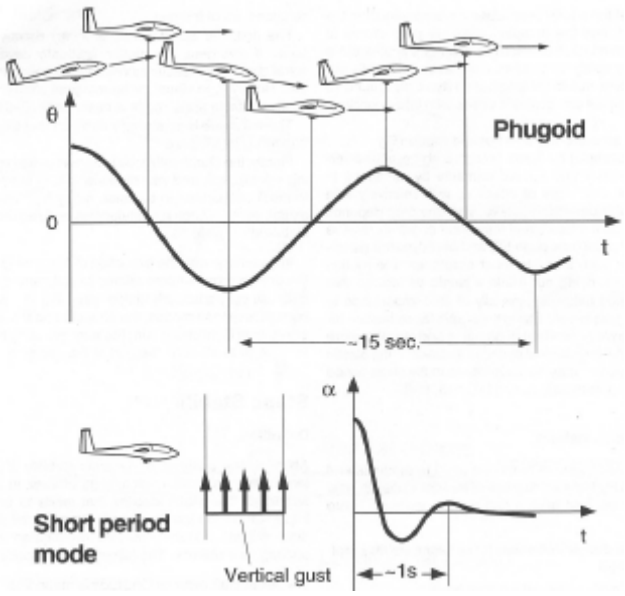

Fig. 4.17: Phugoid and short period modes [26].

Because sailplanes invariably exhibit lateral symmetry, the stability analysis may be divided into two independent problems, *Longitudinal stability and Lateral stability*. Longitudinal stability is the stability of motion in the sailplane's plane of symmetry, that is, forward velocity, pitch, and angle of attack. Lateral stability considers motions occurring out of the plane of symmetry such as slipping, rolling, and yawing (Fig. 4.18).

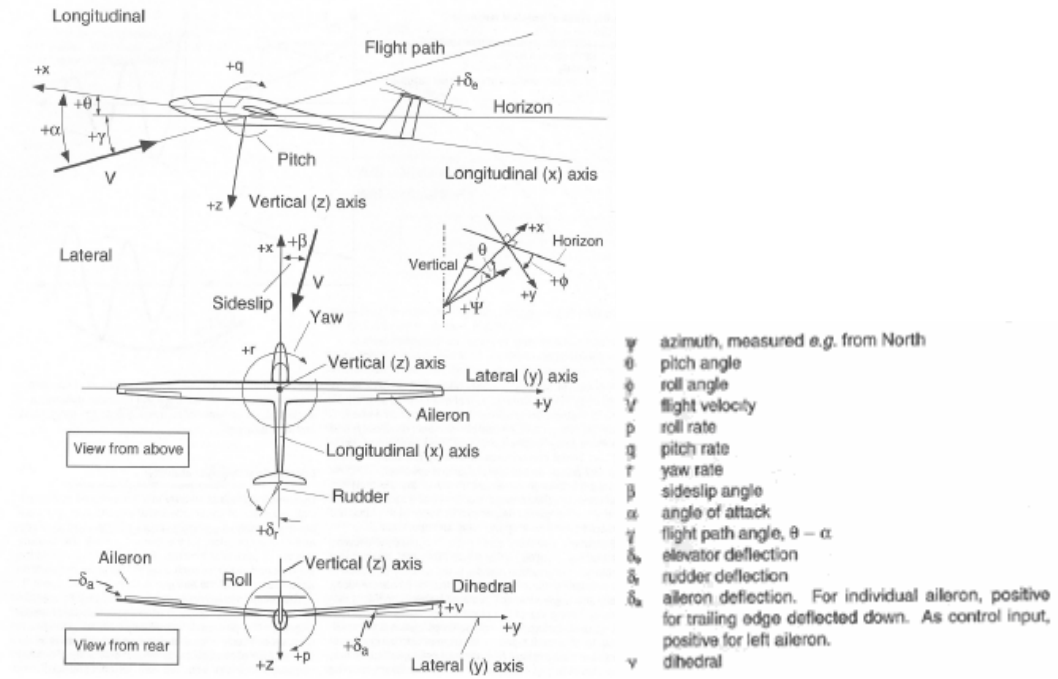

Fig. 4.18: Lateral stability definitions [26].

Another important criterion in stability analysis is the stability margin. The stability margin is simply a measure of aircraft stability and is defined as,

$$\text{Stabilty Margin} = \frac{\left(x_N - x_{CG}\right)}{c_\mu} \tag{24}$$

Where x_N and x_{CG} are the longitudinal positions of the aircraft neutral point (the point about which the sum of the aerodynamic moments is independent of the lift coefficient) and centre of gravity respectively and c_μ is the mean aerodynamic chord (Fig. 4.19).

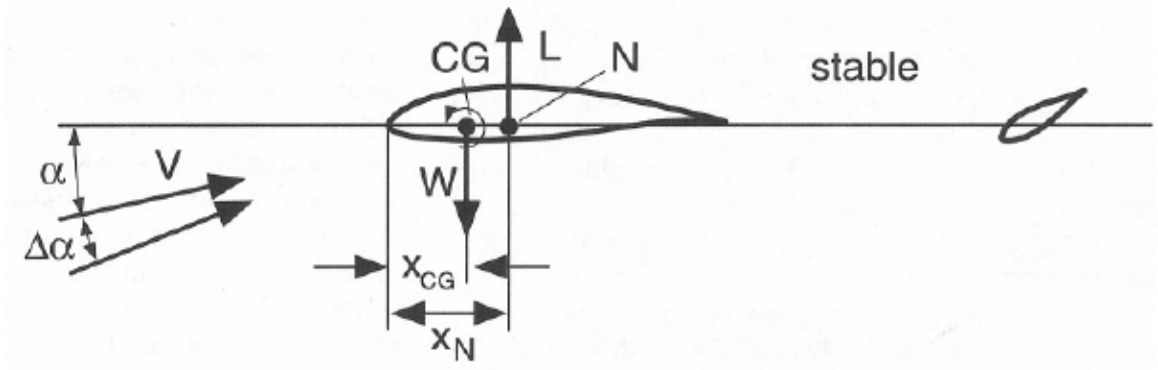

Fig. 4.19: Location of aircraft neutral point and CG in stable configuration [21].

The greater the stability margin, the greater the tendency of the aircraft to return to its equilibrium condition following a perturbation. For example, an aircraft where the stability margin is very low requires very little stabilizer lift to change the equilibrium coefficient of the aircraft. As the stability margin increases, higher stabilizer lift forces are required. For this reason, sailplanes are typically designed with extremely low stability margins where the CG is very close to the neutral point, often within only 5-10% of mean aerodynamic chord [21, 26].

4.4 Aeroelasticity

4.4.1 Static and Dynamic Aeroelasticity

The preceding discussion of stability assumes the sailplane to be a rigid body. *Aeroelasticity*, on the other hand, considers the static and dynamic interactions between the elastic structure of the aircraft and the surrounding air flow. Although aeroelasticity is beyond the scope of this thesis, it is a topic of considerable importance to sailplane design and it therefore essential to familiarize oneself with the basic concepts.

As with flight mechanics, it is convenient to divide aeroelastic problems into static and dynamic phenomena. Static aeroelasticity is the progressive reaction of the aircraft structure to flex without limit. Important to this process is the existence of a spanwise elastic axis along which a transverse load (lift) may be applied without inducing twist. If an upward load is applied ahead of the elastic axis a nose-up twist will be generated. Thus, if the local aerodynamic center lies ahead of the elastic axis, any increase in lift will lead to an increase in the wing angle of attack, in turn leading to additional lift, and so forth. At a sufficiently high airspeed, linear theory predicts that the wing will bend and twist without limit. In practical terms, the wing structure will fail.
Dynamic aeroelasticity, on the other hand, is the unstable oscillation of the aircraft structure known as *flutter*. Flutter is a result of in flight structural deformations associated with the aircrafts natural frequencies and mode shapes. These mode shapes produce aerodynamic loads that change the dynamic behaviour of the aircraft. Therefore, the stability and in fact the structural integrity of the complete system depend entirely on the degree and nature of these loads [20].

Chapter 5

Design Requirements and Optimisation

The first step in designing any aircraft is ultimately understanding what it will be expected to do. In line with this, it must be ensured that the design perform optimally within these realms. This chapter discusses the conflicting requirements of sailplane plane design and establishes methods of determining optimal performance throughout individual sections of the aircraft.

5.1 Aerodynamic Design Requirements

5.1.1 Airfoil Selection

The most important aspect of aircraft design is undoubtedly airfoil selection. While the airfoil itself is a seemingly minute feature, it in fact controls the entirety of the aircrafts performance. It is therefore crucial that the selected airfoil match the intended purpose of the aircraft. For instance, in the case of a sailplane it is essential that the airfoil design display a number of unique/exceptional properties. Such properties include:

- A high maximum lift coefficient in low speed flight,
- Exhibit low drag in high speed flight,
- Have a high L/D ratio, and
- Have good stall characteristics,

While these properties are easily definable, selecting an appropriate airfoil usually requires a careful balance between conflicting requirements. To aid in this process, airfoil selection can be broken down into several simple steps. These steps include:

1. Aerodynamic Polars – The first step in airfoil selection is the generation of lift and drag polars for individual profiles throughout a range of expected flight speeds.

2. *L/D Ratio* –The single most important aspect of any sailplane airfoil is that it portrays a relatively high lift to drag ratio over a range of flight speeds and angles of attack. Generally, the maximum value should be higher than 40 in order to ensure optimal performance. This can easily be determined by observing the

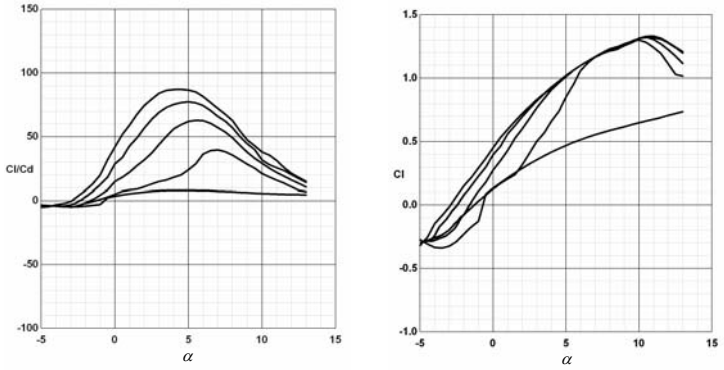

$\frac{C_L}{C_D}$ *vs.* α plot (Fig. 5.1).

Fig. 5.1: Lift and drag polars.

3. *Angle of Attack* – The next step involves determining the most appropriate angle of attack. This angle is found by calculating the average angle of attack of the maximum L/D ratio values, over the range of expected flight speeds. Generally, this value should be as low as possible, usually in the range of 3-5 degrees. As a matter of interest, this angle will latter become the angle of incident between the wing and fuselage.

4. *Stall Characteristics* – Once the optimal angle of attack is determined, the stall characteristics of the airfoil can be established. This is accomplished by ensuring that the previously determined angle does not lie in the vicinity of the stall angle of attack. Generally, if stall initiates within 3 degrees of the optimal angle of attack the airfoil should be avoided. This can be observed simply by referring to the C_L *vs.* α plot (Fig. 5.1). Additionally, another important aspect is the way in which stall develops. Generally, it is preferred that stall develops slowly through a range of angles of attack rather than sharply drop-off after $C_{L\max}$. This is preferred as that in the event of stall developing, the aircraft will remain somewhat stable and the pilot may attempt to control the aircraft rather than it quickly plummeting into a stall induced dive. Examples of this can be observed in Fig. 5.2.

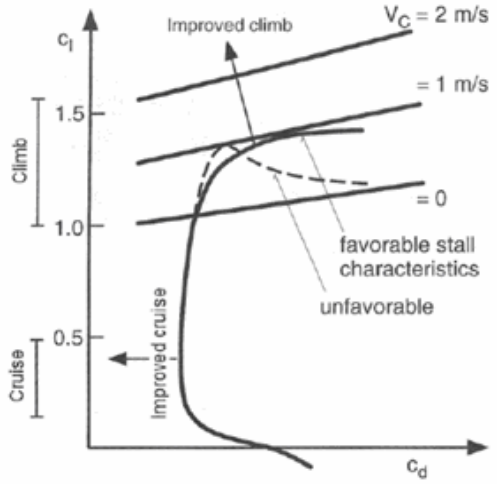

Fig. 5.2: Desirable aerodynamic characteristics for sailplane airfoils [26].

5. *Thickness* – Appropriate thickness is essential in airfoil selection as it accounts for a large percentage of the structural strength. As well as this, thicker airfoils provide more room for control linkages and ballast. Appropriate thickness' range from 12-18%.

6. *Lift* – Finally, the airfoil should be tested to ensure it will produce enough lift to achieve flight at the expected flight speeds. This can be easily determined by using the following equation and calculating the approximate aircraft weight and wing area:

$$Mg \le \tfrac{1}{2} C_L \rho V^2 S \qquad (25)$$

While these steps provide an excellent basis, selecting an appropriate airfoil will still remain an extremely difficult procedure. However, experimentation has shown that

airfoils from the Horstmann and Quast families provide extremely favourable characteristics for most forms of sailplane flight [9].

5.1.2 Aspect Ratio

The aspect ratio is defined in terms of the wing area and span. Consequently, changes in either the chord and/or span drastically influence the aspect ratio (Fig. 5.3). In addition, increasing the aspect ratio not only increases the wing area but also increases the structural weight, torsional stresses and consequently the manufacturing cost. However, the most important affect of either increasing or decreasing the aspect ratio is undoubtedly its influence on both profile and induced drag.

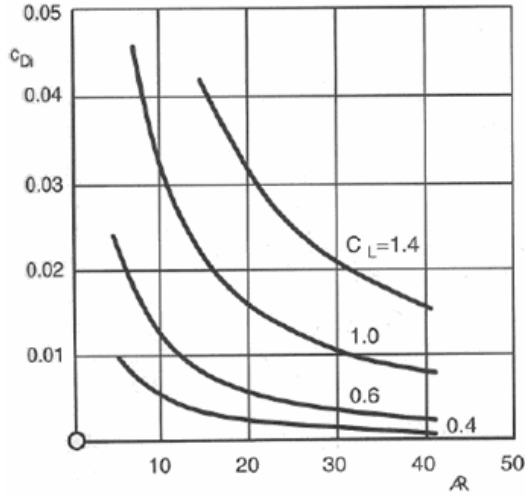

Fig. 5.3: Induced drag coefficient vs. aspect ratio for varying C_L [12].

As can been seen in Figs. 5.3-5.4, induced drag significantly decreases as aspect ratio increases, while parasitic drag increases linearly. This is because as the aspect ratio increases the tip vortex produced "downwash" has less local wing area to enact on, leading to lower induced drag while the accompanying increased surface area results in both increased friction and pressure drag and thus increased parasitic drag.

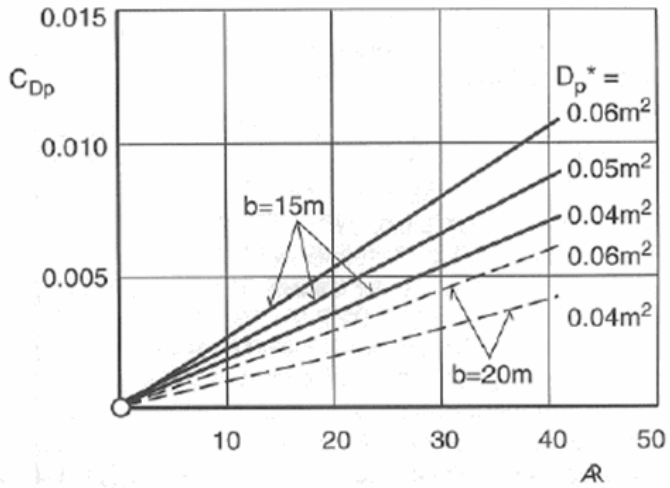

Fig. 5.4: Parasitic drag vs. aspect ratio [12].

These relationships can also be determined mathematically using the following equations,

$$C_{D_i} = \frac{C_L^2}{\pi ARe} \tag{26}$$

$$C_{D_p} = \frac{S}{b^2} AR \tag{27}$$

Where *e* is the Oswald *span efficiency factor*. The efficiency factor is equal to 1.0 for an elliptic wing and is some value less than 1.0 for any other planform. A typical value for a rectangular wing is approximately 0.70.

Naturally, it is evident that a careful balance between induced and parasite drag must exist. However, because of the strong effect of lift on induced drag (Fig. 5.3), the aspect ratio for minimum drag varies considerably. For example, at high lift coefficients and consequently high speeds, the induced drag dominates and the minimum drag occurs at relatively high aspect ratios. On the other hand, at lower lift coefficients and consequently low speeds, the profile drag becomes more important, and optimisation favours lower aspect ratios. Figure 5.5 illustrates this relationship between differing design lift coefficients and optimum aspect ratios.

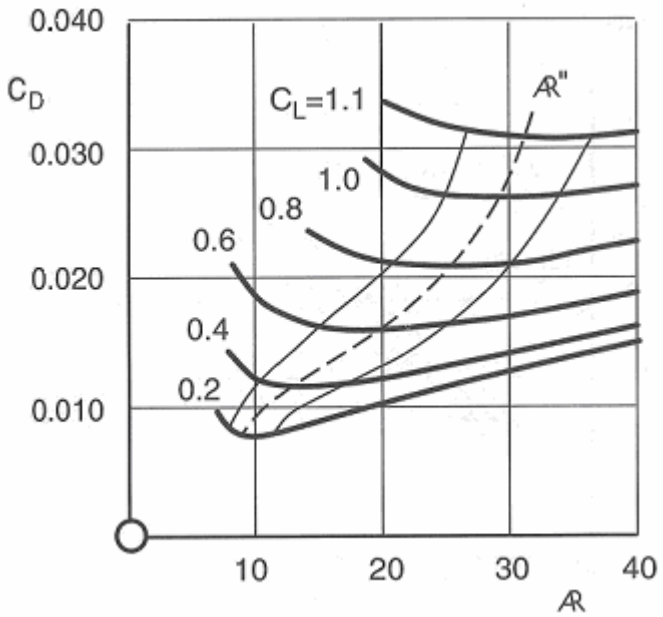

Fig. 5.5: Effect of aspect ratio and lift coefficient on total drag [12].

Unfortunately, the selection of an optimum aspect ratio for varying flight conditions remains a difficult problem. However generally, sailplanes require larger aspect ratio usually in the range of 30-40 as these ratios provide slower glide speeds and less sensitive flight control [26].

5.1.3 Wing Planform

As discussed in the previous chapter, wing planform considerably affects spanwise lift distribution. This, in turn determines the amount of induced drag as well as the stall characteristics of the wing. As we know, elliptical wings provide optimal lift distribution as well as ensuring to minimise induced drag, however, they are considerably difficult to manufacture and are therefore generally not employed in most aircraft.

This, along with the considerable ease in manufacturing aerodynamic surfaces defined by straight lines, means that nearly all modern sailplane wing planforms are fabricated from rectangular and trapezoidal sections. Nevertheless, in order to approximate an elliptical planform, several trapezoidal sections can be combined to produce what is known as double and triple tapered planforms.

While replicating the elliptical planform provides exceptional lift qualities, it also replicates their unforgiving stall characteristics. Therefore, in order to ensure favourable stall characteristics, sailplane wings are generally designed so that flow separation occurs first over the inboard sections of the wing. This preventative measure ensures that the loss of aileron controls is significantly decreased, and also reduces the tendency of the aircraft to "fall off" on one wing and enter a spin.

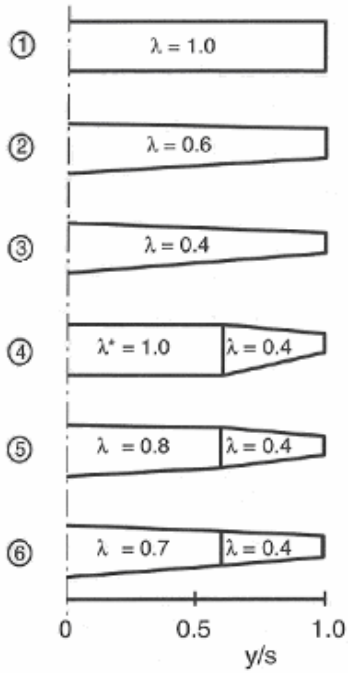

Fig. 5.6: Variations of wing planforms [24].

By avoiding short, thick low aspect ratio and highly tapered wings and incorporating more progressively tapered, high aspect ratios wings, higher performance can be more easily attained. Both theoretical investigations and practical experiments suggest that tapered wings with a taper ratio of 0.4 :1 and double tapered wings with a taper ratio of 0.4:0.8:1 and a taper break at z/s=0.6 yield especially good results (Fig. 5.6).

5.1.4 Wing Loading

Unfortunately, optimal wing loading is a function of the meteorological conditions. Figure 5.7 shows cross-country speed vs. wing loading and span for four thermal models. As can be seen, the optimum wing loading varies considerably depending on the particular thermal model. While the wide/weak and narrow/strong thermals (*B1* and *A2*), favour a wing loading between 25 and 35 daN/m^2, the *B2* (wide/strong) requires a very high wing loading (over 40 daN/m^2) and the *A1* (narrow/weak) thermal an extremely low wing loading (under 20 daN/m^2).

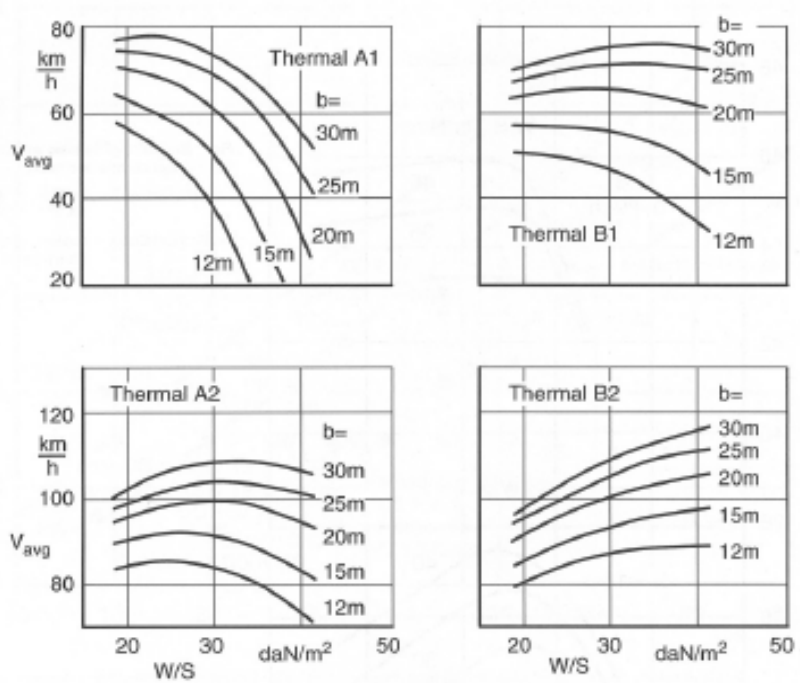

Fig. 5.7: Effect of span, aspect ratio and wing loading on average cross-country speed [26].

Compared with meteorological assumptions, wingspan and aspect ratio have relatively little effect on the choice of wing loading. The reasonably consistent effects of these design parameters, namely that higher wing spans and aspect ratios favour higher wing loadings, make them relatively easy to account for during the design process.

The influence of aspect ratio and wing loading on cross-country speed is well illustrated in Fig. 5.8, which shows the effects of deviating from the optimum combination. If the optimal regions from each of the figures are combined into a single chart (Fig. 5.9), it becomes evident that, while the aspect ratio may be selected to provide good performance in all weather conditions, the optimum wing loading varies considerably.

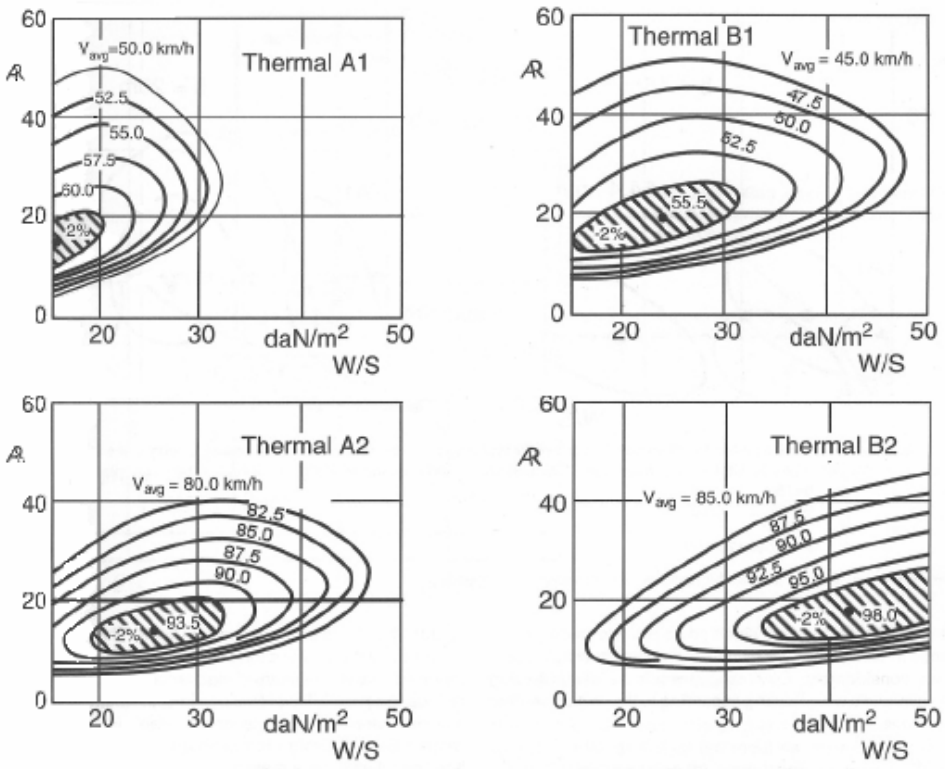

Fig. 5.8: Average cross-country speed as a function of aspect ratio, wing loading and thermal model [26].

Put simply then, choosing the optimal wing loading equates to defining the weather conditions in which the sailplane will be likely to perform. To over come these issues however, most modern high performance sailplanes are delivered with provisions for water, or solid ballast.

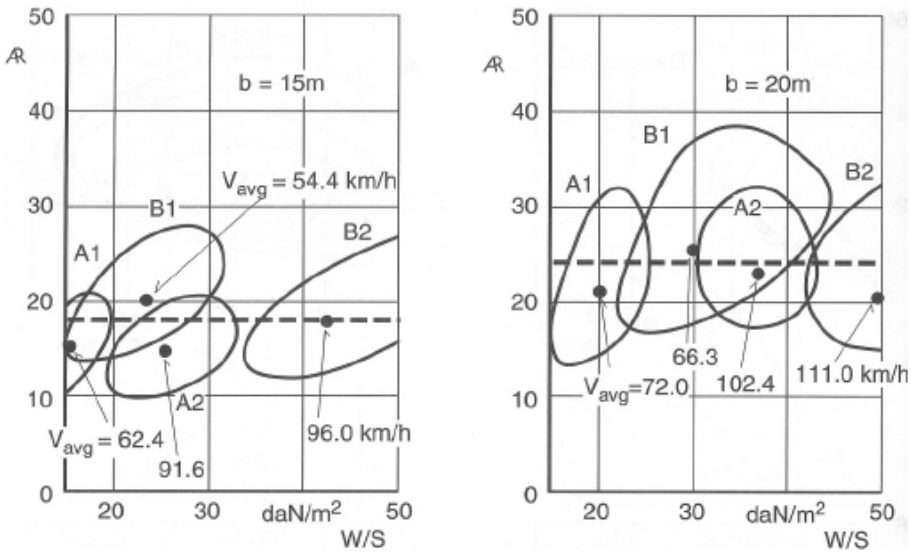

Fig. 5.9: Combination of wing loading and aspect ratio yielding near-optimum average cross-country speed [26].

– – – – – Aspect ratio for highest average cross-country speed.

Therefore, to ensure optimal performance can be gained, the zero-ballast wing loading should be held as low as possible to allow for good weak-weather performance, and the ballast capacity should be as large as possible to allow the wing loading to be increased in strong weather conditions.

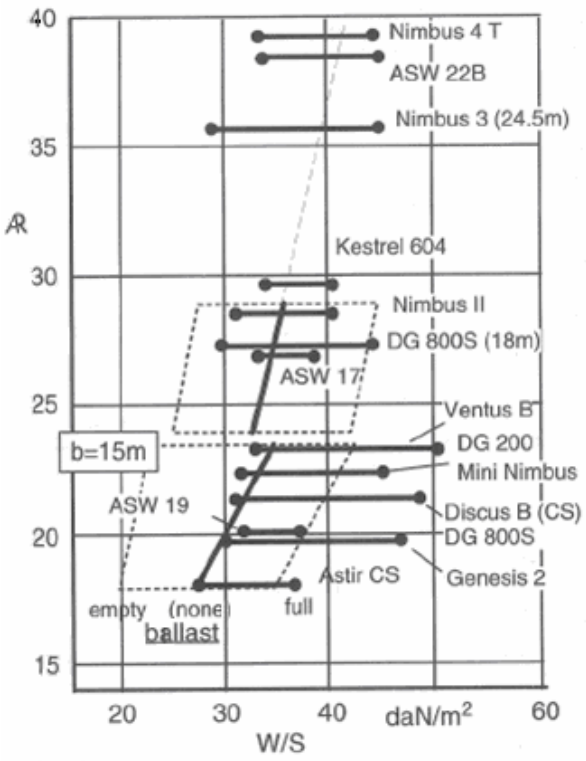

Fig. 5.10: Optimal wing loadings for various sailplanes [26].

Based on these considerations, it is possible to define a range of combinations of aspect ratio and wing loading representing a reasonable compromise for cross-country performance in varying weather conditions (Fig. 5.10).

5.1.5 Winglets

Despite high aspect ratios and carefully optimised wing planforms, induced drag still remains a significant source of drag on finite wings. One possible method of reducing induced drag is through the optimisation of wingtip geometry. One such approach employs winglets, small aerodynamic surfaces extending upwards from the wingtip, designed to both produce additional lift, stability and reduce the effects of downwash.

Fig. 5.11: Various winglet configurations [7].

According to the simplest theory, winglets allow some of the wing vortices to continue into the wingtip where they are trailed away from the plane of the wing. In doing so, the wingtip vortex filament has less wing area to enact on and consequently less intensity. Furthermore, by extended the winglet perpendicular to the wing plane, a small root moment is produced and consequently additional lift and lateral stability can be gained. Thus, by trailing some of the vortices away from the plane of the wing, a properly designed winglet can reduce the downwash at the wingtip and with it provide further lateral stability as well as a certain amount of additional lift [7, 13].

Balanced against the reduced induced drag is the additional profile drag of the winglet itself. Obviously, this leads to a fundamental trade-off in winglet design. However generally, induced drag is far more pronounced than profile drag and therefore winglets are usually optimised to minimise induced drag and consequently optimised to the wing itself.

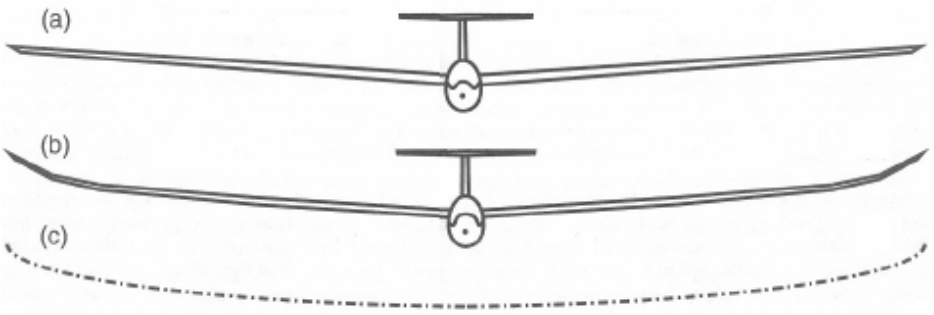

Fig. 5.12: Various lateral wing configurations [26].

a) Dihedral
b) Polyhedral
c) Semi-ellipse

In addition to winglets, several other approaches exist in minimising induced drag. As with winglets, *polyhedral,* a variation of the dihedral angle at several stations along the wingspan, provides a non-planar geometry offering the possibility of reducing induced drag (Fig. 5.12). Experimentation has shown that the optimum wing curvature is elliptical, however manufacturing such profiles has proven to be extremely difficult [26].

5.1.6 Fuselage and Fuselage/Wing Junction

Essentially the fuselage has two basic tasks:

- to carry the pilot, and
- to form a structural connection between the wing and empennage.

While in this case there is no pilot, sufficient space is still required to incorporate the controlling apparatus, ballasts and the inherent necessity to keep the prototype geometrically similar to its full size counterpart. To some extent, the cockpit and aft fuselage may be thought of as separate components. While the forward fuselage is sized to provide room for the pilot, the tail boom need only satisfy strength and stiffness requirements, without regard to its internal volume (except for the minimal space required by control cables). This obvious deduction naturally leads to the tapered fuselage typical of most modern sailplanes (Fig. 5.13).

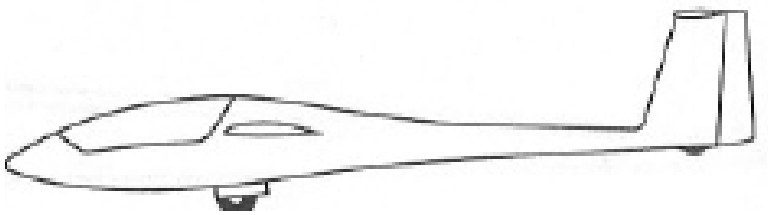

Fig. 5.13: Typical tapered fuselage [19].

Experimental values have shown that the fuselage typically accounts for around 10-15% of the sailplane's total drag. Therefore, it seems obvious that a clean aerodynamic form is essential to provide optimal performance. To achieve this, the fuselage is usually tapered aft of the boundary-layer transition line to minimise wetted area and additionally the skin friction incurred due to flow separation. Proper fuselage tapering however requires careful consideration with regard to the fuselage-wing interference effects [19].

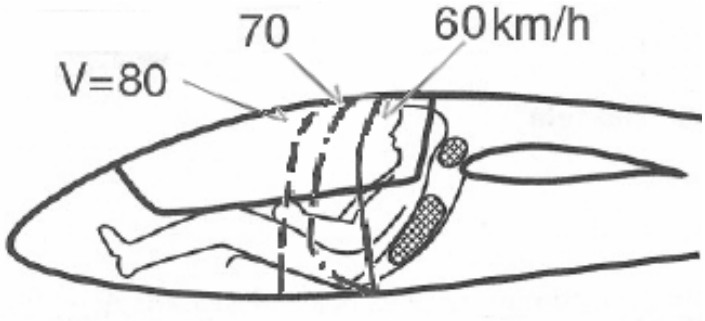

Fig. 5.14: Position of boundary layer transition at various speeds [26].

Put simply, the most important aspect of wing/fuselage design is the separation of the adverse pressure gradients associated with these regions. To achieve this, fuselage taper must occur either ahead of the point of maximum thickness of the wing root airfoil, or aft of the wing's trailing edge. If the fuselage taper occurs aft of the wing trailing edge, the wing should be set as high as possible on the fuselage and the taper limited to the fuselage lower surface (Fig. 5.15). Another method for reducing the adverse pressure gradient in the wing/fuselage junction involves fairing both the leading and trailing wing edges at the fuselage junction. Typically, a relatively narrow radius at the leading edge and a broader fairing at the trailing edge produce exceptional results.

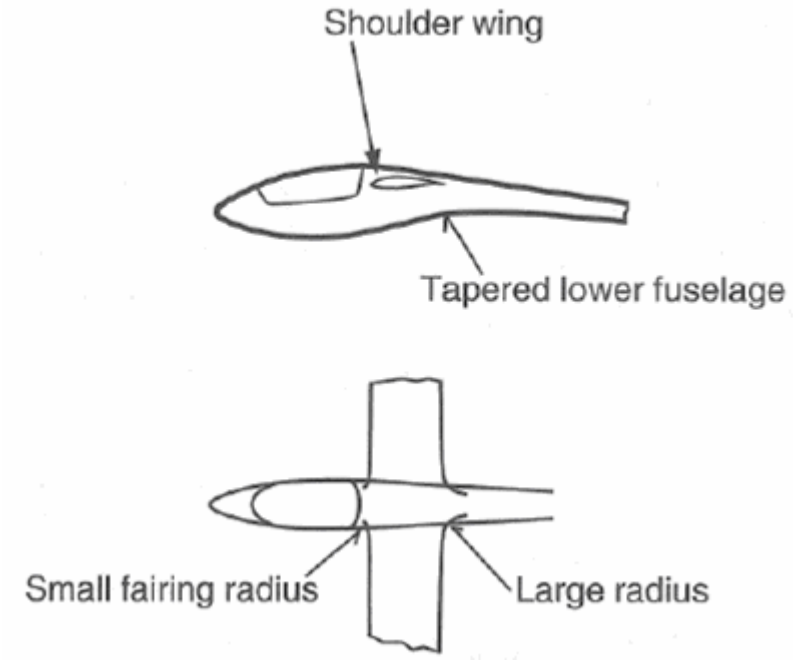

Fig. 5.15: Wing/fuselage junction for minimum interference drag [26].

Even with proper design, adverse pressure gradients are inevitable in the area of the wing-fuselage junction. However, a simple method of determining the wing/fuselage interference can be obtained by computational means. This method involves calculating the polars of the complete aircraft and subtracting the individual drag components of fuselage, wing, and empennage. The difference yields the interference drag (Fig. 5.16).

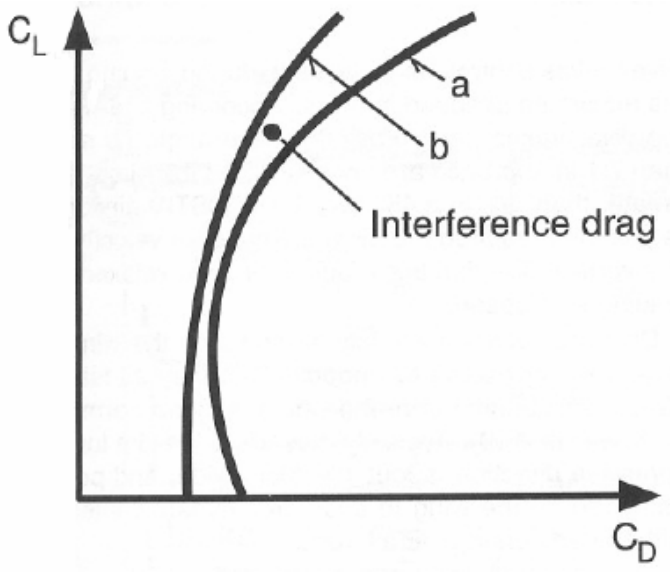

Fig. 5.16: Estimation of interference drag [26].

a	Polar measured in flight
b	Calculated polar
a-b	Estimated interference drag

In addition, because the fuselage aerodynamics is strongly influenced by the flow field induced by the wing, sailplane fuselages are usually built with a slight nose-down droop. This droop ensures that the fuselage centre line is inline with the surrounding flow and subsequently reduces the upwash and downwash affects on the forward and aft fuselage sections respectively. Analogous to wing loading, proper droop varies according to flight conditions, with more droop being required at low speeds. However, fuselages are generally optimised for high airspeeds as drag contribution is more significant in these flight regimes [26].

5.1.7 Ailerons

Although aileron optimisation and configuration is beyond the scope of this thesis, it is a topic of considerable importance to sailplane design and it therefore essential to include some basic information pertaining to their purpose.

Ailerons are typically located at the wing trailing edge and are sized to provide appropriate roll manoeuvrability in flight. Generally, they are located in this region as this is where the boundary layer is thickest. Since the dynamic pressure within the boundary layer is smaller than its free stream value, aileron effectiveness is improved by keeping the boundary layer as thin as possible. Very thick airfoils are thus unsuitable for use in

the aileron region. Laminar airfoils feature relatively thin boundary layers and this, combined with the trend towards thinner wings, has led to modern sailplanes with relatively small ailerons. While ailerons of 20-25% wing chord extending spanwise from $y/s = 0.6 - 0.95$ were typical of the first generation of laminar wing sailplanes (Fig. 5.17), modern practice favours longer ailerons of smaller chord (around 15%). For most purposes ailerons usually terminate inboard of the wingtip in order to prevent damage during landing.

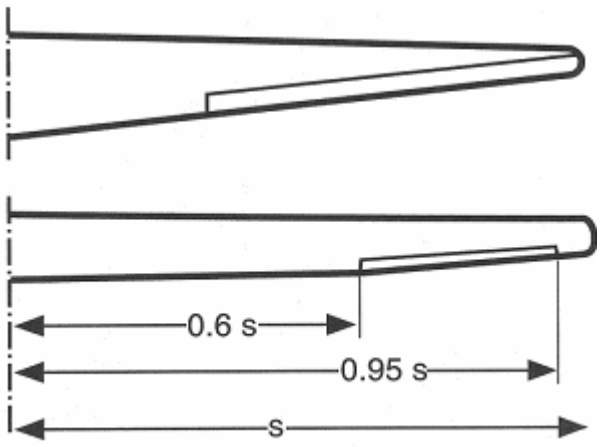

Fig. 5.17: Typical aileron configurations [22].

5.1.8 Tail Assembly

As discussed in previous chapters, the tail assembly consists of a horizontal and vertical stabilizer. As with the wing, the primary empennage planform parameters are aspect ratio and taper. It should be noted, that the optimum aspect ratio for each of the tail surfaces is a function of the profile drag of the selected airfoil, the induced drag, weight considerations, and effects on lift curve slope. Various studies have shown that horizontal stabilizer aspect ratios in the range of

$$4.5 \leq AR_H \leq 8 \qquad (28)$$

yield especially good results. Similarly, aspect ratios for vertical stabilizers lie mainly in the range of

$$1.5 \leq AR_V \leq 2 \qquad (29)$$

Previous studies show that induced drag of the individual tail surfaces is minimised with a taper ratio of approximately 0.4. However, this value should only be considered an absolute minimum. Increasing the taper ratio *(i.e.* reducing the taper) results in only a small drag penalty compared to the optimum. In addition, empennage chords are typically much smaller than those of the wing, consequently Reynolds number effects must be considered when optimising stabilizer planform parameters.

Fig. 5.18: Empennage arrangements: conventional, cruciform, T-tail and V-tail [26].

Some basic empennage arrangements are illustrated in Fig. 5.18. The conventional configuration, in which the horizontal and vertical tail surfaces are mounted separately on the fuselage, is seldom found in modern sailplanes due to the poor ground clearance provided by the relatively thin aft fuselages. The cruciform tail alleviates this difficulty somewhat but brings with it increased interference drag due to the four corners created by the intersection of the horizontal and vertical stabilizers.

One special form of empennage, the V-tail, differs from the other configurations by combining the longitudinal and lateral stability and control functions in a single set of control surfaces. Although several advantages exist, the overwhelming number of disadvantages including high induced drag renders the V-tail a reasonably inadequate empennage.
By comparison, the T-tail offers many advantages including:

- reduced interference drag,
- improved ground clearance,
- greater clearance from wing wake,
- good spin characteristics, and
- improved vertical stabilizer effectiveness due to end plate effect.

As a disadvantage, the T-tail places the horizontal stabilizer mass well away from the fuselage axis. Aeroelastic considerations necessitate increased fuselage and vertical stabilizer stiffness and with it an increase in structural weight. Overall, the many advantages of the T-tail have led to it becoming the standard for modern high performance sailplanes. Further information regarding horizontal and vertical stabilizer selection is outlined in the following sections [26].

5.1.9 Stability

The horizontal stabilizer has the task of maintaining the longitudinal stability and pitching moment equilibrium (longitudinal trim) in all steady and transient flight conditions. An aircraft is in moment equilibrium when the sum of all moments about any arbitrary reference point is zero (Fig. 5.19). Writing the aerodynamic forces and moments with respect to the center of gravity yields:

$$\sum M_{CG} = L_w \left(x_{CG} - x_{AC} \right) + M_{0w} - M_H = 0 \tag{30}$$

It should be noted, that if the horizontal stabilizer is cambered, the equation must be modified to reflect the zero lift moment, M_{0_H}, of the horizontal stabilizer. An exact calculation would also take into account a similar contribution from fuselage however, for simplicity both of these factors have been ignored.

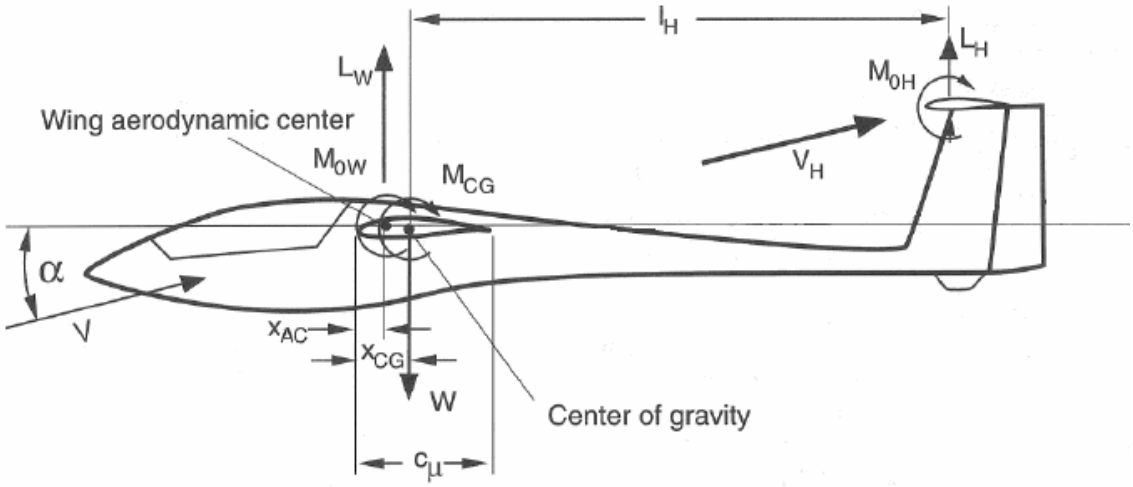

Fig. 5.19: Force and moment definitions for longitudinal stability [26].

The previous relationship can also be written in non-dimensional form by normalising to the dynamic pressure *q*, the wing area *S*, and the mean aerodynamic chord c_μ and simplifying by introducing several terms such as the lift curve slopes and volume coefficients for both the wing and horizontal stabilizer:

$$C_{L_H} \frac{dC_{L_w}/d\alpha_w}{dC_{L_H}/d\alpha_H} \frac{V_H}{V_W} = C_{L_w} \left(\frac{x_{CG}}{c_\mu} - 0.25 \right) + C_{M_{0w}} \tag{31}$$

As will be discussed, the lift curve slopes $dC_{L_w}/d\alpha_w$ and $dC_{L_H}/d\alpha_H$ are calculated based on the aspect ratios of the empennage and wing respectively.

5.1.9.1 Horizontal Stabilizer

Before determining any of the relevant parameters pertinent to the selection of the horizontal stabilizer its basic function should first be considered. Typically, sailplane airfoils are positively cambered to produce significantly more lift than their symmetric counterparts. Consequently, this cambering produces a negative zero-lift moment *(i.e.* nose-down) (Fig. 5.20, A). Using the center of gravity as a reference point for the forces and moments, and increasing the angle of attack results in increased lift and an accompanying positive (nose up) moment. Naturally, this condition is considered statically unstable.

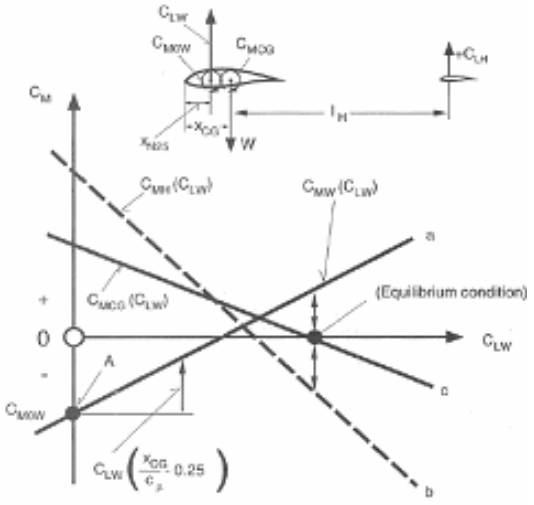

Fig. 5.20: Horizontal stabilizer contribution to stability [26].

(a) Isolated wing (unstable)
(b) Stabilizer contribution
(c) Complete aircraft (stable)

For static stability, the positive slope of the wing moment curve C_{M_w}, must be balanced by a correspondingly strong negative moment C_{M_H}. This corresponding negative moment is typically produced by the horizontal stabilizer. Whether this moment can be achieved however is dependent on a number of stabilizer parameters including the area, volume coefficient, angle of attack, lift curve slope and moment arm.

Apart from satisfying the static stability requirements, the empennage must also be able provide the moments necessary to trim the aircraft following a disturbance. Here, both the horizontal stabilizer volume and lift coefficients play a role, along with the sailplane angle of attack, induced downwash, stabilizer incidence, and elevator deflection.

In order to determine the appropriate parameters necessary for both static and dynamic stability a simplified method can be employed. First, the desired center of gravity range and minimum stability margin is established.

These parameters lead to the minimum stabilizer volume coefficient determined as follows:

$$\left(\frac{V_H}{V_W}\right)^{\star} = -\frac{x_{CG} - x_N}{c_\mu} + \frac{x_{CG}}{c_\mu} - 0.25 \tag{32}$$

Typically, this value should lie in the range of,

$$0.35 \le V_H / V_W \le 0.55 \tag{33}$$

Next, it must be verified that this stabilizer volume provides the required longitudinal control forces to trim the aircraft in all flight conditions. Here the critical cases are maximum wing lift (both positive and negative) with the center of gravity at its aft limit. Figure 5.21 presents an example of a wing with a cambered airfoil ($C_{M_{0_w}} = -0.1$), aft center of gravity location and a horizontal stabilizer volume $V_H / V_W = 0.3$. Using the following equations for the lift curve slopes of the wing and horizontal stabilizer respectively, the stabilizer lift coefficients can be calculated per Eq. 15.

$$\frac{dC_{L_w}}{d\alpha_w} = \frac{2\pi AR}{AR + 2} \tag{34}$$

$$\frac{dC_{L_H}}{d\alpha_H} = \frac{2\pi AR}{2 + \sqrt{AR^2 + 4}} \tag{35}$$

For this particular example, the trim condition at maximum or minimum lift requires a stabilizer C_{L_H} range of $-0.73 \le C_{L_H} \le +0.67$. If these coefficients cannot be achieved with the given stabilizer, the stabilizer volume must be increased and the other appropriate parameters changed accordingly.

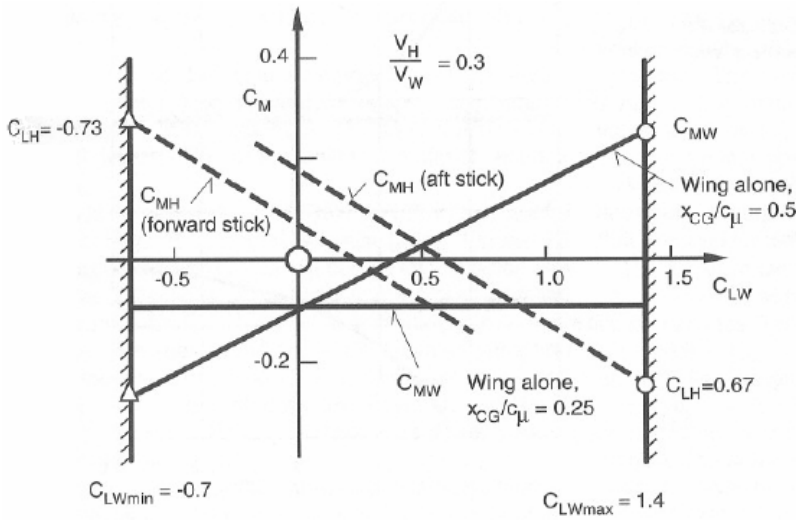

Fig. 5.21: Equilibrium conditions for maximum and minimum wing lift coefficients [26].

In addition to Eq. 16, the volume ratio can be calculated using the following equations

$$V_w = \frac{dC_{L_w}}{d\alpha_w} c_\mu S_w \tag{36}$$

$$V_H = \frac{dC_{L_H}}{d\alpha_H} \ell_H S_H \tag{37}$$

These equations are particular useful when locked into a certain design by particular constraints [26].

5.1.9.2 Vertical Stabilizer

The vertical stabilizer provides directional stability and contributes to the lateral stability of the aircraft. Analogous to the horizontal stabilizer, the vertical stabilizer can be optimised based on its effectiveness and drag penalties. Such optimisation first involves the calculation of certain variables. These values again include the lift curve slope and the stabilizer volume coefficient and can be calculated by:

$$\frac{dC_{L_V}}{d\beta} = \frac{2\pi AR_V}{2 + \sqrt{AR_V^2 + 4}} \tag{38}$$

$$V_V = \frac{dC_{L_V}}{d\beta_V} \ell_V S_V \tag{39}$$

Typically, the vertical stabilizer volume coefficient normalised against the wing area and span should lie in the range of,

$$0.045 \le V_V / S_w b_w \le 0.075 \tag{40}$$

Due to the endplate effect of the vertical stabilizer (especially in the case of T-tails), the vertical stabilizer has an effective aspect ratio somewhat larger than its geometric aspect ratio. This effect is shown for various empennage arrangements in Fig. 5.22 and can be calculated by:

$$AR_{eff} = \frac{AR_{geom}}{K} \tag{41}$$

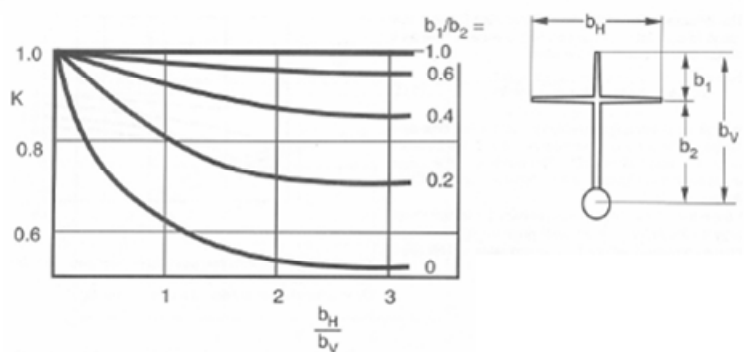

Fig. 5.22: Increase in effective aspect ratio due to end plate effect [26].

5.1.9.3 Tail moment arm

The horizontal stabilizing lift forces mentioned previously are directly proportional to the moment arm. The moment arm is optimised for drag minimisation on one hand and structural weight of the aft fuselage and empennage on the other. A longer empennage arm provides more aerodynamic damping in pitch and yaw, which, among other things, improves the stability of the spiral dive mode. On the other hand, longer moment arms require increased stiffness to ensure aeroelastic stability. Furthermore, short moment arms may not provide the require force necessary to ensure stability in all flight régimes. Although the optimal moment arms for vertical and horizontal stabilizer differ slightly moment arms in the range of

$$4 \leq \ell_H / c_\mu \leq 6 \qquad (42)$$

tend to yield particularly good results from both a weight and drag point of view.

5.2 Structural Design Requirements

As discussed earlier, the successful design of any aircraft involves a careful balance between conflicting design requirements. In addition to aerodynamic considerations, structural considerations must also be addressed. The most important of these considerations is undoubtedly the airfoil and wing integrity. As discussed in the previous chapter detrimental affects such as flight loads and aeroelasticity constantly bombard the wing structure. In response to these affects the previously mentioned parameters must be examined in order to ensure structural failure does not occur or is limited to specific areas.

5.2.1 Airfoil Selection

As mentioned earlier appropriate thickness is essential in airfoil selection. Generally, airfoils should be as thick as possible to provide high torsional stiffness in both the longitudinal and lateral directions of the wing or empennage. In addition, thicker airfoils also allow for easier manufacturability. As well as this, in the event that the wing or empennage comes into contact with a foreign object, larger geometries generally provide a greater cushioning effect. However, the obvious drawback from thicker airfoils is the accompanying weight gains associated with the additional material and structural stiffeners such as struts and ribs (Fig. 5.23). Consequently, optimising airfoils still remains a rather difficult task. Typically however, designers have tended to focus on thicker airfoils (12-18%) largely because of the additional space provided for ballasts as well as the advantageous aerodynamic properties these thicknesses provide.

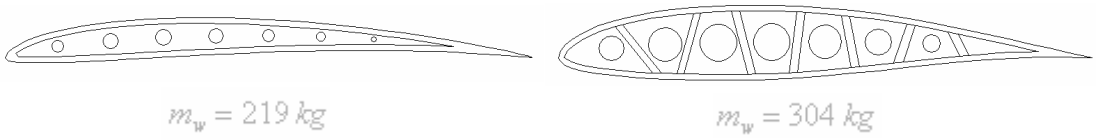

Fig. 5.23: Comparison between wing structural weight for thick and thin airfoils.

5.2.3 Aspect Ratio

As discussed, an aircraft with high aspect ratio wings has less induced drag and consequently greater efficiency. Aerodynamically this is beneficial, however as aspect ratio is increased more and more structural weight is required to support the wing. At some stage there comes a point where the disadvantage of increasing structural weight needed to support the increased wing span counteracts the advantage of decreased drag. Obviously then, an aircraft with a compromise on aspect ratio and which also considers factors such as control characteristics, size allowances, and numerous other factors, would provide optimal performance. Unfortunately, optimising the aspect ratio for both aerodynamic efficiency and structural weight presents a highly difficult problem to solve. For this reason, designers tend to place more emphasis on the aerodynamic aspect of the wing rather than that of the weight. However, it is obvious that wings with larger aspect ratios and low weight produce the most favourable results.

In addition to the stresses produced by the free weight of the wing there is also the often overlooked aerodynamic stress associated with the flight loads. While the structural weight and subsequently the structural stiffness can only be optimised to the aspect ratio, it is also necessary to ensure that the wing can withstand the varying aerodynamic loads and moments placed on it during flight. As mentioned, the wing can be considered for all intensive purposes a long, thin beam-like structure. Therefore, by employing elementary beam theory, stresses and deflections can be determined at the wing/fuselage junction and the appropriate measures taken to ensure failure does not occur. These properties can be estimated using the following equations:

$$\sigma = \frac{Mc}{I} + \frac{P}{A} \tag{43}$$

$$\delta = \frac{ML^2}{2EI} \tag{44}$$

where M is the moment created by the lifting force, c is the distance from the wings neutral axis, I is the wings moment of inertia, P is any force acting in the wing plane, A is the area that force P enacts on, L is the wing semi-span and E is the modulus of elasticity. Typically however, these properties are calculated with the use of computational methods which can also predict a number of other interesting outcomes associated with the wing dynamics.

5.2.4 Fuselage

While the fuselages' most basic task is to form a structural connection between the wing and empennage, it also functions as the main load bearing component of the aircraft. Consequently, while in operation the fuselage experiences a complex system of stresses. One particular case occurs during landing or more precisely during impact (Fig. 5.24). Because of the inherent geometry of the fuselage, impact stresses are typically passed through to regions of sharp sectional change. These regions, typically the wing/fuselage junction and the empennage, are more prone to failure than the initial impact zone, as the stress in these regions is significantly magnified. Obviously, a multitude of differing design requirements exists depending on the relevant test orientation. For this reason, impact test at varying orientations are an essential aspect to the design of any aircraft. These tests allow designers to limit the amount of damage incurred by either incorporating crumple zones or using stress concentration points to focus stress into easily repairable locations. Recently, computational methods have been developed to evaluate such instances.

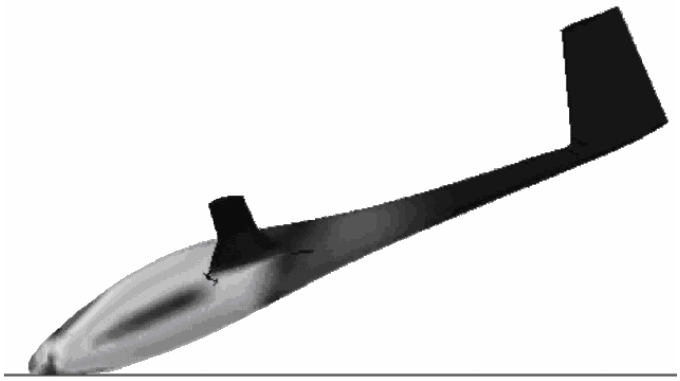

Fig. 5.24: Stress during impact.

5.2.5 Component Mass Location

Another important, yet often overlooked structural requirement is that of component mass location. Component mass location is the location of a components centre of mass relative to the mass majority neutral axes. Typical examples are that of the wings and empennage (Fig. 5.25).

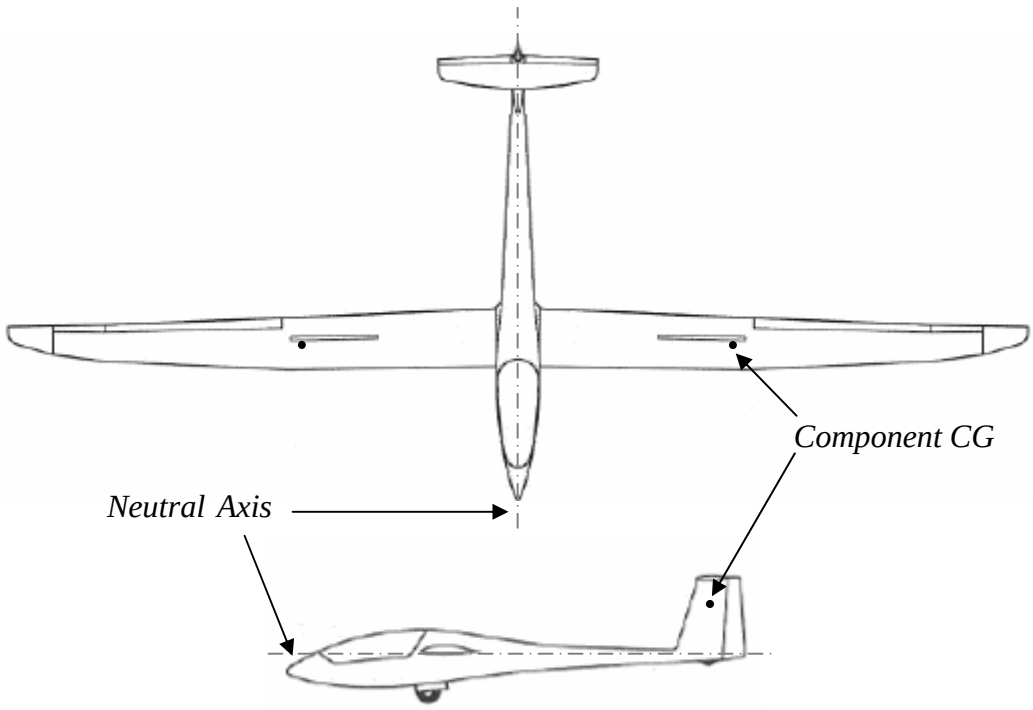

Fig. 5.25: Location of centre of mass for wing and empennage.

As discussed, while this presents only a small issue in level flight, problems may arise in turning manoeuvres but more likely and consequently more detrimentally in the instance of an impact. For this reason, aeroelastic considerations necessitate increased stiffness in and around these regions. While seemingly unavoidable, precautions should be taken to ensure that component mass is located as close as possible to the fuselage neutral axis I order to minimise unnecessary damage during an unstable landing or crash.

5.2.6 Materials Selection

As mentioned earlier, structural strength and weight are essential proponents to a successful sailplane design. Common to both these parameters is the material in which the aircraft is to be constructed. Fortunately, modern materials have largely eliminated many of the structural problems associated with the issues mentioned above. However, despite the availability of these modern materials, particular attention must still be paid to differing components of the aircraft. For this reason, different materials are often employed depending on the objective of these components. Typically, the fuselage is constructed from a relatively heavy, high endurance material, while the wings and empennage are usually constructed from a much lighter and more modular material.

In addition, several other aspects also play a role in material selection; manufacturability, affordability and maintainability. Such properties, usually rule out the use of labour-intensive construction methods and expensive materials such as titanium and exotic aluminium alloys. With the advent of carbon fibre however, these problems can often be alleviated. Furthermore, carbon fibre allows the development of more unusual wing and fuselage configurations not easily realised with other materials.

5.2.7 Aeroelastic

In addition to stress and impact considerations, modal considerations are also of particular importance. Although not nearly as obvious in general operation as load stresses, aeroelastic instabilities are extremely dangerous. In the event such instabilities occur, structural disintegration may result in a matter of seconds. Furthermore, the negative aerodynamic affects associated with wing flutter may render control surfaces ineffective. Methods of eliminating such aeroelastic behaviour include high material stiffness and limitation of the distance between mass centers as mentioned above. It is therefore necessary in the design of any aircraft, particularly in the case of a prototype (which would obviously need some method of propulsion) for a modal analysis to be conducted [20].

Chapter 6

Numerical Analysis

This chapter provides a brief introduction into the governing equations employed throughout the study, along with an overview of the accompanying software utilised throughout the design and analysis stages. In addition, this chapter discusses the numerical process through which the results were obtained.

6.1 Flow Equations

As mentioned in chapter 3, the equations governing the flow about an aircraft are extremely complicated. This section helps to define these equations and provides a basic explanation as to their purpose in this study.

6.1.1 Conservation of Mass

The conservation of mass or continuity equation is a fundamental equation of fluid mechanics and can be expressed in either integral or differential forms (Eq. 45-46). The continuity equation states that in order to conserve mass, the rate of change of the mass inside the control volume, plus the net rate of mass flow through the control surface must equal zero. It should be noted that the continuity equation in either its integral or differential form, is valid for steady and unsteady flow as well as compressible and incompressible fluids.

(Integral Form)

$$\left.\frac{dM}{dt}\right)_{system} = \frac{\partial}{\partial t}\int_{CV} \rho \, d\mathrm{V} + \int_{CS} \rho V \, d\mathrm{A} = 0 \qquad (45)$$

Rate of increase of mass in control volume + **Net rate of mass flux through the control surface** = **0**

(Differential Form)

$$\frac{\partial \rho}{\partial t} + \frac{\partial(\rho u)}{\partial x} + \frac{\partial(\rho v)}{\partial y} + \frac{\partial(\rho w)}{\partial z} = 0 \qquad (46)$$

Net rate of mass flux through the control surface + **Rate of increase of mass in control volume** = **0**

6.1.2 Conservation of Momentum

The conservation of momentum equation is a mathematical statement for the conservation of momentum within a fixed, non-deforming control volume. As in the case of the continuity equation, the momentum equation can be used in integral and differential forms (Eq. 47-48). Of particular importance to this study is the differential form of the momentum equation, commonly referred to as the Navier-Stokes equation. Within this particular form, equations for momentum in each direction are simplified for incompressible Newtonian fluid flow with constant viscosity. Due to these simplifications, the Navier-Stokes equation has previously been limited to simple geometries and boundary conditions. Recently however, the advent of faster computers and more complex computational fluid dynamics (CFD) software has enabled the analysis of more complex "real world" problems.

(Integral Form)

$$\vec{F} = \left.\frac{d\vec{P}}{dt}\right)_{system} = \vec{F}_S + \vec{F}_B = \frac{\partial}{\partial t}\int_{\mathrm{CV}} \mathrm{V}\rho \, d\forall + \int_{\mathrm{CS}} \mathrm{V}\rho V \, d\mathrm{A} = 0 \qquad (47)$$

Sum of the forces acting on the control volume = **Rate of change of the momentum inside the control volume** + **Net rate of flux momentum out through the control surface** = **0**

(Navier-Stokes Equation incompressible flow)

$$\rho\left(\frac{\partial u}{\partial t} + u\frac{\partial u}{\partial x} + v\frac{\partial u}{\partial y} + w\frac{\partial u}{\partial z}\right) = \rho g_x - \frac{\partial p}{\partial x} + \mu\left(\frac{\partial^2 u}{\partial x^2} + \frac{\partial^2 u}{\partial y^2} + \frac{\partial^2 u}{\partial z^2}\right)$$

$$\rho\left(\frac{\partial v}{\partial t} + u\frac{\partial v}{\partial x} + v\frac{\partial v}{\partial y} + w\frac{\partial v}{\partial z}\right) = \rho g_y - \frac{\partial p}{\partial y} + \mu\left(\frac{\partial^2 v}{\partial x^2} + \frac{\partial^2 v}{\partial y^2} + \frac{\partial^2 v}{\partial z^2}\right) \qquad (48)$$

$$\rho\left(\frac{\partial w}{\partial t} + u\frac{\partial w}{\partial x} + v\frac{\partial w}{\partial y} + w\frac{\partial w}{\partial z}\right) = \rho g_z - \frac{\partial p}{\partial z} + \mu\left(\frac{\partial^2 w}{\partial x^2} + \frac{\partial^2 w}{\partial y^2} + \frac{\partial^2 w}{\partial z^2}\right)$$

6.2 CFD Modelling

Computational fluid dynamics (CFD) is a powerful numerical simulation tool employed to provide greater insight into the flow behaviour of fluids that would otherwise be impossible to visualise using experimental techniques. Not only does CFD predict fluid flow behaviour, but it is also capable of analysing heat transfer, mass transfer, phase change, chemical reactions, mechanical movement and the stress and deformation of solid structures interacting with fluids.

There are three main benefits associated with CFD software: insight, foresight and efficiency. Through the use of CFD software insight is gained into devices and systems that would otherwise be difficult to prototype or test through experimentation. This insight enables the user to obtain an enhanced understanding of the design as well as means of visualising otherwise impossible phenomena. CFD software provides the benefit of foresight by allowing the user to test a number of variations in order to answer those “what if” scenarios. Through this process, the optimal solution can be obtained. Finally, the efficiency of CFD software allows better and faster designs to be produced. This saves both time and money, and ultimately allows products to go to market much faster.

In its application, CFD software operates by converting the differential form of the governing equations mentioned earlier into a set of algebraic equations. These equations can then be solved for flow field values at discrete points. These discrete points are created via a process referred to as discretisation. In this process the fluid domain is represented by a geometrically similar model consisting of multiple, linked, simplified elements contained within the domain boundaries. These boundaries can be defined as either inlets, outlets, walls and/or a number of other conditions. The model is then solved using an iterative process until convergence is reached, a point where the solution is no longer changing with successive iterations.

6.3 CFD Software Selection

Due to the complexities associated with aircraft design, several forms of software were employed throughout the design process. This software had to be capable of modelling a range of flow conditions and in addition provide detailed and complete information pertaining to the velocity and pressure distribution throughout the domain of interest. Furthermore, the software needed to be capable of modelling large amounts of turbulent flow, as this was anticipated at several specific locations over both the wing and aircraft structure.

As the information pertaining to the two dimensional airfoil analysis was of upmost importance to this study, a specialised airfoil flow program known as XFOIL was adopted. Through the use of this specialised program, accuracy of information was ensured. As for the three dimensional analysis, Fluent was chosen based on its widely accepted status within the aerospace field and for its availability within the University.

6.4 XFOIL Overview

XFOIL® is a specialised fluid flow program for the design and analysis of subsonic isolated airfoils. It consists of a collection of menu-driven routines which perform various useful functions pertinent to this study. These functions include:

- Viscous or Inviscid analysis of isolated airfoils allowing,
  - forced or free transition
  - transitional separation bubble(s)
  - limited trailing edge separation
  - lift and drag predictions just beyond $C_{L_{MAX}}$

- Lift and drag polar calculations with fixed or varying Reynolds and/or Mach numbers.

- Writing and reading of airfoil geometry files

- Plotting of geometry, pressure distributions, and Lift/Drag polars

Additional XFOIL features include:

- Airfoil design and redesign by interactive specification of a surface speed distribution

- Airfoil redesign by interactive specification of new geometric parameters such as
  - max thickness and/or camber
  - LE radius
  - TE thickness
  - camber line via geometry specification
  - camber line via loading change specification
  - flap deflection

- Blending of airfoils

6.5 Fluent Overview

Fluent® is one of the world's most widely used commercial CFD codes for modelling fluid flow and heat transfer in complex geometries. Fluent software actually encompasses two separate programs; the Fluent solver program and Gambit, a pre-processor for geometry and mesh generation.

The Fluent solver itself has extensive interactivity and provides number comprehensive modelling capabilities that include:

- 2-D and 3-D geometries,
- flow through porous mediums,
- transient or steady-state analysis,
- convection, conduction and radiation,
- sliding meshes,
- chemical species mixing and reactions,
- turbulent and laminar models and,
- incompressible and compressible flow.

Fluent's program structure is best summarised in the following schematic representation.

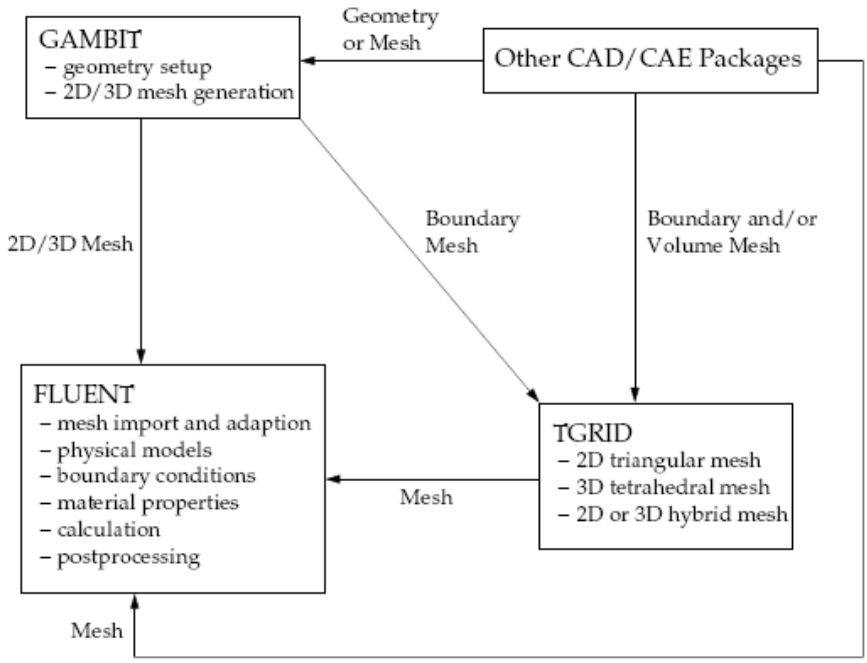

Fig. 6.1: Fluent program structure [35].

6.6 CFD Analysis

The successful completion of any CFD investigation includes a number of essential steps. These steps are imperative to develop a logical sequence through which an accurate solution can be obtained. These steps include:

- Software testing
- Definition of model goals
- Creation of model geometry and grid
- Preparation of solver and physical model
- Problem solution
- Examination of results

6.6.1 Software Testing

Before the implementation of any CFD software, it is first necessary to determine the accuracy of the programs under review. To accomplish this, several airfoil geometries which had easily accessible experimental data were tested using the CFD programs and the results compared. Fortunately, both CFD programs proved to be extremely accurate, providing results comparable to the experimental data. With the accuracy of the CFD software now confirmed analysis could begin.

6.6.2 Modelling Goals

As noted earlier, this study aims to optimise a prototype sailplane with regard to its aerodynamic efficiency. The investigation considers the influence of a number of factors, including the airfoil, wing planform, fuselage and tail assembly geometries, and the inherent interference between these components. These parameters have each been identified as important features with regard to the efficiency of current sailplane models. The overall aim of this study is to determine the appropriate combination of the previously mentioned components to provide the greatest lift and lowest drag over a range of flight speeds.

6.6.3 Modelling Assumptions

To accurately model the sailplane geometry within the set time requirements, certain aspects of the CFD model had to be simplified with regards to both the physical and simulatory aspects.

Certain assumptions were made for the physical structure of sailplane in order to reduce both the design time and solution time of the investigation. These assumptions included the selection of a generic fuselage and tail assembly; details of which can be found in Appendix C. This assumption was based on research illustrating that the majority of these components were geometrically similar in most sailplanes. In addition, an appropriate prototype scale was chosen based on the ease of manufacturability and the similitude to RC models that already exist. Details concerning the prototype scale are illustrated in Table 6.1.

Table 6.1: 1:6 Prototype Sailplane Details

Body & Wing							Horizontal Stabilizer				Vertical Stabilizer			
fuselage length	wingspan, b	aspect ratio, AR	wing area, S	wing loading	root chord	taper ratio	span	area	aspect ratio	mean chord	height	area	aspect ratio	mean chord
(m)	(m)	(-)	(m^2)	(daN/m^2)	(m)	(-)	(m)	(m^2)	(-)	(m)	(m)	(m^2)	(-)	(m)
1.13	2.5/3	22.1	0.28	5.38	0.14	0.35	0.375	0.029	5.51	0.08	0.20	0.29	1.36	0.170

Flow velocities of 1 m/s, 5 m/s, 10 m/s, 15 m/s and 20m/s were chosen for this investigation. It was expected that the data received from this range would suffice for the optimisation process, based on a review of similar models. This flow was assumed parallel and un-turbulated prior to the interaction with the relevant sailplane components. It should also be noted that all components were tested assuming un-accelerated level flight (Fig. 6.2). The horizontal stabilizer was tested at a range of differing angles of attack from -6 to +6 degrees to ensure an accurate stability analysis could be carried out (See Results).

In the development of the CFD model, further assumptions were made in order to improve the accuracy of the solutions as well as to reduce the solution time of the investigation. These assumptions included:

- 2D and 3D analyses
- No seams, joints, rivets or other fixing were modelled, and

Fig. 6.2 Component analysis orientation .

6.6.4 Model and Mesh Generation

6.6.4.1 Two-Dimensional

As previously mentioned, airfoil selection is the single most important aspect of sailplane design. Therefore, considerable effort has been made to ensure that the results obtained from the two dimensional analysis are highly accurate. To ensure this accuracy the two dimensional analysis was undertaken with the use of a specialised airfoil analysis program called XFOIL.

In order for XFOIL to calculate the appropriate lift and drag polars, the airfoil geometry and Reynolds numbers needed to be specified. Fortunately, an online airfoil coordinate database exists that contains over 1200 low Reynolds number airfoils. Of these, 70 positively cambered airfoils typically employed in models of similar size were selected as possible candidates for the wing geometry. In addition, 10 symmetric airfoils were selected for the horizontal and vertical stabilizers, respectively (See Appendix C).

To ensure no adverse effects occurred at either the wing root or tip, Reynolds numbers were calculated for both of these locations. This enabled the results to be averaged over the entire wing surface. Reynolds numbers for the various aircraft components are illustrated in the following tables.

Table 6.2: Reynolds Numbers for Wing Airfoils

	1 m/s	5 m/s	10 m/s	15 m/s	20 m/s
Wing Root (0.143 m)	10 000	48 000	96 000	144 000	192 000
Wing Tip (0.050 m)	3 000	17 000	34 000	51 000	68 000

Table 6.3: Reynolds Numbers for Horizontal Stabilizer Airfoils

	1 m/s	5 m/s	10 m/s	15 m/s	20 m/s
H. Stabilizer Root (0.085 m)	6 000	28 000	57 000	85 000	113 000
H. Stabilizer Tip (0.045m)	3 000	16 000	31 000	47 000	62 000

Table 6.4: Reynolds Numbers for Vertical Stabilizer Airfoils

	1 m/s	5 m/s	10 m/s	15 m/s	20 m/s
V. Stabilizer Root (0.170 m)	11 000	57 000	113 000	170 000	226 000
V. Stabilizer Tip (0.100 m)	7 000	36 000	71 000	107 000	143 000

With these variables specified, the appropriate lift and drag polars could be generated. The results from this analysis were then used to determine the most optimal airfoil geometry (see Results).

6.6.4.2 Three-Dimensional

The airfoil determined from the two dimensional analysis was then used to simulate and evaluate the three dimensional effects of differing wing geometries. The wing configurations were the product of the previous chapter's research and consisted of a rectangular wing, tapered wing, tapered wing with winglet, a double tapered wing, a double tapered wing with winglet, a triple tapered wing with winglet and a triple tapered wing with a high performance winglet (See Appendix C). The three dimensional models were generated using SolidWorks® and incorporated all of the pertinent features of the optimal airfoil. The fuselage, tail assembly and optimised sailplane geometries were also modelled in this way. The models were then exported to Gambit for pre-processing.

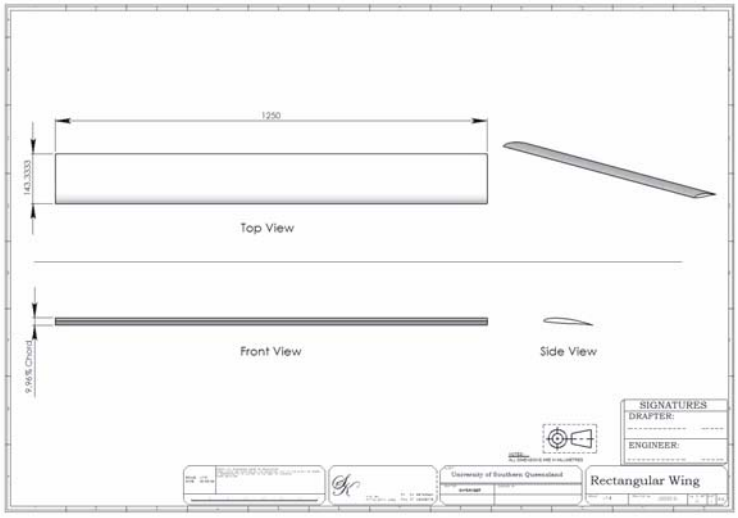

Fig. 6.3: 3d parametric model of rectangular wing.

The next step was to create and mesh the computational domain. For consistency all nine models were meshed using an identical process. To create the computational domain, the specific geometries (i.e. wings, fuselage etc) were subtracted from a large rectangular block (Fig. 6.4).

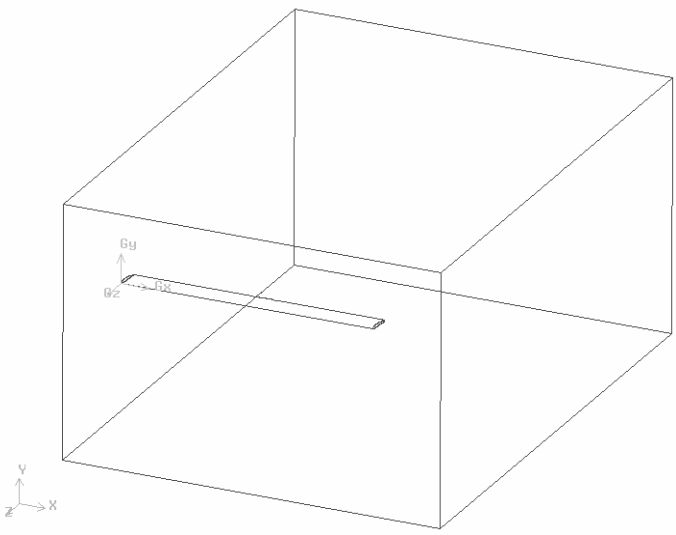

Fig. 6.4: Computational domain.

Next, a sizing function was employed to control the domain mesh. This enabled the mesh density to be controlled at various locations, specifically in regions where the flow needs to be analysed in some detail (i.e. close to wing).

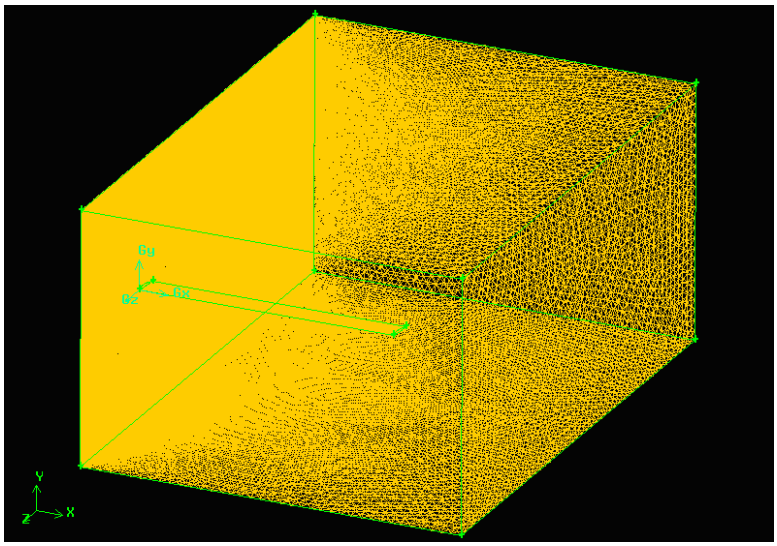

Fig. 6.5: Mesh of computational domain.

Using the TGRID meshing application a 3d tetrahedral mesh was then applied to the computational domain (Fig. 6.5). In addition, boundary zones were specified for the wing, inlet, outlet and walls as shown in Fig. 6.6.

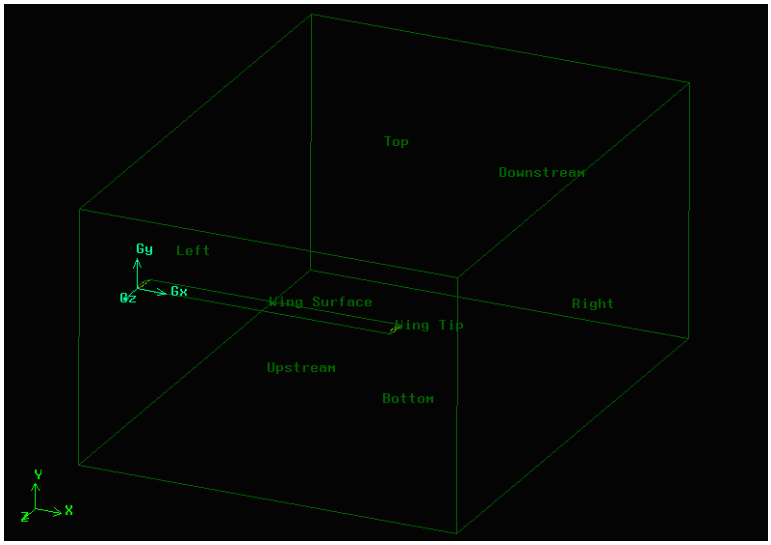

Fig. 6.6: Boundary zones.

Finally, the mesh quality was assessed (Fig. 6.7). The mesh quality is important because the size and shape of elements influence the accuracy of the final solution. The models were then exported to Fluent for the final set-up and solution.

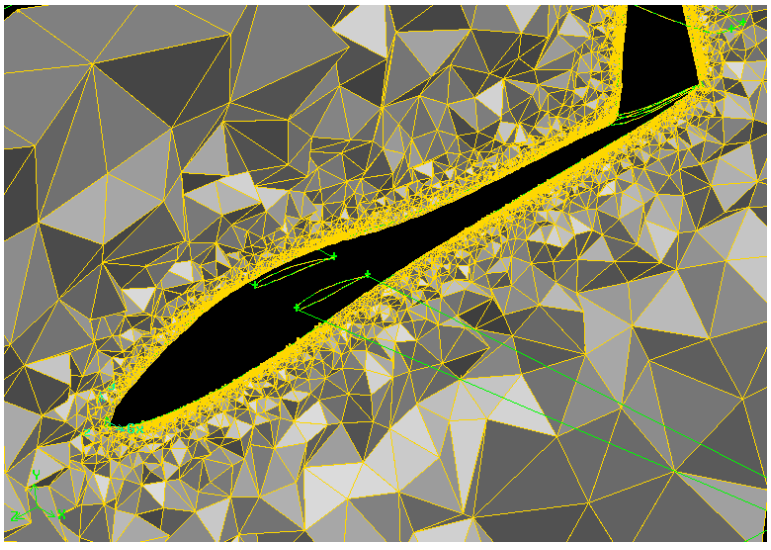

Fig. 6.7: Mesh quality surrounding optimised sailplane.

6.6.5 Fluent Solver

Once the Gambit model was imported into the Fluent solver program, the model was checked for any inconsistencies in the defined boundaries and elements of the meshed domain. Certain model parameters, including the solver type, time state, model type, and the boundary, operating and initial conditions, were then defined. These parameters are presented in the following tables.

Table 6.5: Model Parameters

Solver	Segregated
Formulation	Implicit
Time state	Steady
Model Type	Viscous k-ε
Solution Space	3D

Table 6.6: Model Boundary Conditions

Boundary Name	Boundary Type	Hydraulic Diameter (m)	Turbulence Intensity Factor	Velocity (m/s)
Upstream	Velocity Inlet	-	2	10,15,20
Downstream	Pressure Outlet	-	2	-
Left	Wall (Zero Shear)	-	2	-
Right	Wall (Zero Shear)	-	2	-
Top	Wall (Zero Shear)	-	2	-
Bottom	Wall (Zero Shear)	-	2	-
Wing Surface	Wall (No slip)	0.140	-	-
Fuselage Surface	Wall (No slip)	0.140	-	-
Tail Surface	Wall (No slip)	0.140	-	-
Sailplane Surface	Wall (No slip)	0.140	-	-

Once the aforementioned parameters had been defined, an iterative process was initiated and monitored until convergence occurred. Using this process, the most optimal wing planform was determined, as well as the necessary aerodynamic data for both the fuselage and tail assembly. The results are presented in the following chapter.

6.7 Structural Modelling

In addition to the aerodynamic analysis, a structural analysis was also deemed necessary to assess the structural integrity of the model. Based on the information detailed in the previous chapter, stress, modal and impact analyses were conducted to ensure the prototype could withstand the varying conditions incurred during normal and adverse operation. These investigations were conducted with the use of computational software, outlined below.

6.8 COSMOSWorks Overview

COSMOSWorks® is a design analysis automation application fully integrated into the SolidWorks® application. This software uses the Finite Element Method (FEM) to simulate the working conditions of designs and predict their behaviour. COSMOSWorks has the ability to perform several analysis types, allowing the investigation of a number of different situations. The analysis types include:

- Linear stress
- Frequency
- Buckling
- Thermal
- Impact

These dynamic features allow the user to quickly check the integrity of designs and ultimately find the optimal design solution. These benefits, coupled with the relative ease of use compared to other FEM packages, made COSMOSWorks the best choice for this section of the design process.

6.9 Static Analysis

Once the aerodynamic analysis had been completed and the geometry optimised, it was then necessary to conduct a static analysis to determine if the sailplane geometry could withstand the respective flight loads. Fortunately, the three dimensional models constructed in SolidWorks could easily be tested with the use of the integrated COSMOSWorks application (Fig. 6.8).

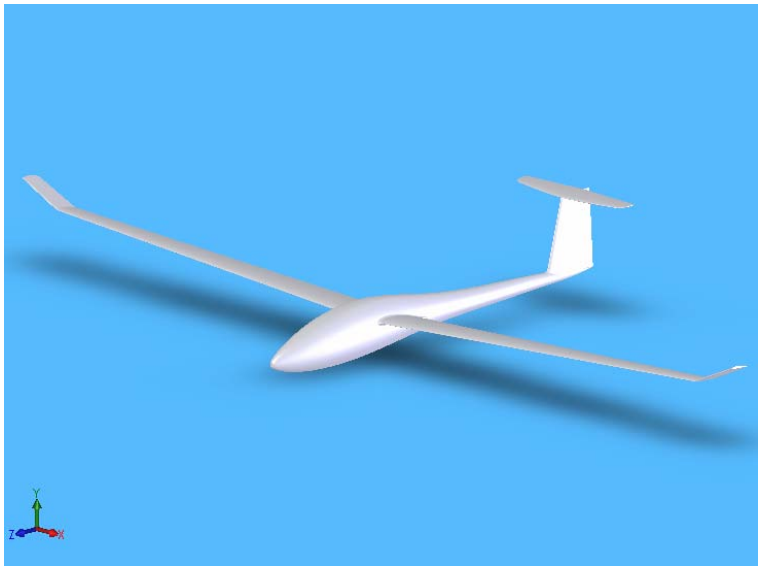

Fig. 6.8: Optimised sailplane geometry.

However, before any analysis could begin certain parameters requiring defining. These parameters included the mesh density, material type, and load and restraint strengths and locations. Due to the tight geometric fairing in the wing/fuselage and fuselage/tail junctions, the mesh size had to be relatively small to ensure the success of the meshing process and the overall accuracy of the solution (Fig. 6.9).

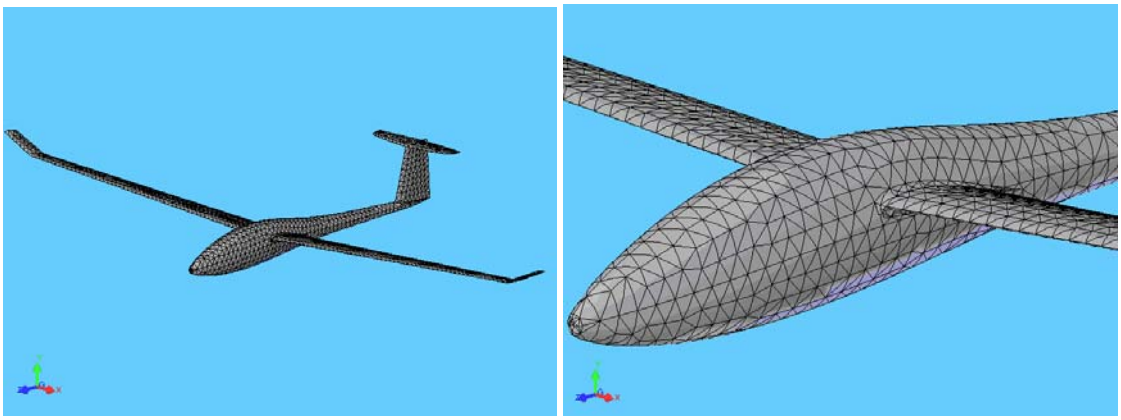

Fig. 6.9: Mesh of optimised sailplane.

With regard to the material type, it was decided that the fuselage and tail assembly would be constructed from fibreglass and the wing structure from high impact foam. The selection of these materials was based on their high strength to weight ratios as well as their ease of manufacturability. It should be noted that in order to accurately replicate the true prototype design, the fuselage was considered as a hollow body whereas the wings were considered to be solid structures.

Finally, the load conditions were determined with the use of the aerodynamic data obtained from the previous investigation. The analysis considered loads as a consequence of the aircraft moving at a constant flight speed of 20 m/s. These loads were applied at the aerodynamic centres of the wing and horizontal stabilizer. These conditions are illustrated in Fig. 6.10.

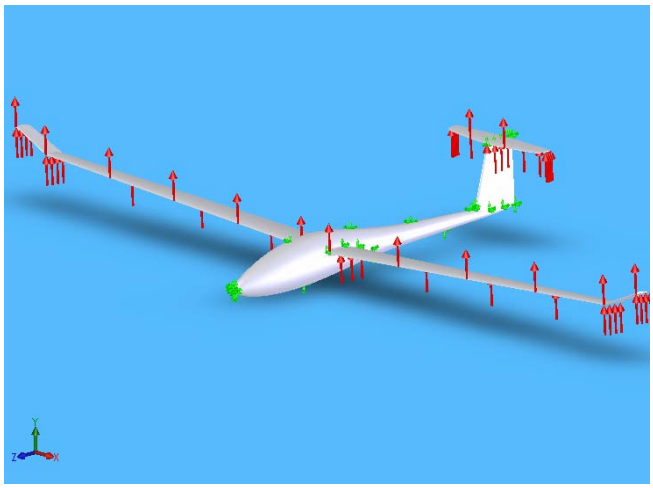

Fig. 6.10: Load and restraint conditions for static analysis.

With these parameters defined the static analysis was conducted and the results recorded in the following chapter.

6.10 Modal Analysis

A modal analysis was conducted to ensure that the prototype geometry could withstand any aeroelastic behaviour that may occur during operation. This analysis was conducted using the same parameters defined in the static analysis and the results are recorded in the following chapter.

6.11 Impact Analysis

An impact analysis was conducted to determine whether the prototype could withstand the stresses associated with a ground impact. Again, an identical set up procedure was conducted with this analysis however two additional parameters were required. These parameters were the impact velocity and the angle of impact. An impact velocity of 15 m/s was chosen because the results from the aerodynamic analysis indicate this velocity to be the stall velocity of the aircraft. Of the multitude of possible impact orientations, an angle of impact of 45 degrees was chosen for interest's sake (Fig. 6.11). The results from this analysis are discussed in the following chapter.

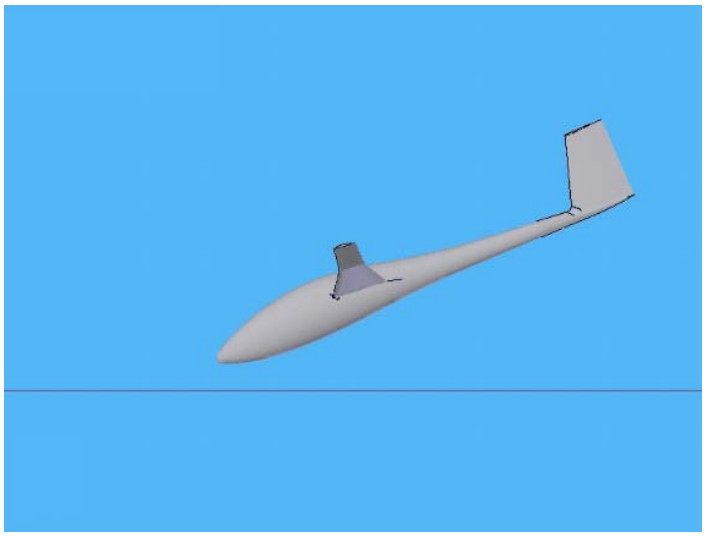

Fig. 6.11: Impact orientation.

Chapter 7

Results and Discussion

This chapter outlines and discusses the results obtained from the CFD and structural analysis.

7.1 Results Outline

The results from the numerical analysis have been grouped into three sections:

- *Two-Dimensional* which examines the results of the airfoil geometries for the wing, horizontal stabilizer and vertical stabilizer;
- *Three-Dimensional* which examines the results from the various wing planforms, fuselage, tail assembly and complete prototype geometries and in addition covers the stability analysis; and
- *Structural* which includes the static, modal and impact analyses.

7.2 Two-Dimensional

7.2.1 Wing Airfoils

The results from the two dimensional analysis indicate that over the various flow velocities tested, thinner airfoils produced significantly greater L/D ratios than their thicker counterparts. These higher L/D ratios can be attributed to the additional friction drag incurred by the thicker profiles. In addition, as mentioned in earlier chapters, thicker airfoils are typically more prone to greater amounts of flow separation. This theory is reinforced by the results, which indicate that thicker airfoils generally exhibited lower stall angles of attack, illustrating their greater susceptibility to flow separation. This phenomenon can be substantiated by the following figure.

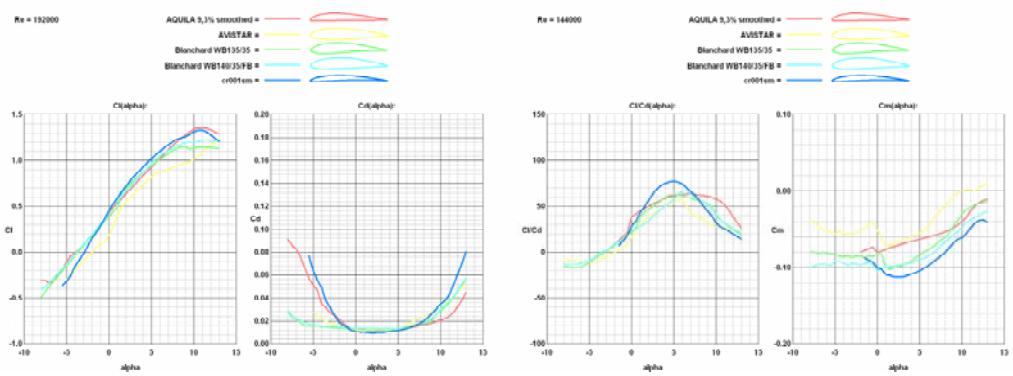

Fig. 7.1:Thick and Thin Airfoil Comparison.

It can be seen in Fig. 7.1 that the thinner airfoils, marked in blue and pink, not only have greater L/D ratios but also stall at a much higher angle of attack. Based on this data, it was concluded that thinner airfoils yielded the greatest performance over the range of airfoils tested. This decision was based on the L/D ratios, the angle of attack and the size of pre-stall region.

Through a systematic elimination process, the 70 possible wing airfoil geometries were reduced to just 3 using the method described in chapter 5 (Fig. 7.2). These were the CR 001sm, HQ 358, and HQ 3510 (See Appendix D). While the CR 100sm and HQ 358 airfoils produced marginally better L/D ratios than that of the HQ 3510, they were also extremely thin (7-8% of the chord).

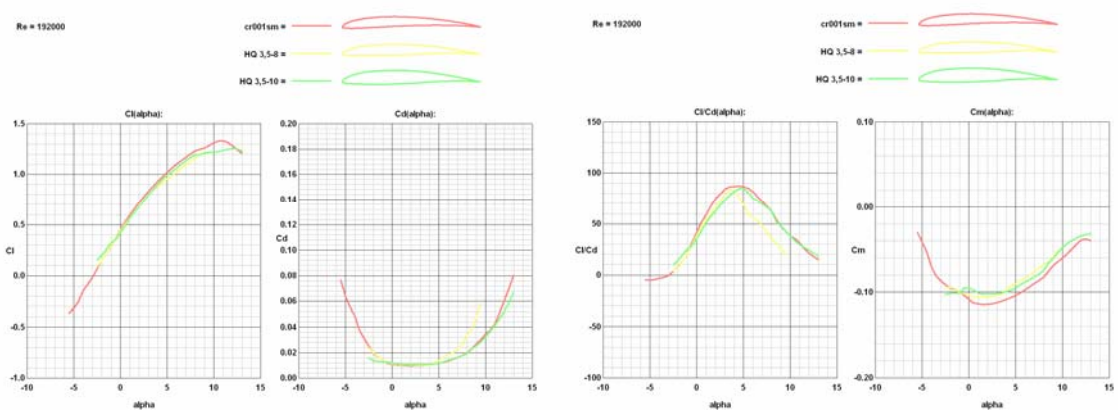

Fig. 7.2: CR 100sm, HQ 358 and HQ 3510 Comparison at 20 m/s.

Because there was only a marginal difference in the aerodynamic properties of the final three, it was decided that the HQ 3510 was the most optimal choice based on the manufacturability of the wing geometry. This airfoil produced a maximum lift to drag ratio well above that considered acceptable over the majority of flight speeds. In addition, the optimal angle of attack was found to be 5.0 degrees, which is within the typical range. The lift and drag polars for both the wing root and wing tip of the HQ 3510 at 20m/s are illustrated in the following figures. For extensive results, refer to Appendix D.

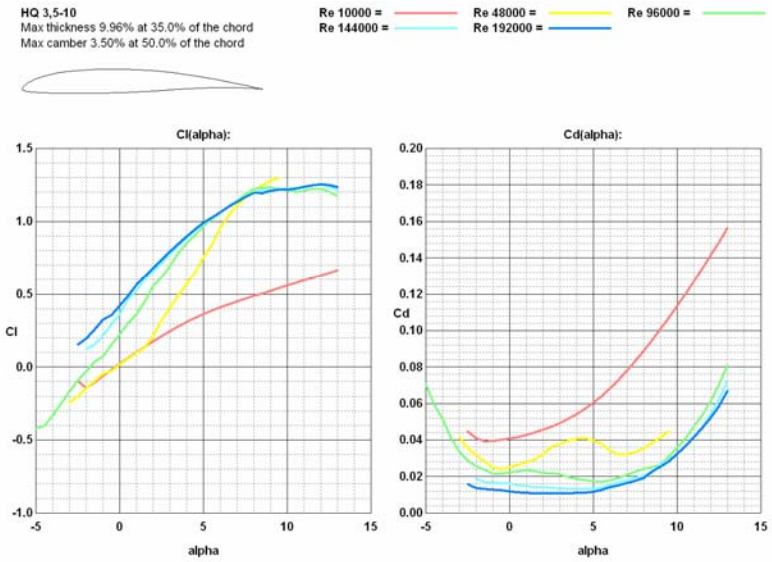

Fig. 7.3: HQ 3510 Wing Root - C_L vs. AOA and C_D vs. AOA .

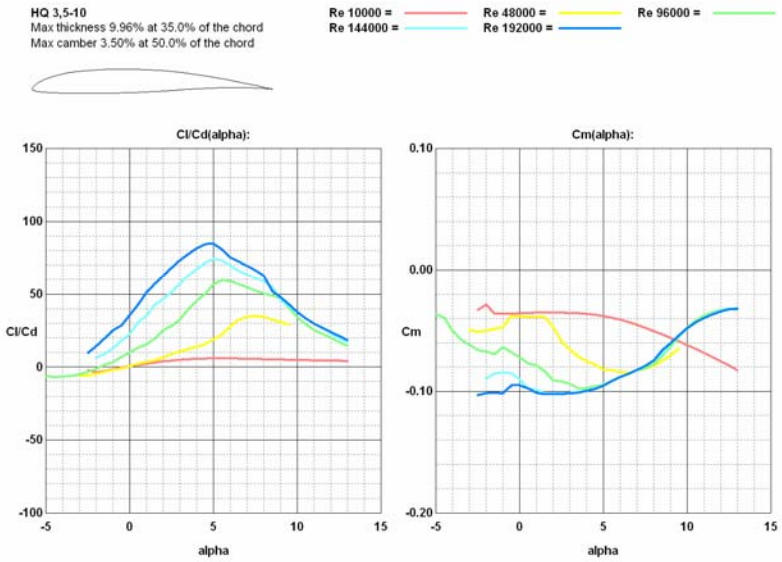

Fig. 7.4: HQ 3510 Wing Root - C_L/C_D vs. AOA and C_M vs. AOA .

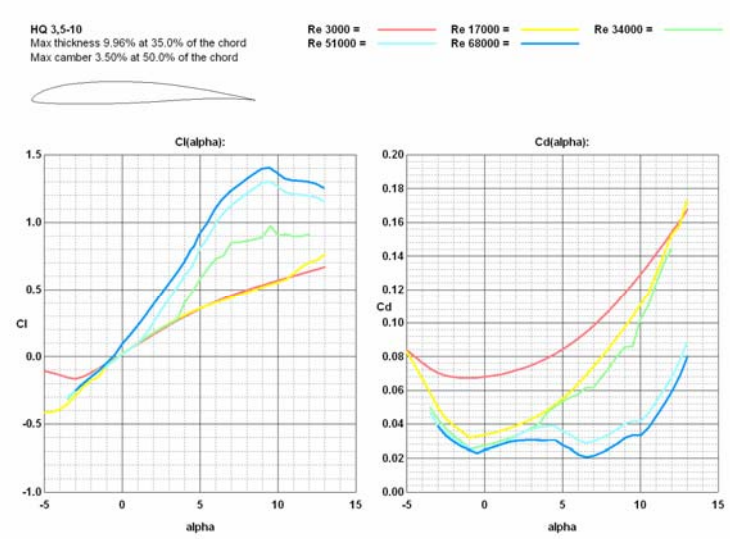

Fig. 7.5: HQ 3510 Wing Tip - C_L vs. AOA and C_D vs. AOA .

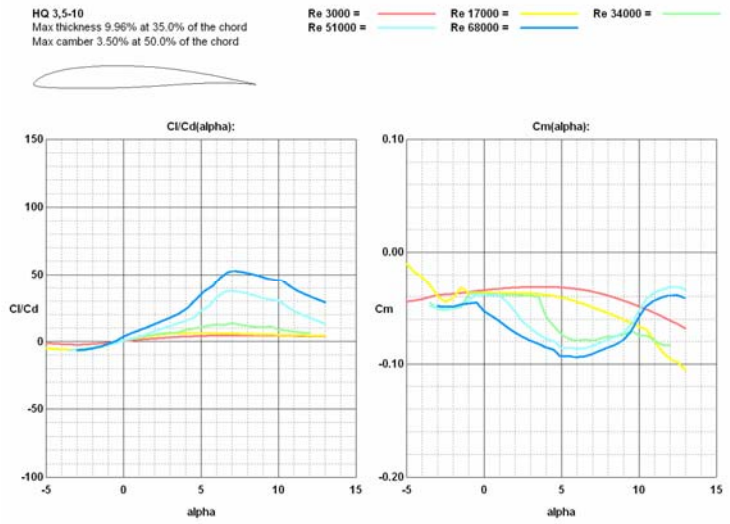

Fig. 7.6: HQ 3510 Wing Tip - C_L/C_D vs. AOA and C_M vs. AOA .

Using this airfoil the minimum flight velocity was calculated based on a rectangular planform with a wingspan of 2.5 m and a total aircraft weight of 1.85 kg. This velocity found to be approximately 10 m/s (See Appendix B). Due to this low flight velocity there was no need to conduct the three-dimensional analyses at 1 m/s and 5 m/s.

7.2.2 Horizontal Stabilizer Airfoils

The C_L range is of particular importance to the airfoil selection for horizontal stabilizers. Therefore, the pre-stall region and range were scrutinised quite significantly. Great emphasis was placed on the $C_L vs. \alpha$ gradient and profile drag during optimisation process. In order for the horizontal stabilizer to function effectively (i.e. stabilize the aircraft) the chosen airfoil needed to produce both high amounts of lift at low angles of attack, as well as high amounts of lift for small changes in the angle of attack. Analogous to the wing, the horizontal stabilizer also needs to have minimal drag on the overall aircraft structure. The airfoil that best displayed these properties was the NACA 0009. Details of this airfoil are shown in the following figures. For extensive results, refer to Appendix D.

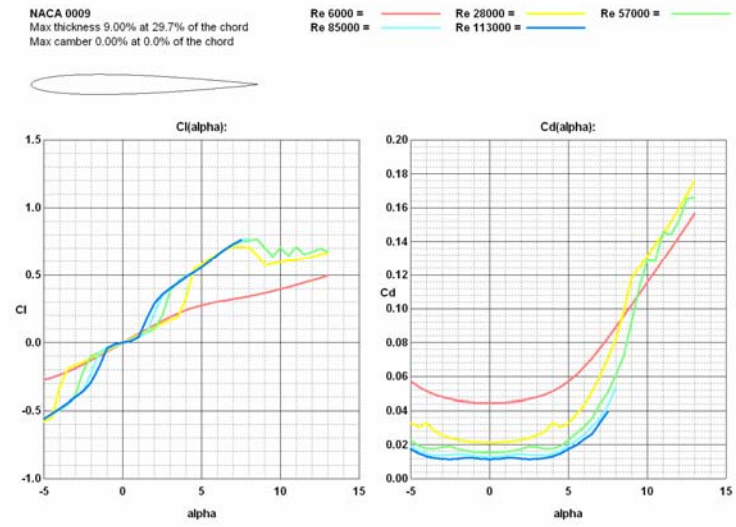

Fig. 7.7: NACA 0009 Stabilizer Root - C_L vs. AOA and C_D vs. AOA .

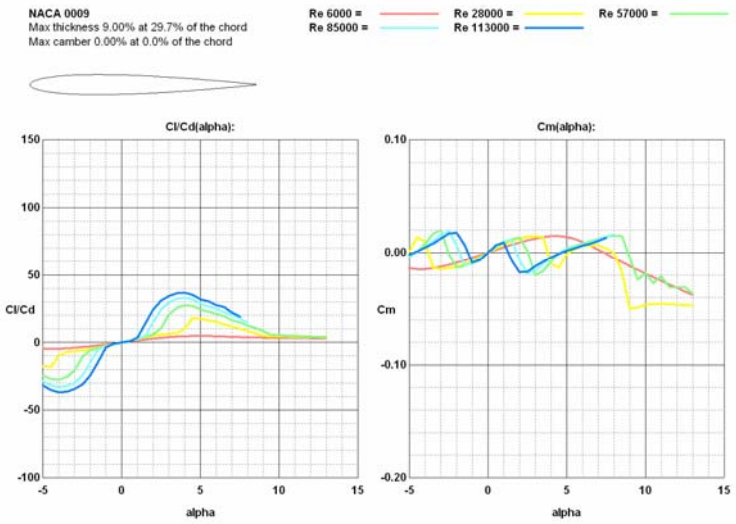

Fig. 7.8: NACA 0009 Stabilizer Root - C_L/C_D vs. AOA and C_M vs. AOA .

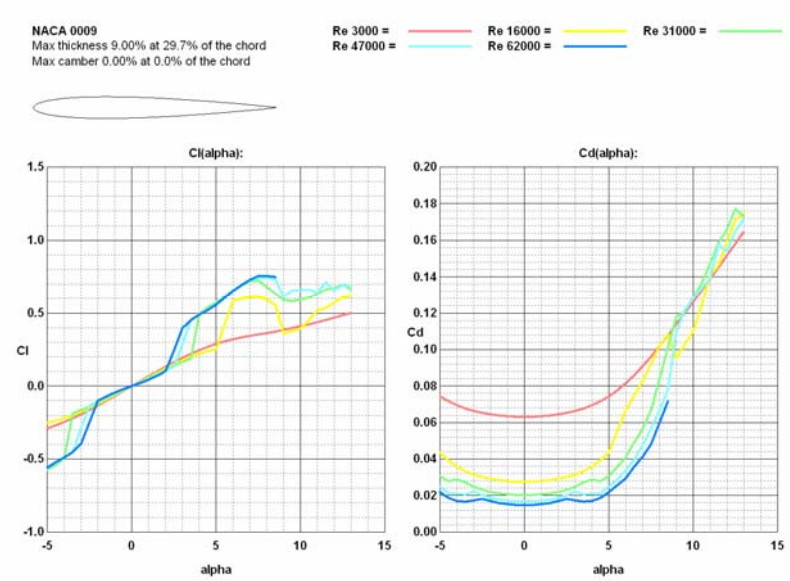

Fig. 7.9: NACA 0009 Stabilizer Tip - C_L vs. AOA and C_D vs. AOA .

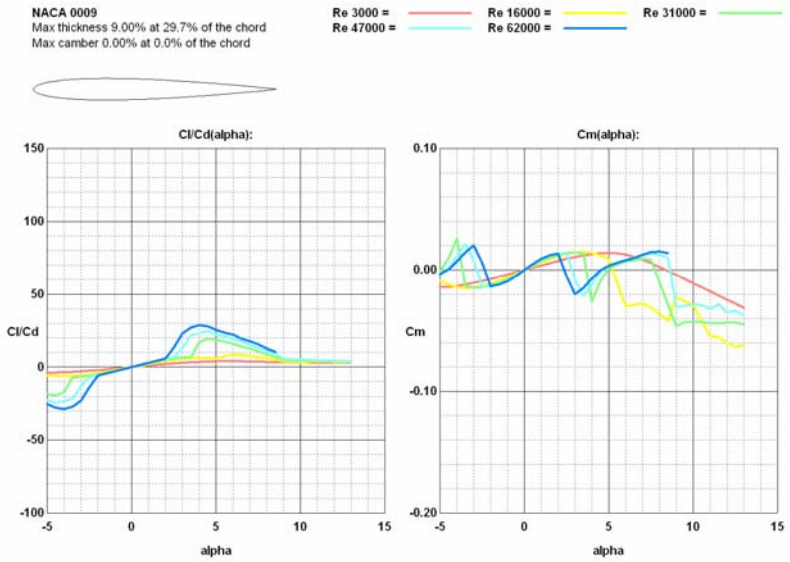

Fig. 7.10: NACA 0009 Stabilizer Tip - C_L/C_D vs. AOA and C_M vs. AOA .

7.2.3 Vertical Stabilizer Airfoils

The optimal airfoil for the vertical stabilizer was required to have low amounts of lift and drag. These properties were necessary to ensure that the vertical stabilizer geometry had as little affect as possible on the overall aerodynamic performance of the aircraft. Of the five profiles tested, the airfoil which best exhibited these key qualities was the S9033. This airfoil produced significantly less drag than the other profiles tested. In addition, it consistently produced low amounts of lift over all of the flight velocities tested. The results are illustrated below. For extensive results, refer to Appendix D.

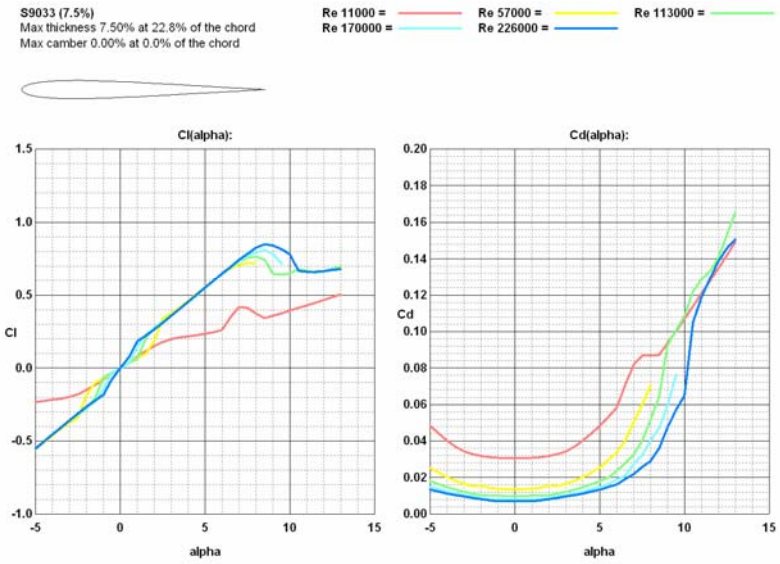

Fig. 7.11: S9033 Stabilizer Root - C_L vs. AOA and C_D vs. AOA .

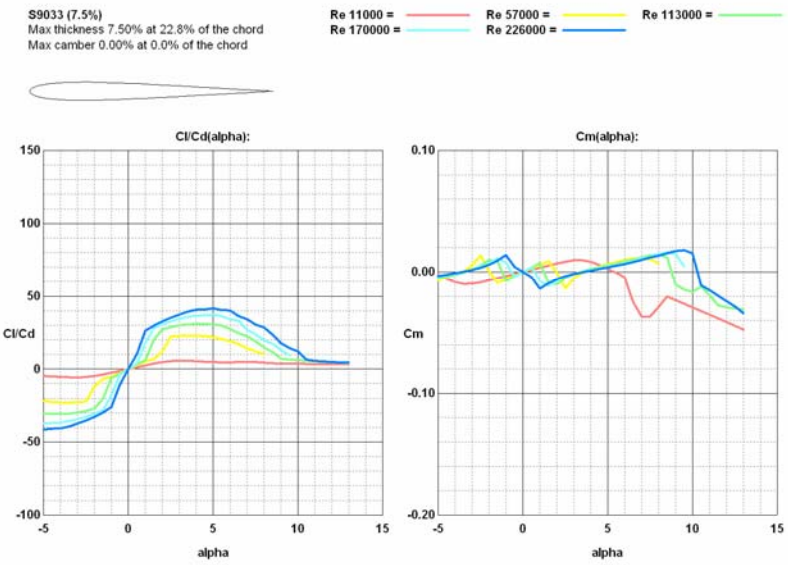

Fig. 7.12: S9033 Stabilizer Root - C_L/C_D vs. AOA and C_M vs. AOA .

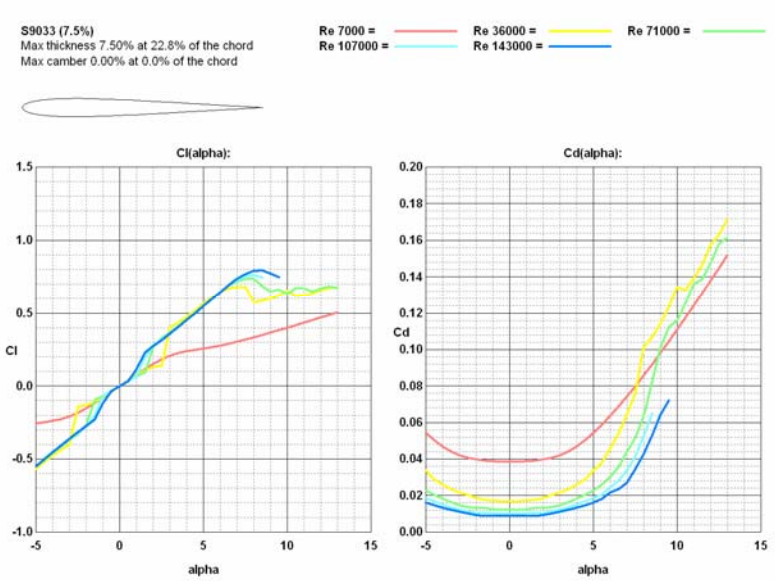

Fig. 7.13: S9033 Stabilizer Tip - C_L vs. AOA and C_D vs. AOA .

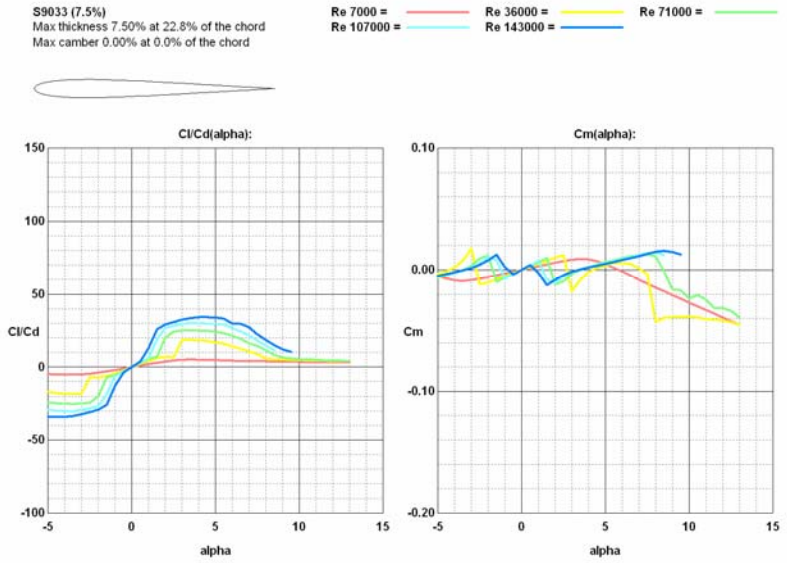

Fig. 7.14: S9033 Stabilizer Tip - C_L/C_D vs. AOA and C_M vs. AOA .

7.3 Three-Dimensional

7.3.1 Wing Planforms

Once the two dimensional analysis was completed, the optimal airfoil was extruded to form several different wing planforms. Tables 7.1-7.3 illustrate the respective lift and drag values over the amended range of flight speeds.

Table 7.1: Body Forces on Individual Wing Planforms at 10 m/s

Part	C_L	*Lift (N)*	C_D	*Drag (N)*
Rectangular Wing	0.835	9.167	0.064	0.704
Tapered Wing	0.751	6.677	0.059	0.524
Tapered Wing with Winglet	0.743	6.697	0.058	0.522
Dbl Tapered Wing	0.782	7.690	0.059	0.584
Dbl Tapered Wing with Winglet	0.774	7.658	0.059	0.587
Triple Tapered Wing with Standard Winglet	0.766	7.699	0.058	0.587
Triple Tapered Wing with High Performance Winglet	0.772	7.718	0.059	0.593

Table 7.2: Body Forces on Individual Wing Planforms at 15 m/s

Part	C_L	*Lift (N)*	C_D	*Drag (N)*
Rectangular Wing	0.840	20.741	0.063	1.545
Tapered Wing	0.756	15.121	0.057	1.148
Tapered Wing with Winglet	0.748	15.172	0.056	1.141
Dbl Tapered Wing	0.787	17.407	0.058	1.277
Dbl Tapered Wing with Winglet	0.780	17.361	0.058	1.286
Triple Tapered Wing with Standard Winglet	0.771	17.438	0.057	1.284
Triple Tapered Wing with High Performance Winglet	0.777	17.480	0.058	1.296

Table 7.3: Body Forces on Individual Wing Planforms at 20 m/s

Part	C_L	*Lift (N)*	C_D	*Drag (N)*
Rectangular Wing	0.846	37.141	0.062	2.714
Tapered Wing	0.761	27.078	0.057	2.014
Tapered Wing with Winglet	0.754	27.174	0.055	2.001
Dbl Tapered Wing	0.793	31.191	0.057	2.242
Dbl Tapered Wing with Winglet	0.764	30.979	0.056	2.254
Triple Tapered Wing with Standard Winglet	0.777	31.224	0.056	2.254
Triple Tapered Wing with High Performance Winglet	0.779	31.311	0.057	2.275

This data shows that the majority of planforms produced similar amounts of lift and drag. However, the rectangular wing produced a significantly greater amount of lift and drag, while the tapered wing produced a slightly lower amount of lift and drag, compared to the majority. This result is expected as lift and drag are directly proportional to surface area.

Through the course of this investigation, it was found that there were two possible optimal wing planforms; one where the wing geometry was fixed, and the other where the wing geometry could be varied. To determine the optimal wing planform for a fixed geometry, it required that the effective lift of the different wing planforms be calculated using the following equation:

$$Effective\ Lift = Wing\ Lift - Wing\ Weight$$

In this way, a wing that weighs more, such as the rectangular wing, results in a greater reduction in effective lift compared to a lighter wing, such as the tapered wing, which leads to a smaller reduction in effective lift. The following tables illustrate this information as well as the L/D ratio through which the planforms were optimised.

Table 7.4: Effective Lift of Individual Wing Planforms

Part	*Effective Lift (N)*		
	10 m/s	*15 m/s*	*20 m/s*
Rectangular Wing	6.232	17.806	34.206
Tapered Wing	5.152	13.596	25.552
Tapered Wing with Winglet	5.169	13.644	25.647
Dbl Tapered Wing	5.689	15.406	29.190
Dbl Tapered Wing with Winglet	5.653	15.356	28.975
Triple Tapered Wing with Standard Winglet	5.680	15.419	29.205
Triple Tapered Wing with High Performance Winglet	5.608	15.370	29.201

Table 7.5: L/D Ratio of Individual Wing Planforms

Part	*10 m/s*	*15 m/s*	*20 m/s*
Rectangular Wing	8.847	11.527	12.604
Tapered Wing	9.829	11.846	12.686
Tapered Wing with Winglet	9.908	11.961	12.819
Dbl Tapered Wing	9.747	12.063	13.021
Dbl Tapered Wing with Winglet	9.628	11.944	12.854
Triple Tapered Wing with Standard Winglet	9.678	12.006	12.958
Triple Tapered Wing with High Performance Winglet	9.462	11.856	12.834

From the table of L/D ratios we can see that the double tapered wing produces the best results over the majority of flight speeds. These values are also shown graphically in Figs. 7.15-7.17.

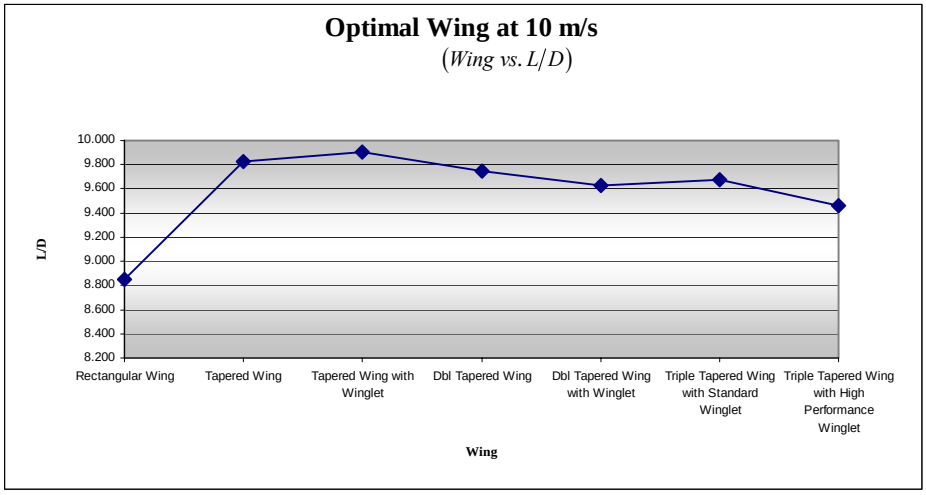

Fig. 7.15: Optimal Wing (Fixed Geometry) - Wing vs. L/D .

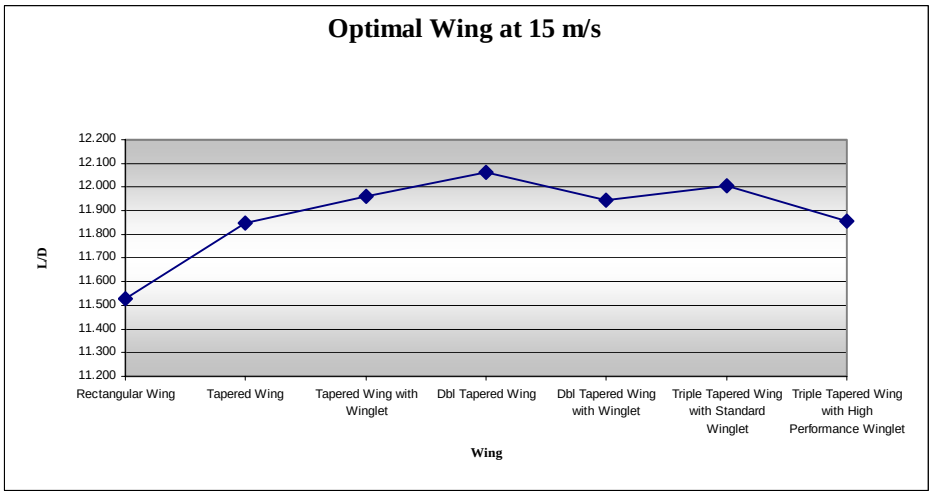

Fig. 7.16: Optimal Wing (Fixed Geometry) - Wing vs. L/D .

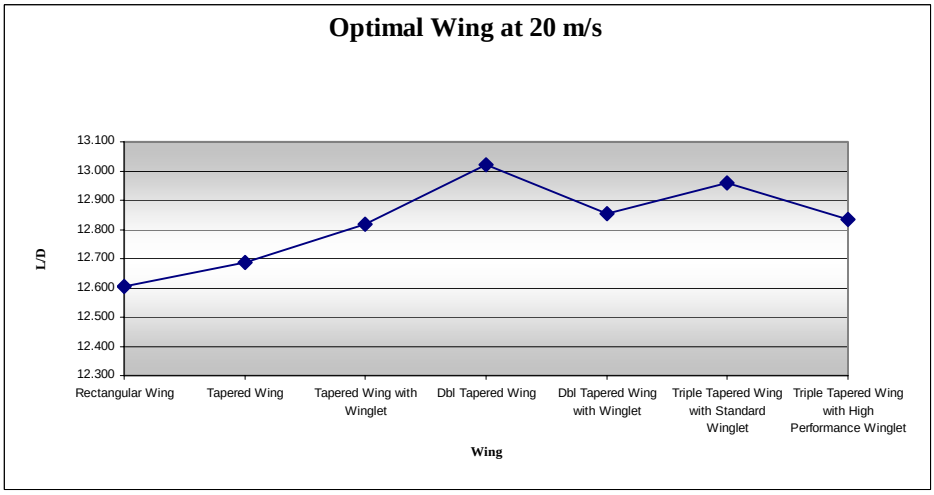

Fig. 7.17: Optimal Wing (Fixed Geometry) - Wing vs. L/D .

By normalising the L/D ratios with respect to the corresponding wing weights, the most optimal wing planform for variable geometry was determined. This was the wing that had the greatest L/D ratio per kg of wing weight. The following tables illustrate these values.

Table 7.6: L/D Ratio and Individual Normalised Body Forces at 10 m/s

Lift/Drag Ratio	*Lift Ratio (N/kg)*	*Drag Ratio (N/kg)*
13.013	61.286	4.710
12.739	85.885	6.742
12.837	86.002	6.700
13.175	75.398	5.723
13.042	74.957	5.747
13.118	74.816	5.703
13.022	71.770	5.511

Table 7.7: L/D Ratio and Individual Normalised Body Forces at 15 m/s

Lift/Drag Ratio	*Lift Ratio (N/kg)*	*Drag Ratio (N/kg)*
13.427	138.661	10.327
13.175	194.506	14.763
13.301	194.838	14.649
13.630	170.661	12.521
13.503	169.930	12.585
13.578	169.461	12.480
13.484	162.557	12.056

Table 7.8: L/D Ratio and Individual Normalised Body Forces at 20 m/s

Lift/Drag Ratio	*Lift Ratio (N/kg)*	*Drag Ratio (N/kg)*
13.685	248.305	18.144
13.443	348.306	25.910
13.583	348.981	25.693
13.914	305.801	21.978
13.743	303.233	22.064
13.854	303.432	21.902
13.762	291.174	21.158

It can be seen that the tapered wing with winglet produces the best L/D ratio per kg of wing weight.

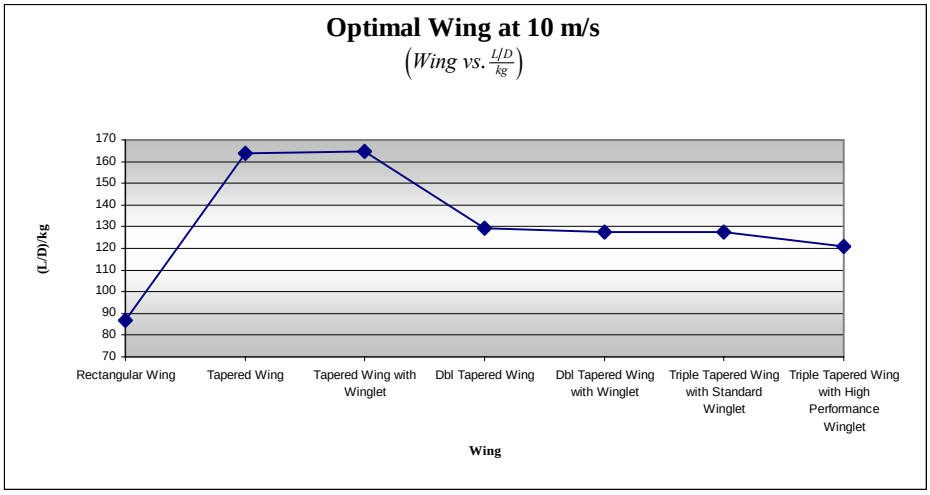

Fig. 7.18: Optimal Wing (Variable Geometry) - Wing vs. $\frac{L/D}{kg}$.

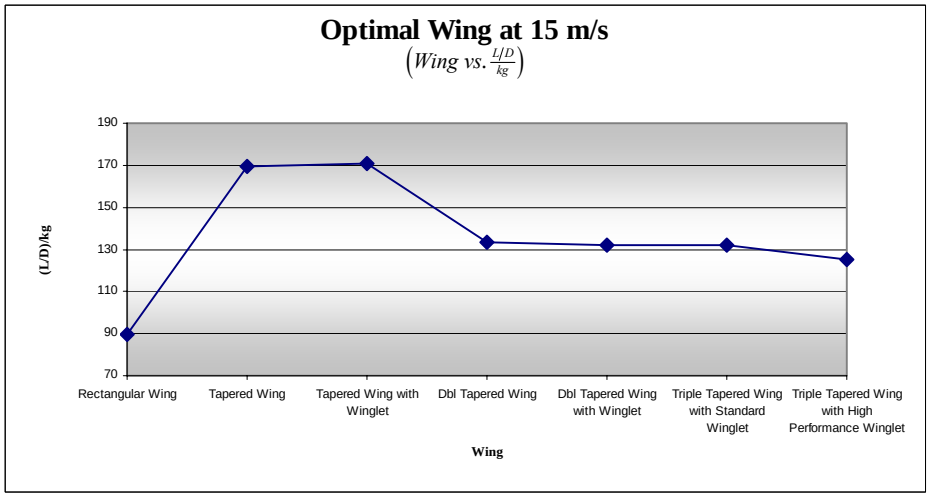

Fig. 7.19: Optimal Wing (Variable Geometry) - Wing vs. $\frac{L/D}{kg}$.

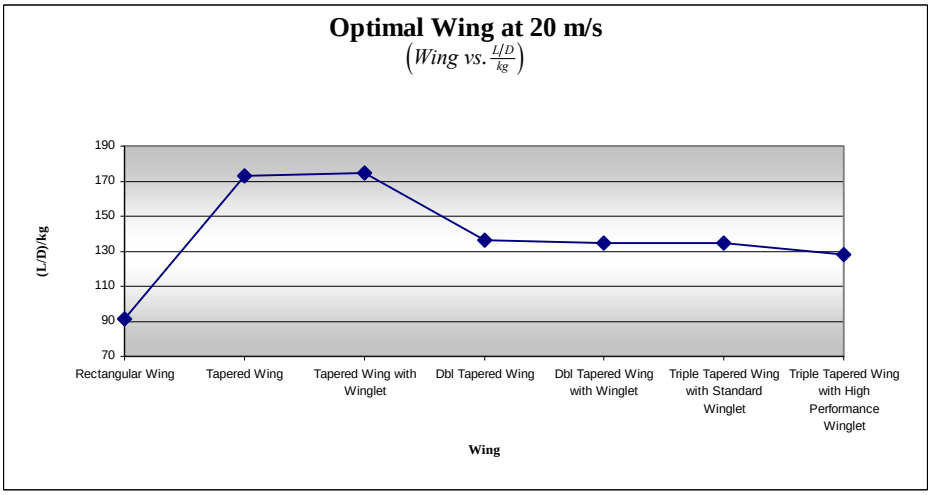

Fig. 7.20: Optimal Wing (Variable Geometry) - Wing vs. $\frac{L/D}{kg}$.

To summarise thus far, when the wing geometry was held fixed the double tapered wing produced the best L/D ratio over the tested flight speeds, and hence was classified as the most optimal wing for a wingspan of 2.5 m. Through the normalisation of the L/D ratios with respect to weight, the tapered wing with winglet produced the best $\frac{L/D}{kg}$ ratio. If the double tapered wing is employed, it will result in an increase in aircraft weight of 0.102 kg and a lift of 31 N, per wing. On the other hand, utilisation of the tapered wing with winglet will result in an increase in weight of 0.078 kg and a lift of 27 N, per wing. Given this information, the double tapered wing weight can be used as a benchmark and the size of the tapered wing with winglet increased to match this weight (0.102 kg) (Refer to Appendix C). This increase will in turn expand the wingspan and surface area, ultimately enhancing the lift produced by the wing. Ultimately, this process of optimisation leads to the tapered wing with winglet producing more lift than the double tapered wing without adding extra weight to the aircraft. The values from the CFD analysis of this wing are illustrated in the table below.

Table 7.9: Body Forces on Tapered Wing with Winglet (Varied Geometry)

Velocity	C_L	*Lift (N)*	C_D	*Drag (N)*
10 m/s	0.709	9.624	0.082	1.107
15 m/s	0.726	22.164	0.077	2.276
20 m/s	0.733	39.808	0.071	3.830

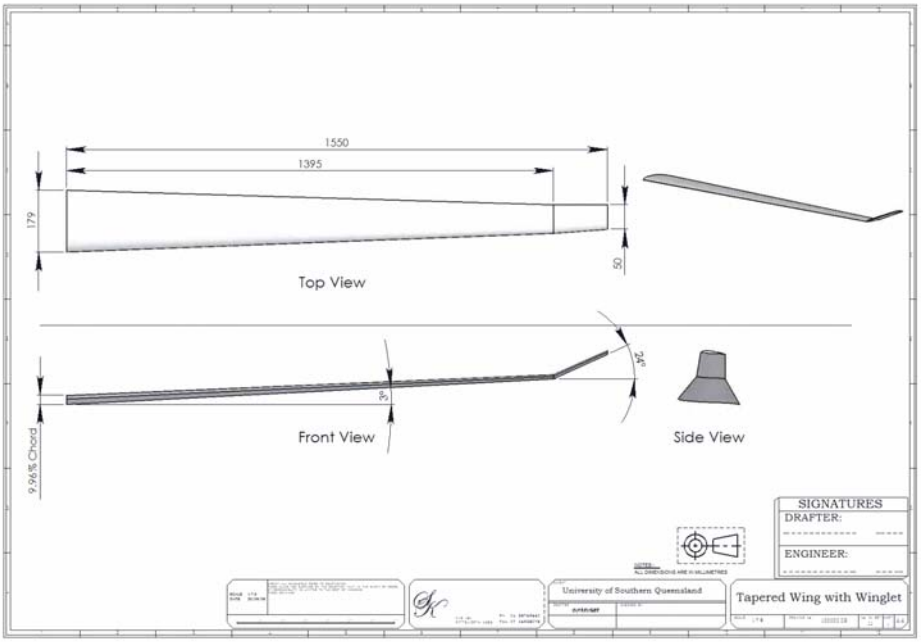

Fig. 7.21: Optimal Wing (Variable Geometry).

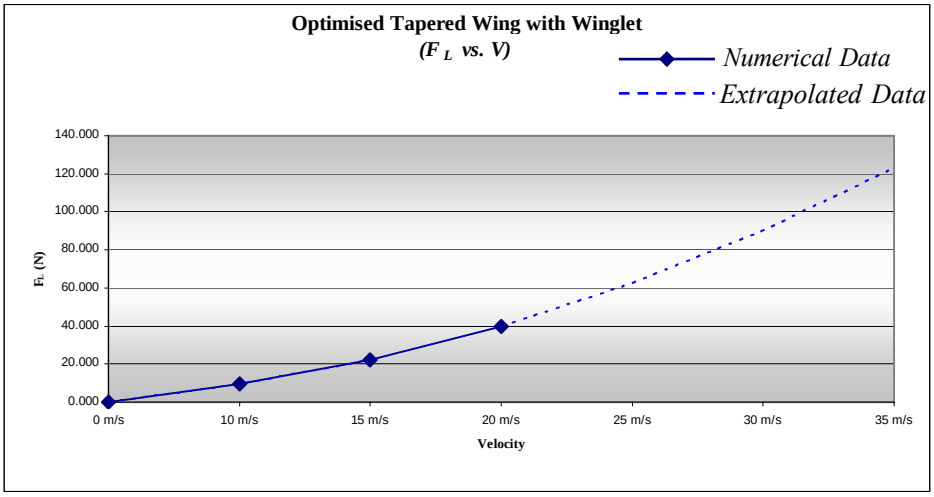

Fig. 7.22: Optimised Tapered Wing with Winglet - F_L vs. V .

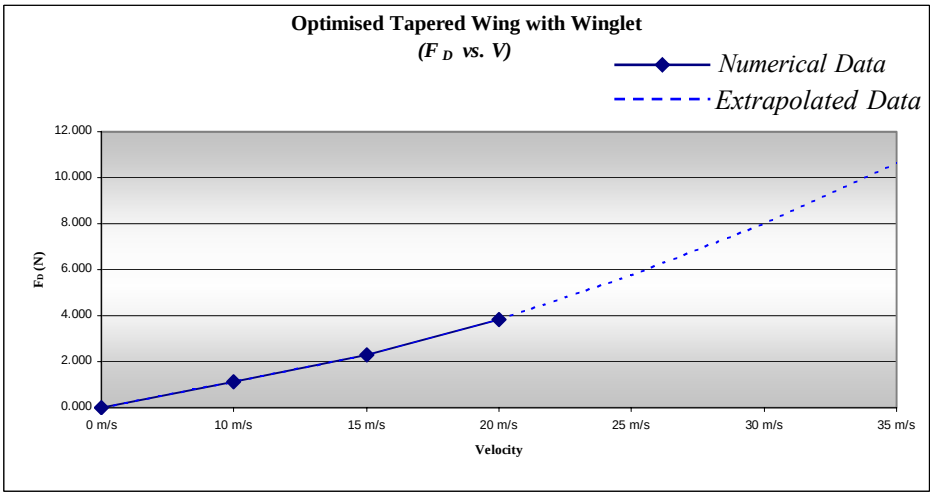

Fig. 7.23: Optimised Tapered Wing with Winglet - F_D vs. V .

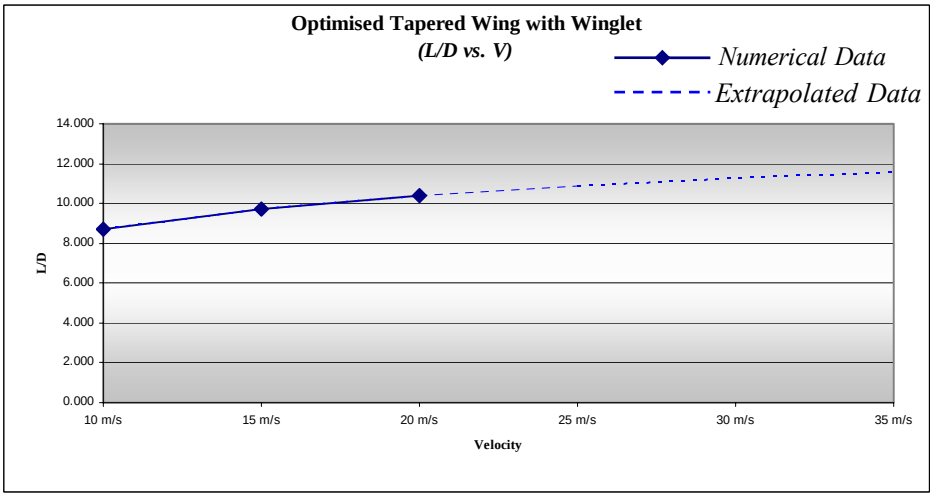

Fig. 7.24: Optimised Tapered Wing with Winglet - L/D vs. V .

In conclusion, the two possible optimal wing planforms were the double tapered wing (fixed geometry) and the tapered wing with winglet (varied geometry). Of these, the double tapered wing with winglet was chosen as the most optimal planform. This result was attributed to the significantly greater L/D ratios produced over the tested flight speeds.

The contour plots below reinforce the theory presented in chapter four regarding downwash. It can be seen that geometries that have greater amounts of surface area near the wingtip incur more downwash, as shown by the spanwise flow. In contrast, planforms that have less wing area for the trailing vortices to act on have less downwash and subsequently less induced drag.

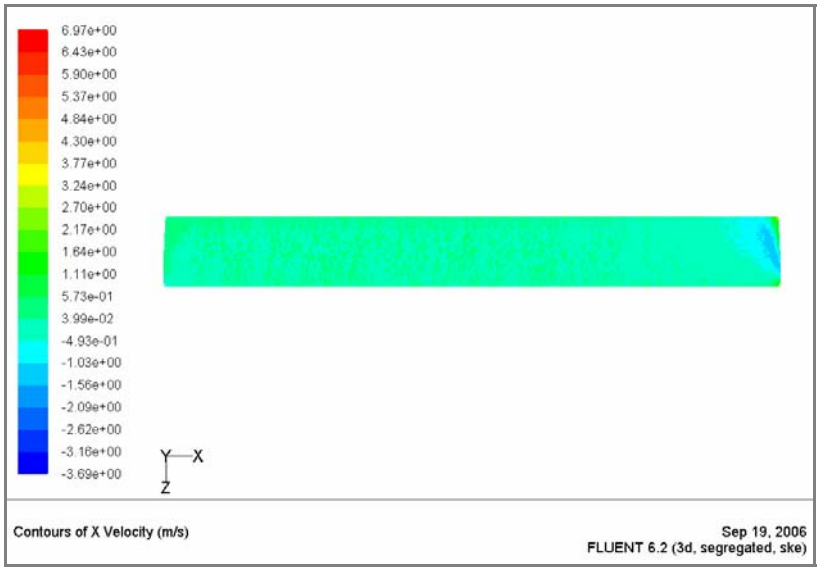

Fig. 7.25: Rectangular Wing X Velocity Contours at 20 m/s.

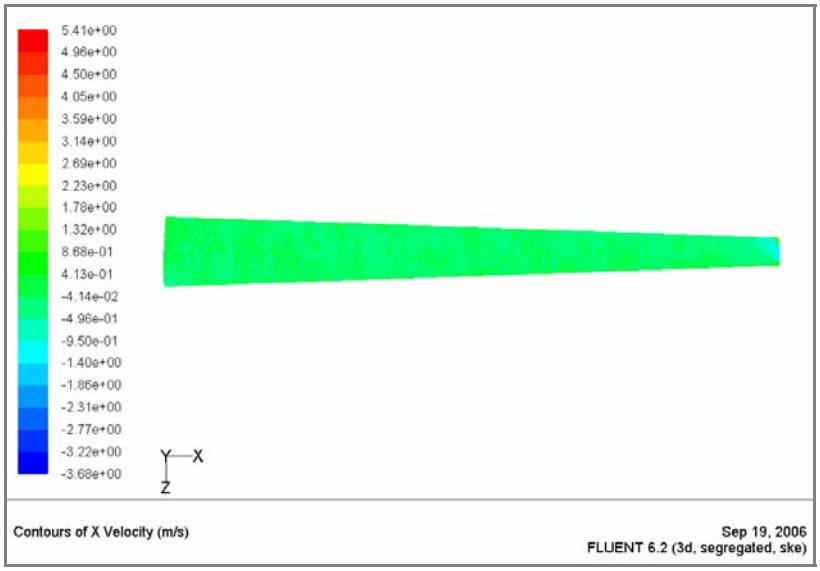

Fig. 7.26: Tapered Wing X Velocity Contours at 20 m/s.

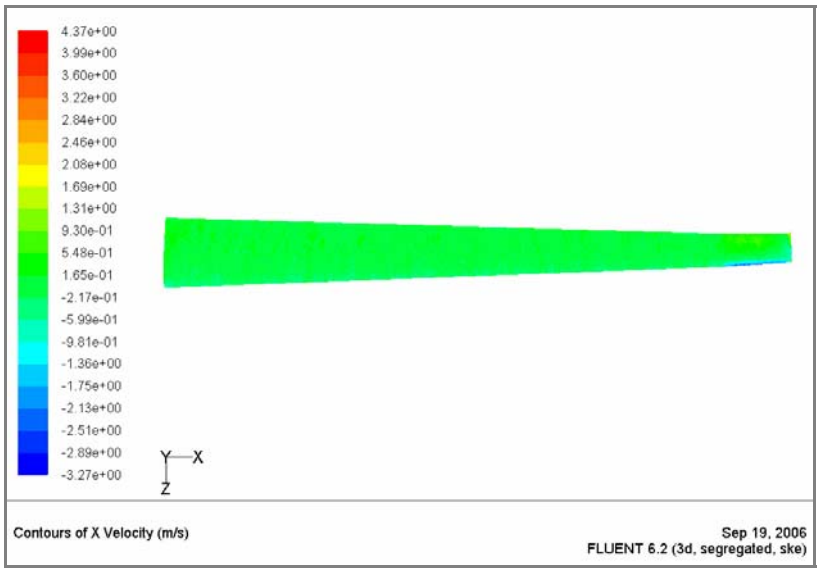

Fig. 7.27: Tapered Wing with Winglet X Velocity Contours at 20 m/s.

A substantial decrease in spanwise flow, as in Fig. 7.27, illustrates the advantage of employing winglets. This can also be substantiated by referring to Tables 7.1-7.3, which show that planforms with winglets have less drag than those without. The benefits of winglets are most obvious at higher flight velocities. At lower velocities, the added surface area of the winglet increases profile drag. For extensive results and contour plots, refer to Appendix E.

7.3.2 Fuselage

Tables 7.10-7.12 illustrate the lift and drag values on the fuselage over the tested flight speeds.

Table 7.10: Body Forces on Fuselage at 10 m/s

Part	C_L	*Lift (N)*	C_D	*Drag (N)*
Fuselage	-0.002	-0.031	0.008	0.126

Table 7.11: Body Forces on Fuselage at 15 m/s

Part	C_L	*Lift (N)*	C_D	*Drag (N)*
Fuselage	-0.002	-0.072	0.008	0.262

Table 7.12: Body Forces on Fuselage at 20 m/s

Part	C_L	*Lift (N)*	C_D	*Drag (N)*
Fuselage	-0.085	-0.128	0.030	0.445

The results indicate that the generic fuselage actually produced a slight amount of negative lift. This finding was of particular interest as this fuselage has been recently employed in the award winning 1999 Discus 2 sailplane. It was thought that this fuselage would produce positive lift values. Also of particular interest were the drag values, which were much lower than anticipated. These values are also illustrated graphically in the figures below.

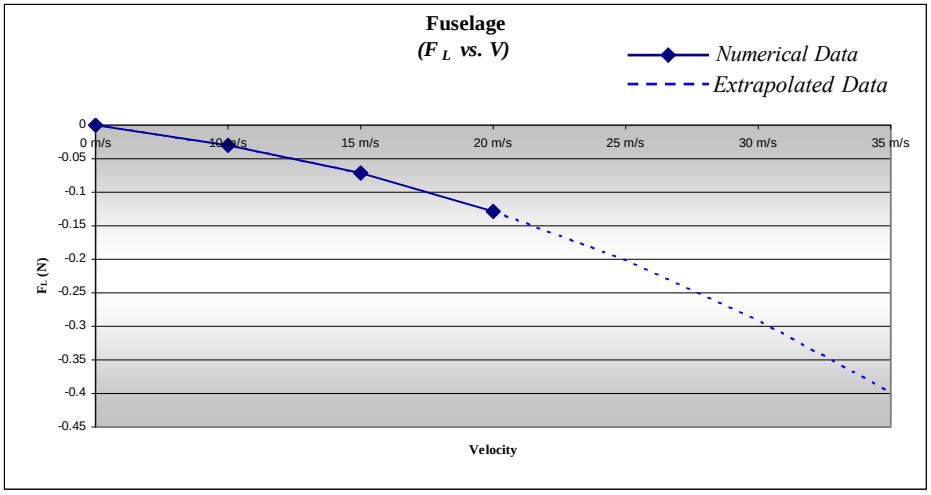

Fig. 7.28: Fuselage- F_L vs. V .

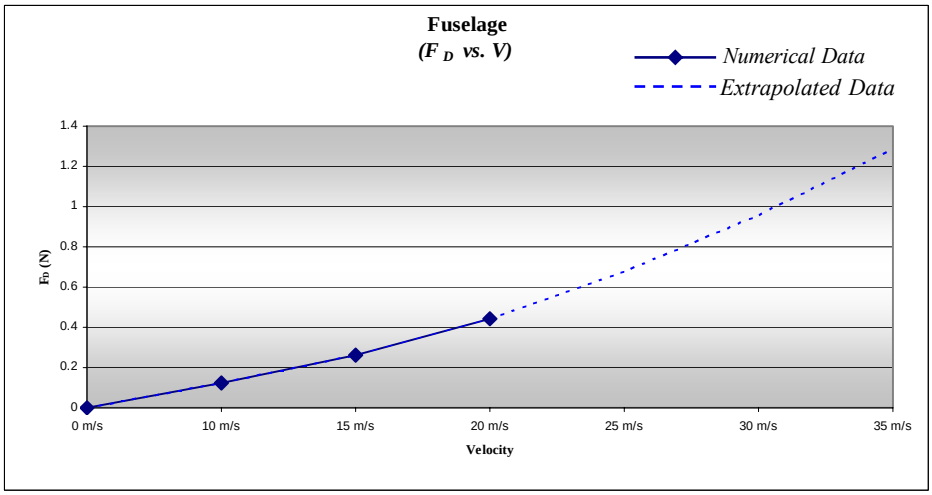

Fig. 7.29: Fuselage - F_D vs. V .

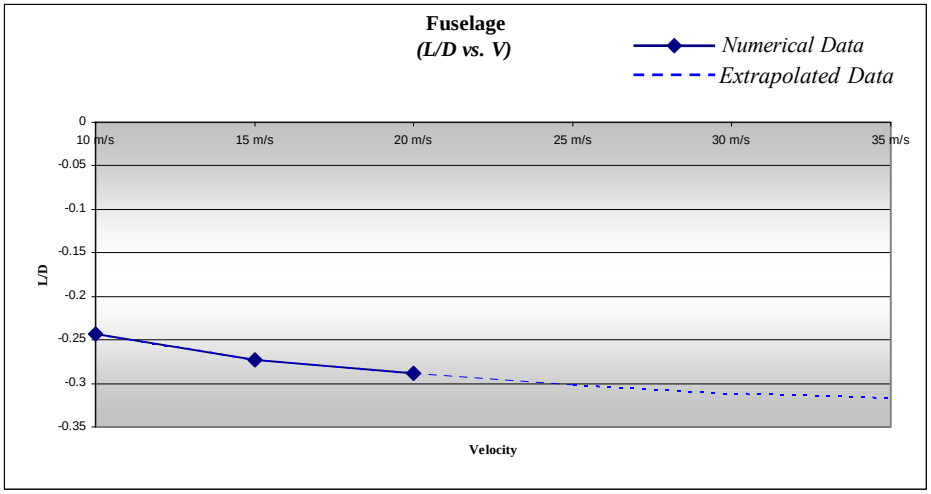

Fig. 7.30: Fuselage - L/D vs. V .

The following dynamic pressure plot shows flow separation by illustrating where kinetic energy is at its highest (Fig. 7.31). These positions, mainly around the cockpit area, are consistent with those shown in chapter five. In addition, the turbulence intensity plot in Fig. 7.32 indicates where the separated flow interacts with the fuselage geometry. This occurs over the aft fuselage, and results in increased levels of drag. If the region of flow separation could be further delayed and the resulting turbulence avoided, less drag would occur. For extensive results and contour plots, refer to Appendix E.

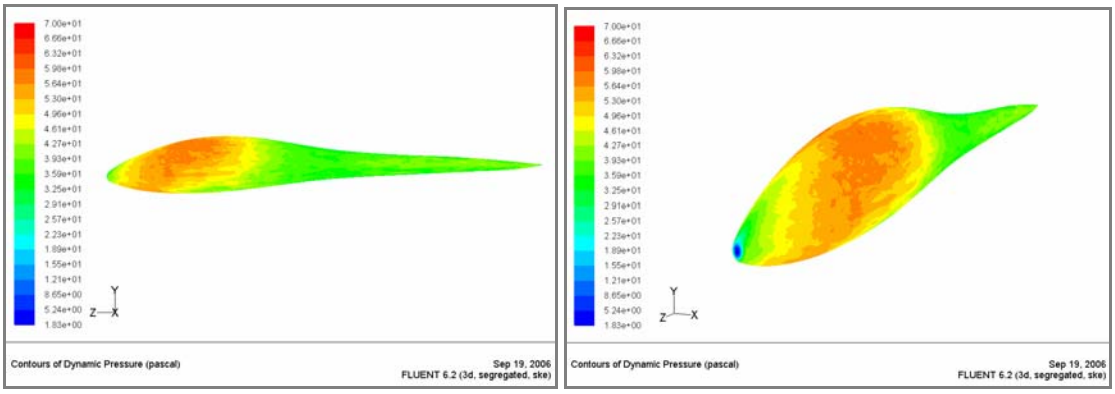

Fig. 7.31: Dynamic Pressure Contours on Fuselage at 20 m/s.

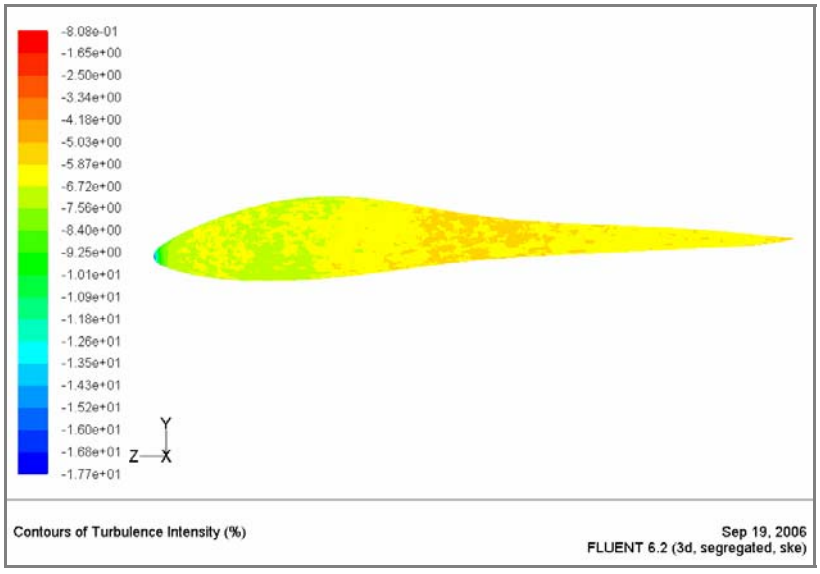

Fig. 7.32: Turbulence Intensity Contours on Fuselage at 20 m/s.

7.3.3 Tail Assembly

As previously mentioned, the tail assembly geometry was analysed at five different angles of attack for the stability analysis. The results presented below have been separated into components to allow a better comparison of the tail assembly geometry over varying flight speeds. It can be seen from the results that the lift forces increase quickly as the angle of attack is increased, while the drag forces remain relatively constant over the range of angles. For extensive results and contour plots, refer to Appendix E.

Table 7.13: Body Forces on Tail Assembly at 10 m/s

Horizontal Stabilizer				
AOA	***C_L***	***Lift (N)***	***C_D***	***Drag (N)***
6 deg	0.449	0.812	0.064	0.116
3 deg	0.351	0.634	0.063	0.114
0 deg	0	0	0.034	0.060
-3 deg	-0.351	-0.634	0.063	0.114
-6 deg	-0.449	-0.812	0.064	0.116

Vertical Stabilizer			
C_L	***Lift (N)***	***C_D***	***Drag (N)***
0	0	0.045	0.081

Table 7.14: Body Forces on Tail Assembly at 15 m/s

Horizontal Stabilizer				
AOA	***C_L***	***Lift (N)***	***C_D***	***Drag (N)***
6 deg	0.467	1.897	0.056	0.226
3 deg	0.358	1.455	0.055	0.222
0 deg	0	0	0.033	0.130
-3 deg	-0.358	-1.455	0.055	0.222
-6 deg	-0.467	-1.897	0.056	0.226

Vertical Stabilizer			
C_L	***Lift (N)***	***C_D***	***Drag (N)***
0	0	0.005	0.154

Table 7.15: Body Forces on Tail Assembly at 20 m/s

Horizontal Stabilizer				
AOA	***C_L***	***Lift (N)***	***C_D***	***Drag (N)***
6 deg	0.438	3.168	0.050	0.362
3 deg	0.361	2.607	0.050	0.361
0 deg	0	0	0.032	0.226
-3 deg	-0.361	-2.607	0.050	0.361
-6 deg	-0.438	-3.168	0.050	0.362

Vertical Stabilizer			
C_L	***Lift (N)***	***C_D***	***Drag (N)***
0	0	0.008	0.248

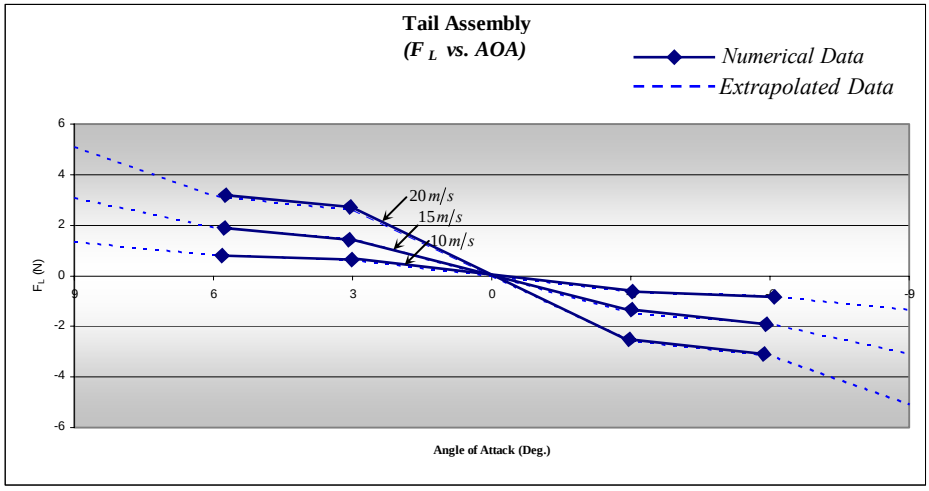

Fig. 7.33: Tail Assembly Comparison - F_L vs. AOA .

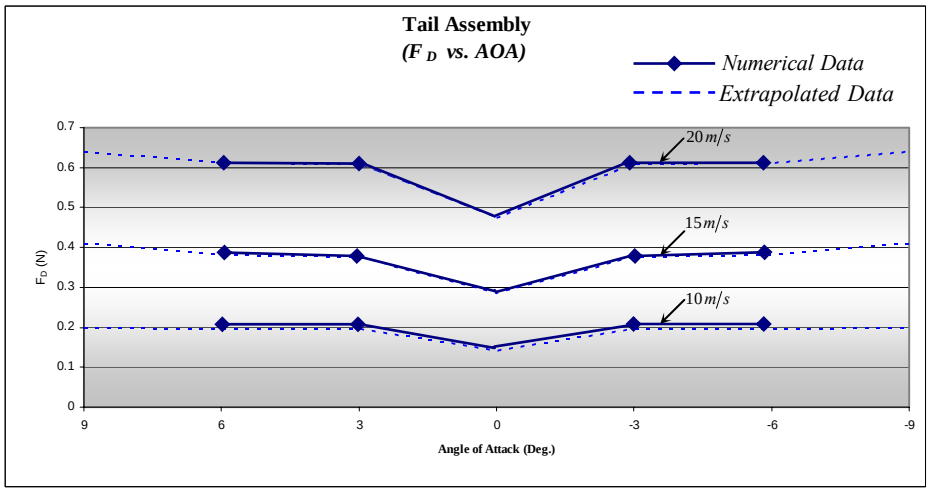

Fig. 7.34: Tail Assembly Comparison - F_D vs. AOA .

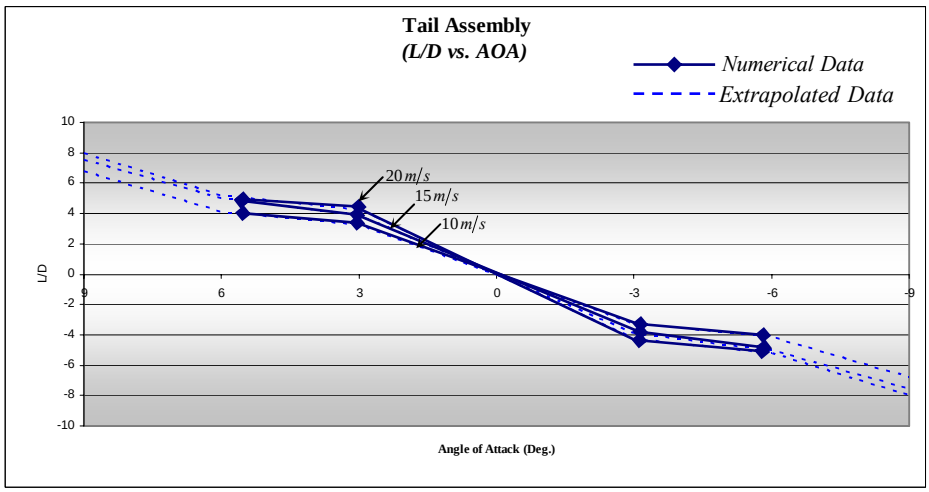

Fig. 7.35: Tail Assembly Comparison - L/D vs. AOA .

7.3.4 Sailplane

The complete sailplane geometry was analysed with both the double tapered wing and the tapered wing with winglet, in order to compare the differences. The results indicate that the sailplane with the tapered wing with winglet produced marginally better results. This is contrast to the results obtained from the wing planform analysis outlined earlier. These results are an obvious consequence of component interference. The results are substantiated below.

Table 7.16: Body Forces on Sailplane with Double Tapered Wing

Velocity	*Lift (N)*	*Drag (N)*
10 m/s	15.375	2.915
15 m/s	35.913	5.736
20 m/s	66.563	9.238

Table 7.17: Body Forces on Sailplane with Tapered Wing with Winglet

Velocity	*Lift (N)*	*Drag (N)*
10 m/s	17.166	3.126
15 m/s	40.431	6.197
20 m/s	73.327	10.169

The following graphs illustrate the previously tabulated results and provide a comparison between the two optimised sailplane geometries.

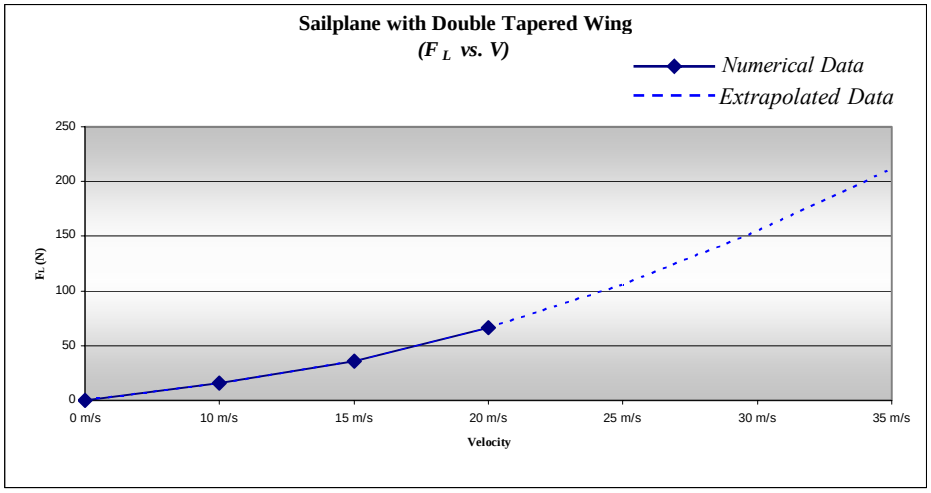

Fig. 7.36: Sailplane with Double Tapered Wing - F_L vs. V .

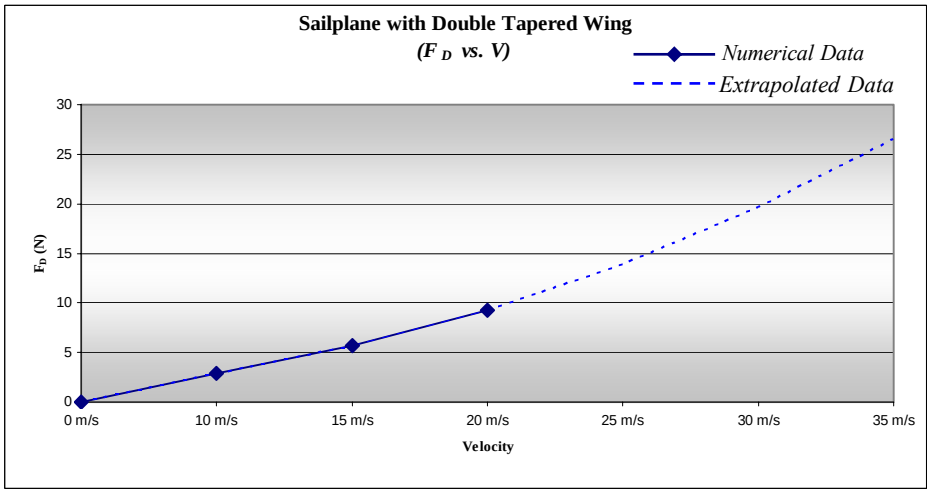

Fig. 7.37: Sailplane with Double Tapered Wing - F_D vs. V .

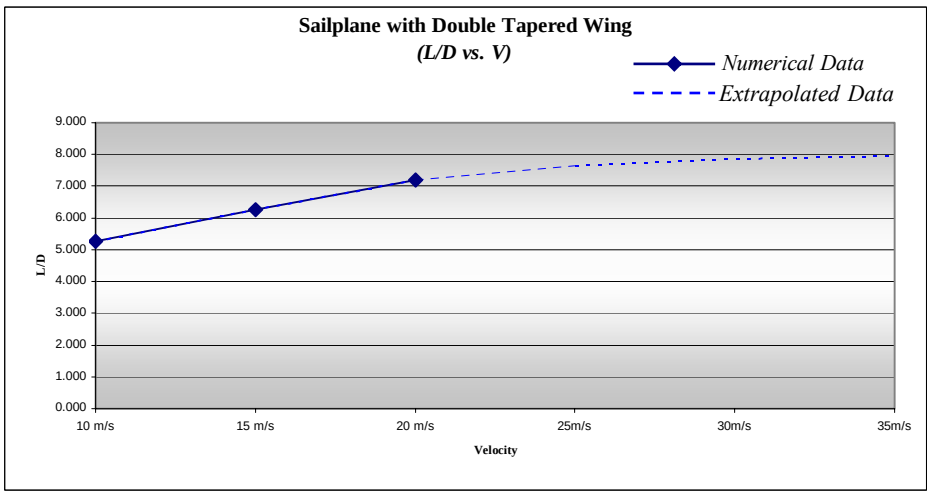

Fig. 7.38: Sailplane with Double Tapered Wing - L/D vs. V .

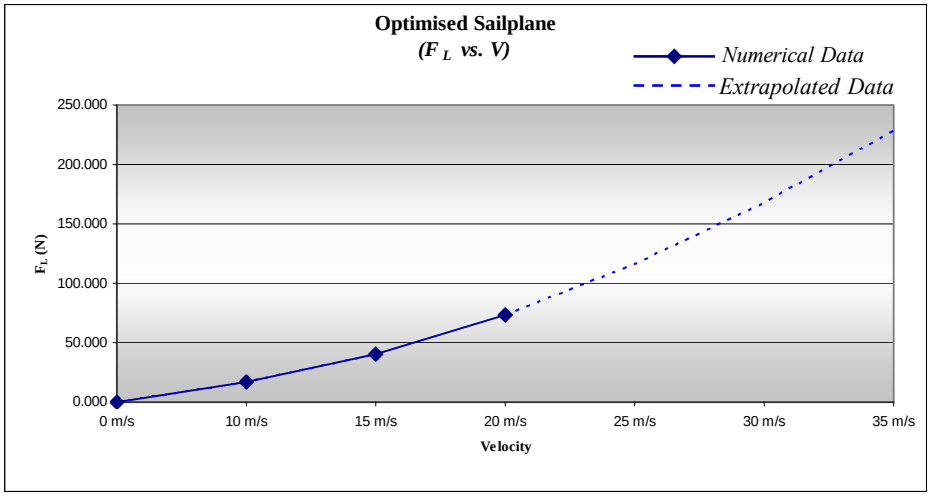

Fig. 7.39: Sailplane with Tapered Wing with Winglet - F_L vs. V .

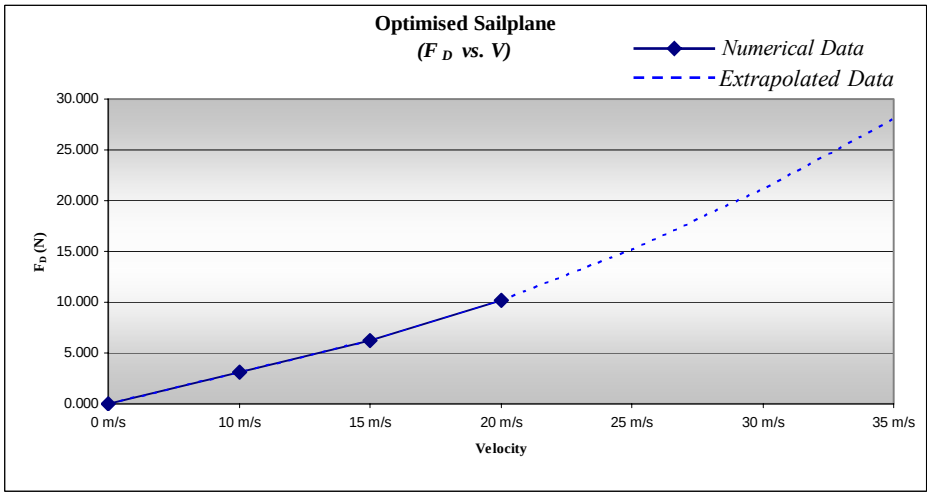

Fig. 7.40: Sailplane with Tapered Wing with Winglet - F_D vs. V .

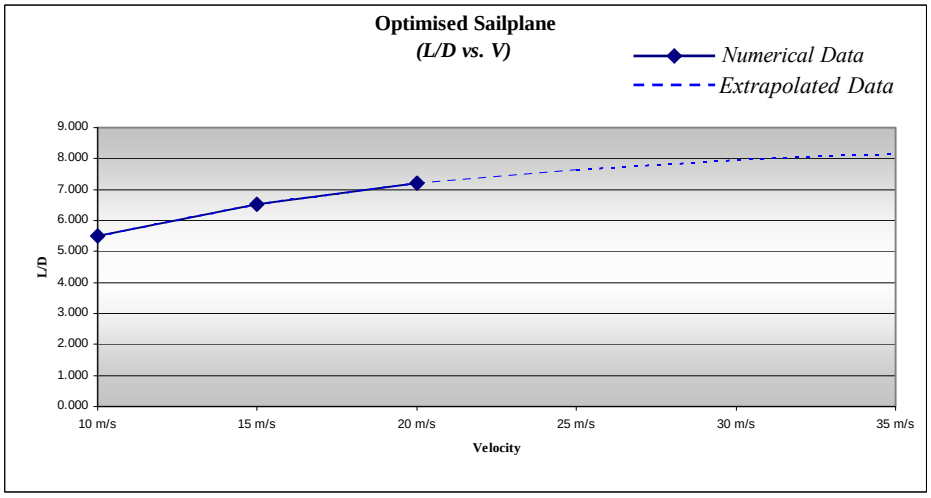

Fig. 7.41: Sailplane with Tapered Wing with Winglet - L/D vs. V .

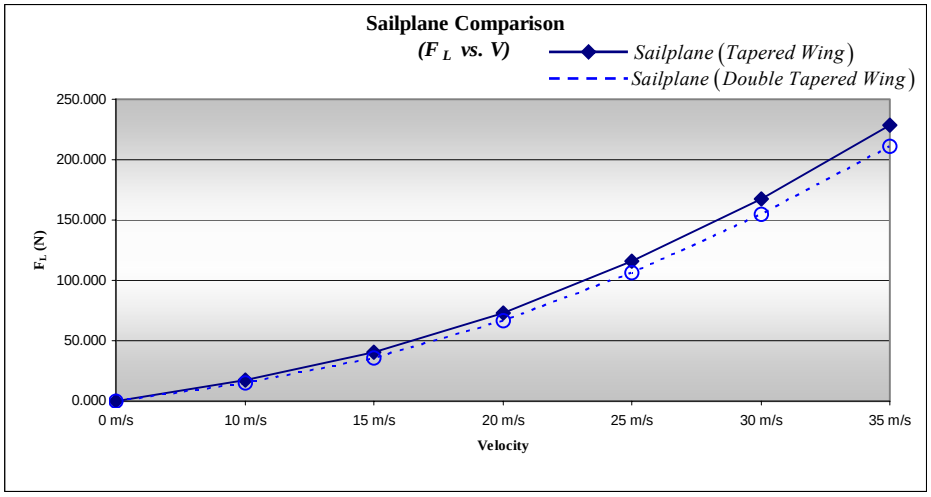

Fig. 7.42: Sailplane Comparison - F_L vs. V .

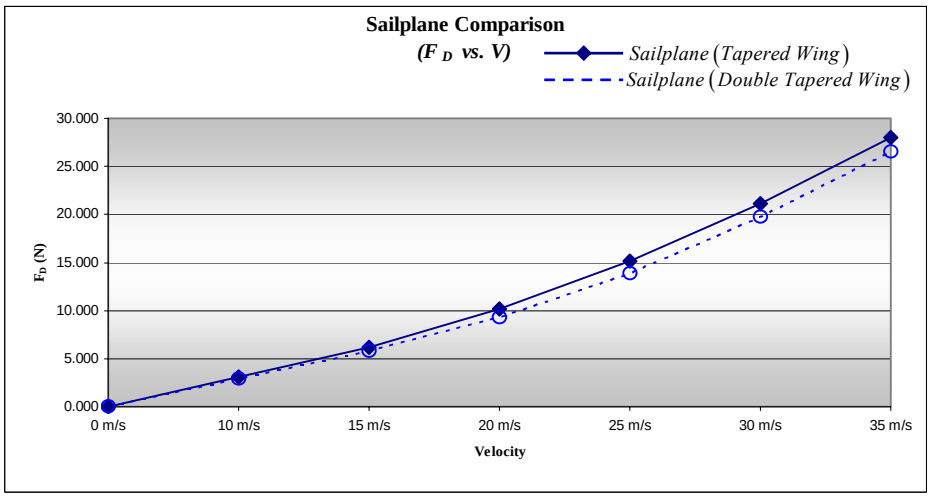

Fig. 7.43: Sailplane Comparison - F_D vs. V .

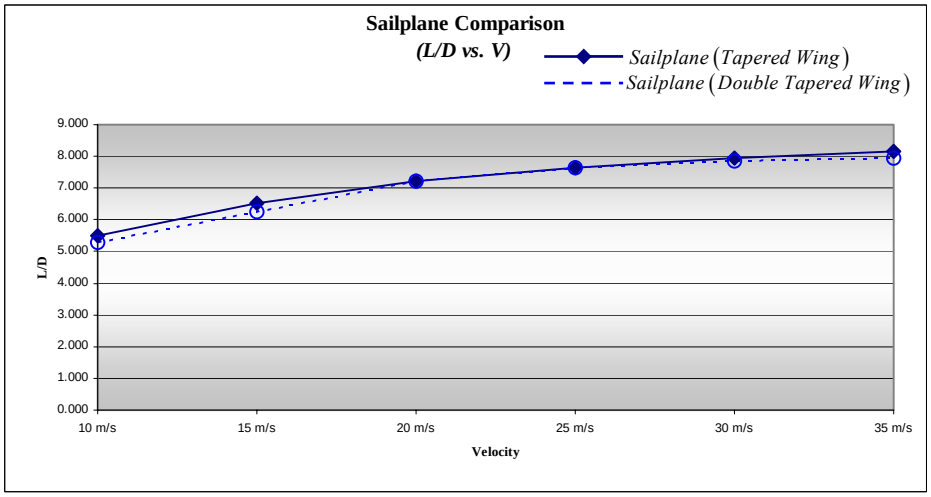

Fig. 7.44: Sailplane Comparison - L/D vs. V .

The results indicate that the sailplane with the double tapered wing had significantly less lift and more drag as a result of interference. Therefore, it can be concluded that although the double tapered wing (fixed geometry) produced far better L/D ratios than the tapered wing with winglet (varied geometry) when analysed individually, the interference due to combining the sailplane geometry resulted in the tapered wing with winglet producing marginally better results. The detrimental effects on drag and lift caused by combining the sailplane components are illustrated in the following figures.

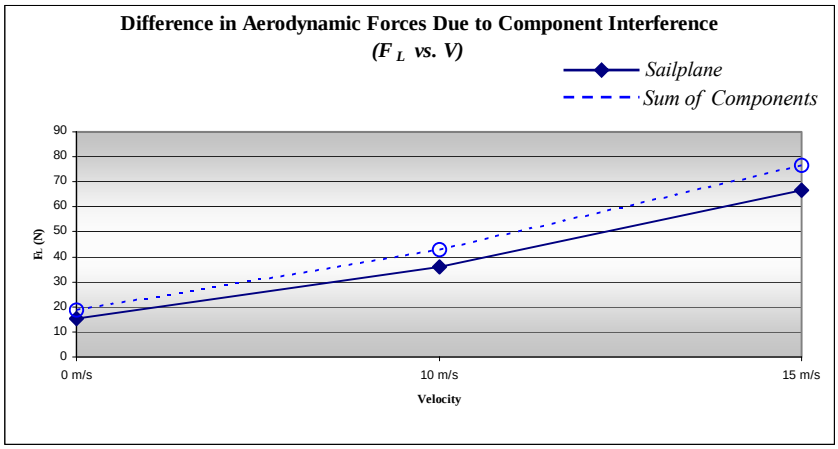

Fig. 7.45: Reduction in Lift due to Interference (Sailplane Double Tapered Wing).

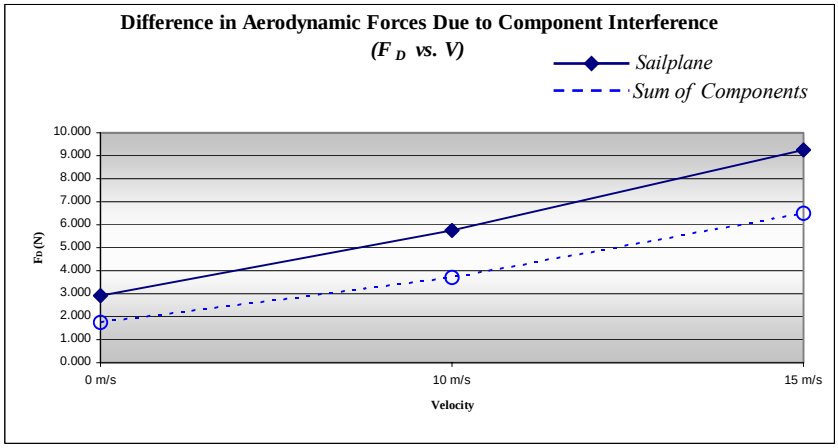

Fig. 7.46: Increase in Drag due to Interference (Sailplane Double Tapered Wing).

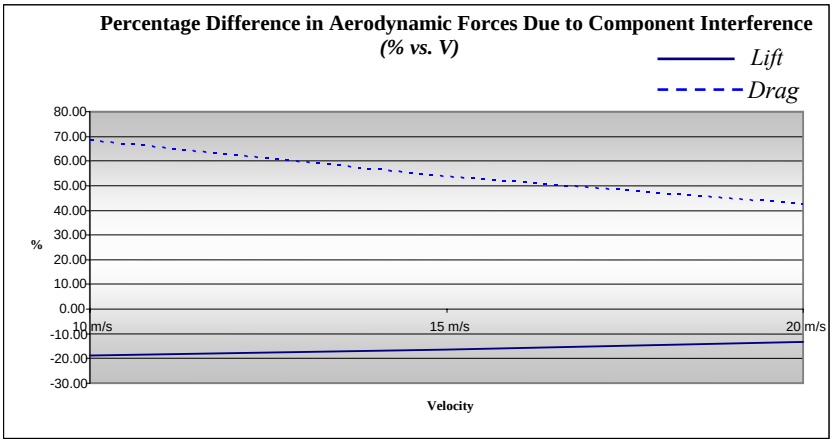

Fig. 7.47: % Difference in Aerodynamic Forces (Sailplane Double Tapered Wing).

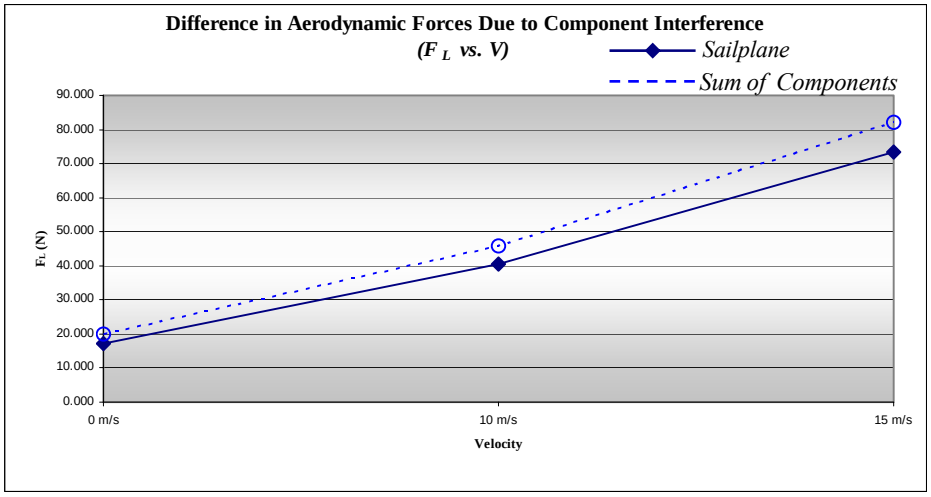

Fig. 7.48: Reduction in Lift due to Interference (Sailplane Tapered Wing).

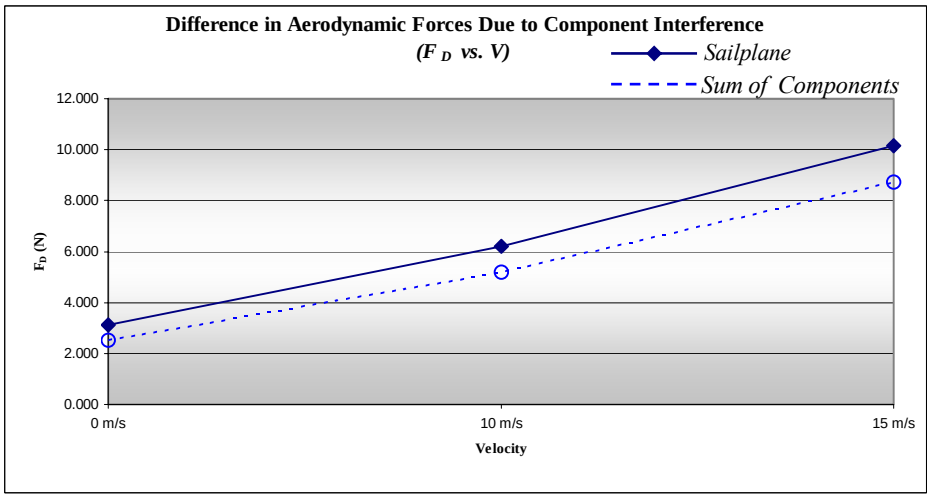

Fig. 7.49: Increase in Drag due to Interference (Sailplane Tapered Wing).

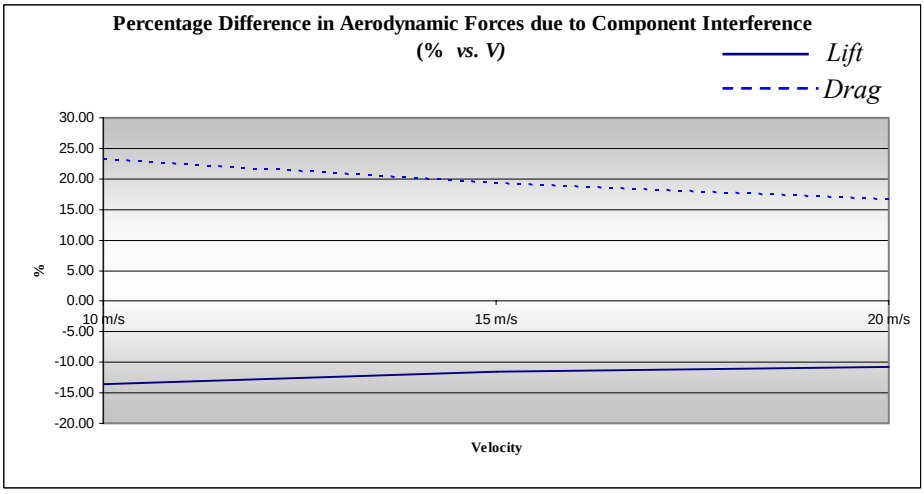

Fig. 7.50: % Difference in Aerodynamic Forces (Sailplane Tapered Wing).

The following plots illustrate the interference at the wing/fuselage and fuselage/tail junctions. The dynamic pressure plot shows the possible location of flow separation, whilst the turbulence intensity plot indicates the regions where the separated flow interacts with the sailplane geometry. These regions typically occur on the aft fuselage and extend upward into the vertical stabilizer. For extensive results and contour plots, refer to Appendix E.

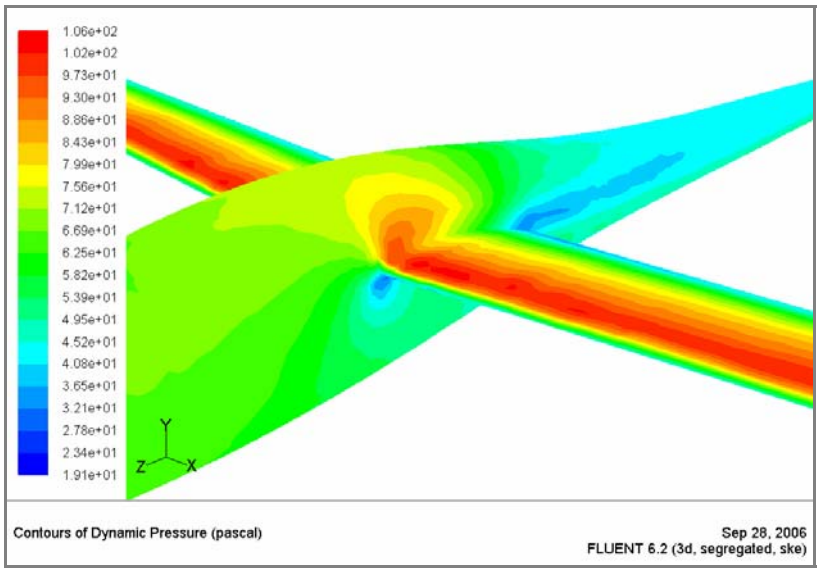

Fig. 7.51: Dynamic Pressure Contours on Sailplane at 20 m/s.

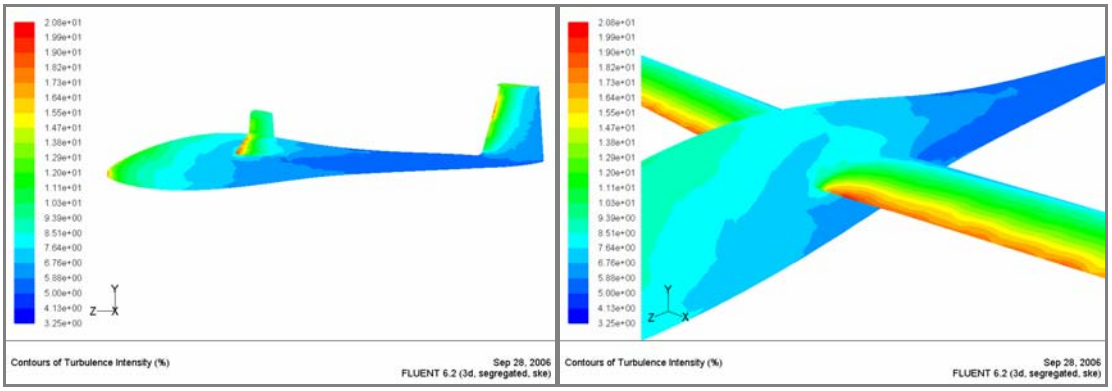

Fig. 7.52: Turbulence Intensity Contours on Sailplane at 20 m/s.

7.3.5 Aircraft Stability Analysis

To determine whether the chosen horizontal stabilizer would produce the required force necessary to ensure both static and dynamic stability, a stability analysis was conducted. This analysis was conducted assuming the sailplane was fitted with the tapered wing with winglet.

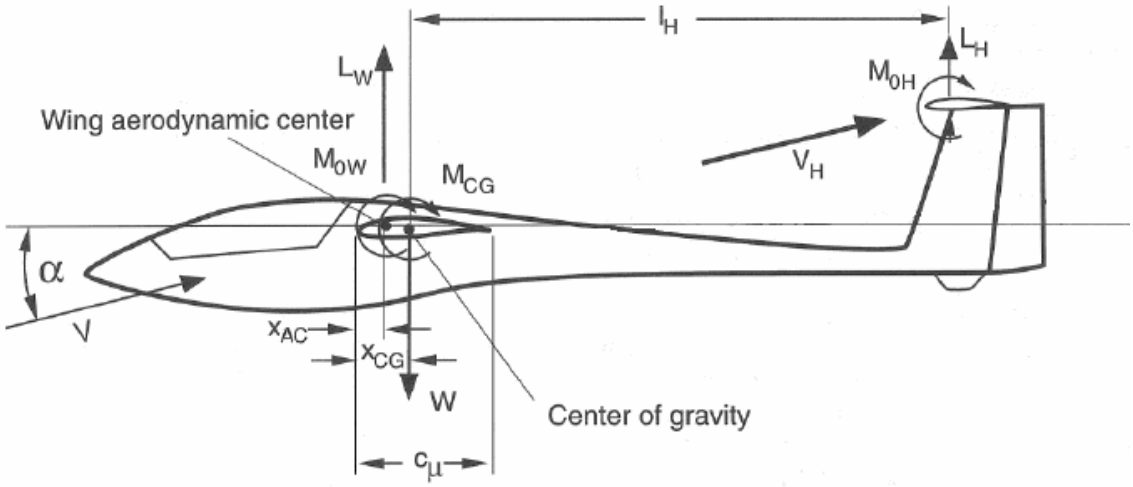

Fig. 7.53: Force and Moment Definitions for Longitudinal Stability.

Static Stability

Setting the stability margin and CG range,

Stability Margin $\left(x_{CG}-x_N\right)/c_\mu=-0.05$, $\quad \dfrac{x_{CG}}{c_\mu}=0.5$

$$\sum M_{CG}=L_w\left(x_{CG}-x_{AC}\right)+M_{0w}-M_H=0 \qquad (30)$$ or;

$$C_{L_H}\frac{dC_{L_w}/d\alpha_w}{dC_{L_H}/d\alpha_H}\frac{V_H}{V_W}=C_{L_w}\left(\frac{x_{CG}}{c_\mu}-0.25\right)+C_{M_{0w}} \qquad (31)$$

The horizontal stabilizer contribution for static stability at 10 m/s is calculated using Eq. 30 as,

$$\sum M_{CG}=19.248\left(0.0750-0.0375\right)+\left(\tfrac{1}{2}\times-0.07\times1.225\times10^2\times\left(0.0750-0.0375\right)\right)-\left(0.640\times L_H\right)$$
$$0=0.722-0.161-0.64L_H$$
$$L_H=0.877\ N$$

Corresponds to horizontal stabilizer at $AOA\approx 6$ deg

Similarly, at 15 m/s and 20 m/s respectively,

$$L_H = 2.03\,N, \qquad AOA \approx 6\,\text{deg}$$
$$L_H = 3.660\,N, \qquad AOA \approx 7\,\text{deg}$$

Through cross-referencing with Figs. 7.7-7.10, it can be seen that the horizontal stabilizer remains in the pre-stall region.

Dynamic Stability

Using the Eq. 31, the range for the lift coefficient of the horizontal stabilizer for dynamic stability can be found, as illustrated below.

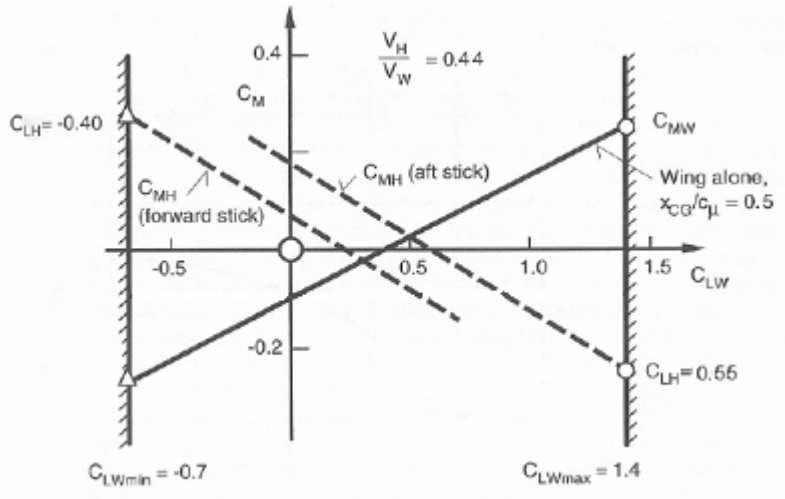

Fig. 7.54: Equilibrium Conditions for Maximum and Minimum Wing Lift Coefficients.

The results of the stability analysis indicate that the chosen horizontal stabilizer provides both static and dynamic stability remaining within the pre-stall region. With these parameters determined, stability of the sailplane can be ensured.

7.3.6 Aerodynamic Analysis Summary

The results of the two dimensional analysis were imperative to the overall aerodynamic analysis. However, without the three dimensional analysis the optimisation of the prototype would not have been achieved. The optimisation process found that two possible optimal wing planforms existed. These planforms were the double tapered wing (fixed geometry) and the tapered wing with winglet (varied geometry). Furthermore, the three-dimensional study highlighted areas of particular concern. These included the generic fuselage and tail assembly, as well as the interactions of the sailplane components. In addition, the stability analysis reinforced that the horizontal stabilizer was adequate to ensure both static and dynamic stability. In conclusion, it was decided that the sailplane with the tapered wing with winglet was the optimal design in comparison to the sailplane with the double tapered wing.

7.4 Structural

7.4.1 Static Analysis

The static stress analysis was conducted to determine if the optimised sailplane structure could withstand the aerodynamic loads placed on it during normal operation. This analysis was conducted at a flight velocity of 20 m/s.

The results indicate that the regions surrounding the wing/fuselage junction incur stress levels of approximately four megapascals. Fortunately, these levels are well below that of the material yield (See Appendix C). In contrast, the stress at the vertical/horizontal stabilizer junction is almost non-existent (Fig. 7.55). These differing conditions can obviously attributed to the different moment arms created by the wing and horizontal stabilizer geometries.

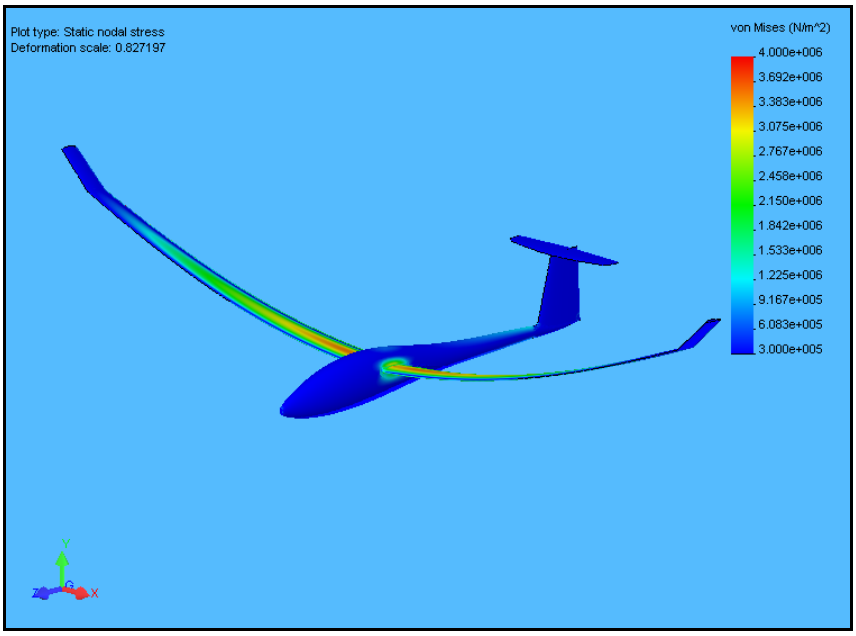

Fig. 7.55: Von Mises Stress on Sailplane at 20 m/s.

The close up view provided in Fig. 7.56 illustrates how the maximum stress region occurs through the centre of the wing geometry, however does not extend into the connected fuselage structure. This can be attributed to the wing/fuselage fairing that acts to distribute the stress over this region.

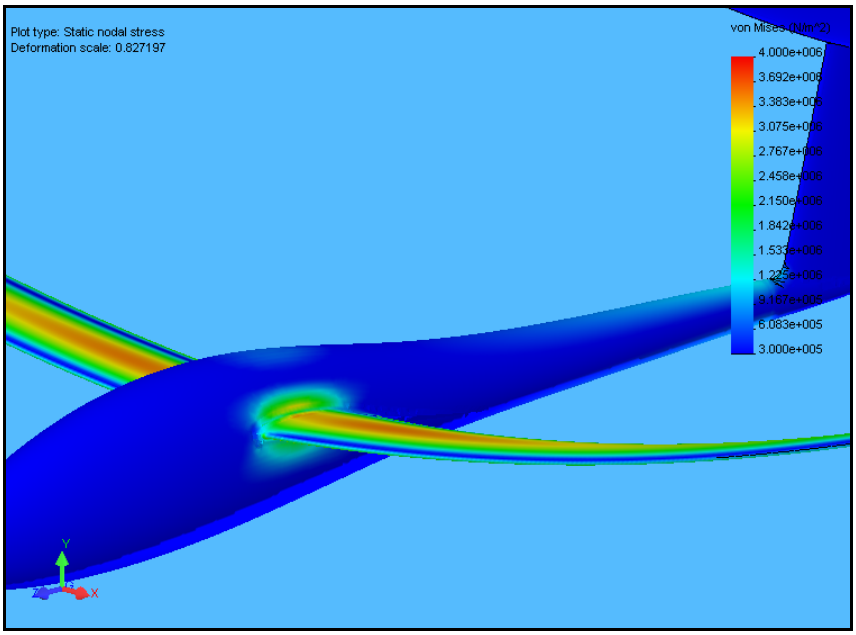

Fig. 7.56: Close up of Wing Stress at 20 m/s.

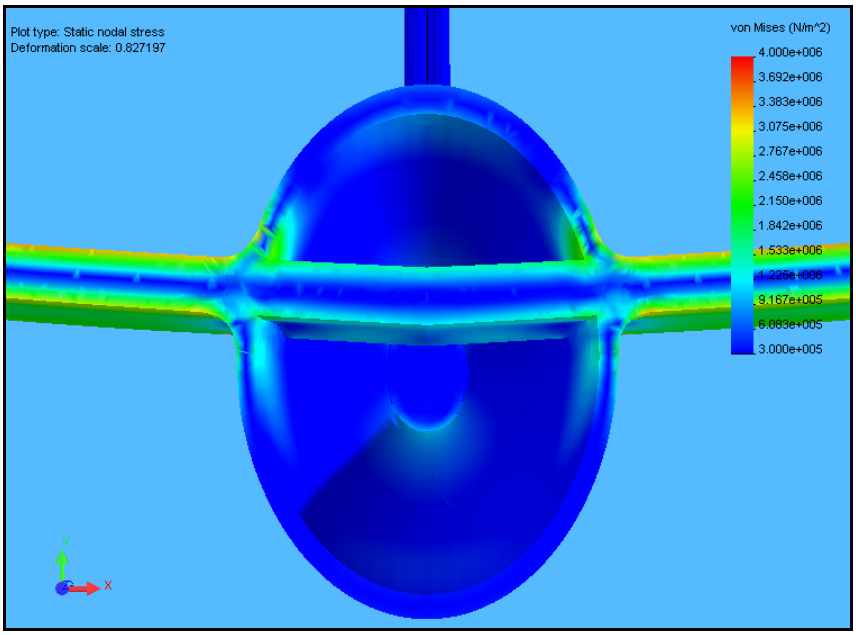

Fig. 7.57: Sectional View through Wing Mid-plane.

In addition, it can be seen in Fig. 7.57, that the stress in the wing/fuselage junction is minimised further through the inward extension of the wing geometry. This extension also provides a certain degree of additional torsional stiffness.

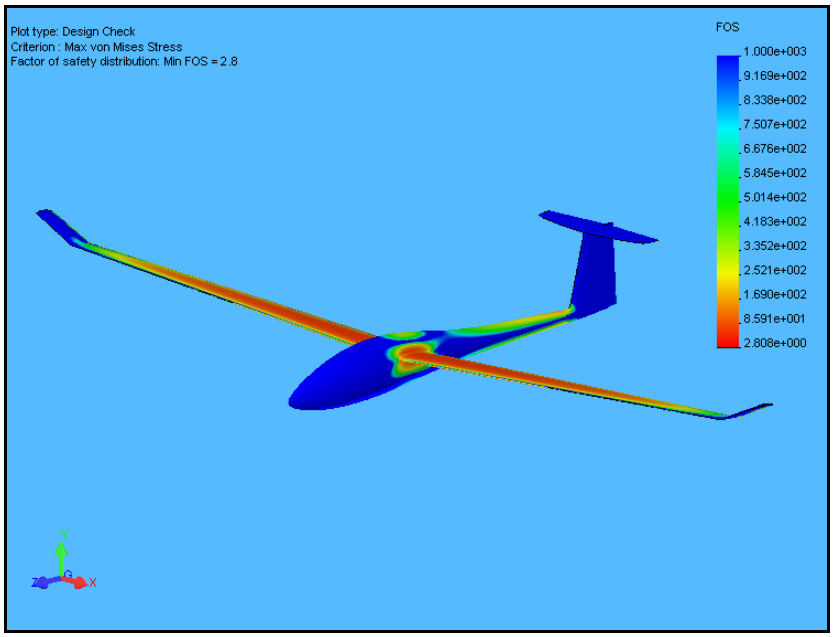

Fig. 7.58: Design Check.

As illustrated in the design check plot (Fig. 7.58) the levels of stress in the critical regions under the aforementioned conditions are still almost three times (FOS 2.8) below that of the material yield. Therefore, it can be concluded that based on the static stress analysis the intended prototype design will suffice for the anticipated operating conditions. For further plots, refer to Appendix F.

7.4.2 Modal Analysis

As was mentioned in the previous chapter a modal analysis was conducted to determine the resonant frequencies of the sailplane structure. While this investigation did not determine the frequencies that the sailplane was likely to incur during flight, it did show the consequences of the resonant frequencies occurring.

The investigation found that should the resonant frequencies occur during flight the sailplane structure would fail to function properly and ultimately lead to structural disintegration. Table 7.18 contains the results for the first five modes.

Table 7.18: First 5 Resonant Frequencies

	Mode 1	***Mode 2***	***Mode 3***	***Mode 4***	***Mode 5***
Frequency	1.5151 Hz	1.9698 Hz	4.6410 Hz	5.7783 Hz	7.3318 Hz

Fortunately, additional research indicates that for a model of this size, resonant frequencies are more likely to occur at levels much lower, typically in the region of 0.1-1 Hz. In addition, any control surface or propulsion device fitted to this structure would resonate at frequencies much higher than those indicated by the first five modes. The following figures visually present the various modal shapes. For further plots, refer to Appendix F.

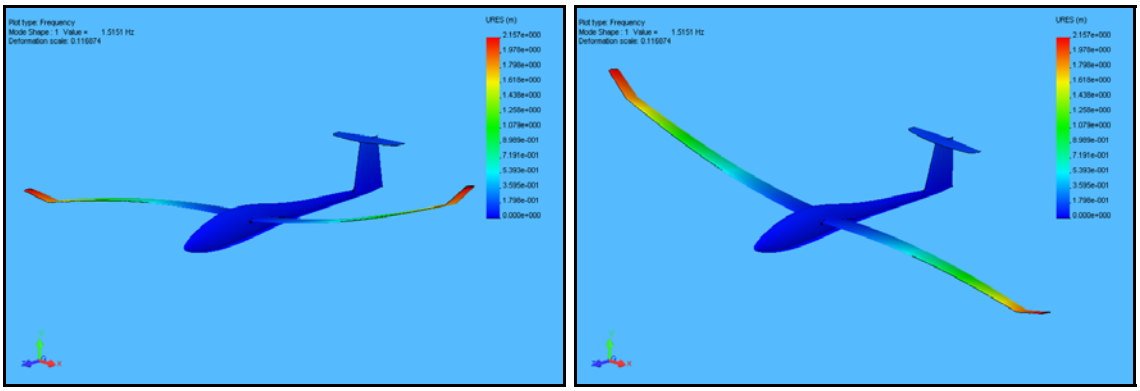

Fig. 7.59: Mode 1 (1.5151 Hz).

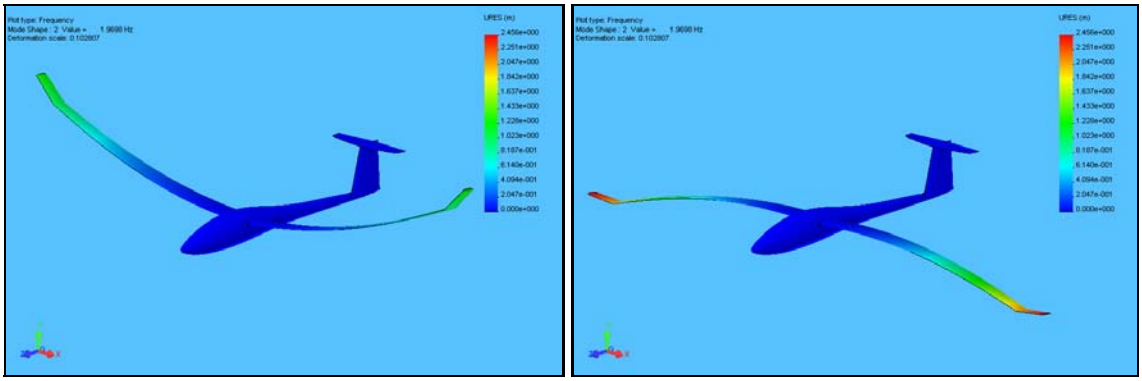

Fig. 7.60:Mode 2 (1.9698 Hz)

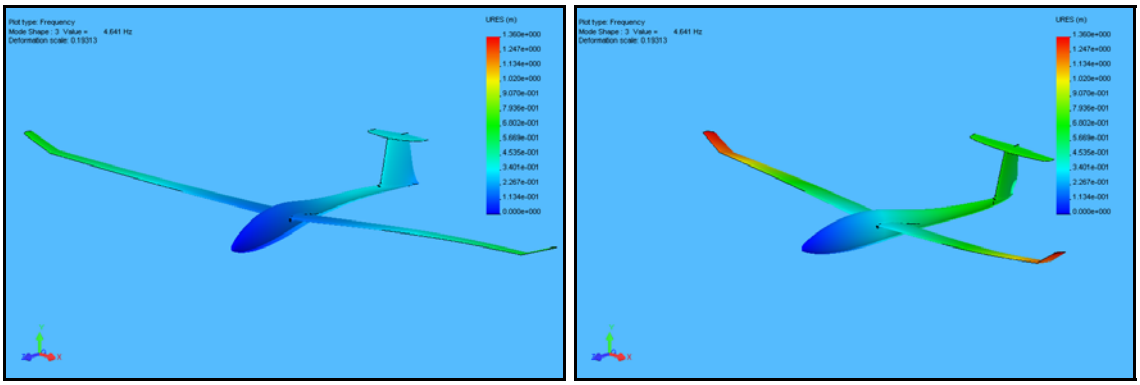

Fig. 7.61: Mode 3 (4.6410 Hz).

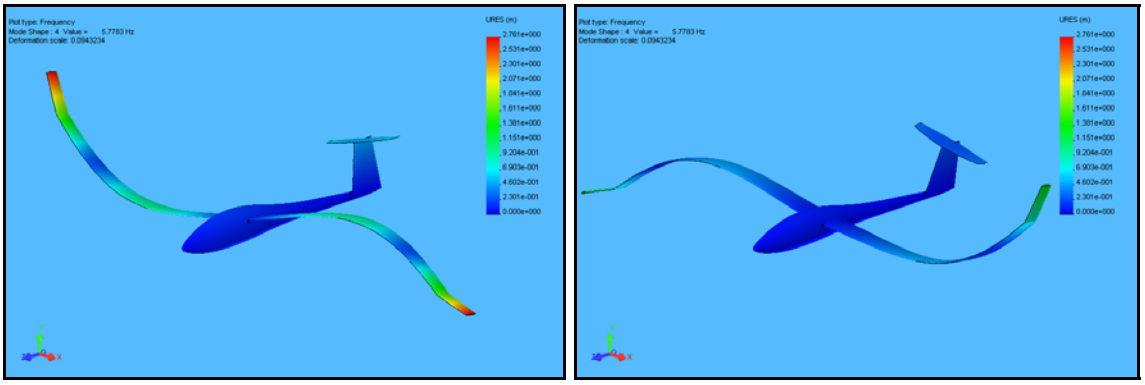

Fig. 7.62: Mode 4 (5.7783 Hz).

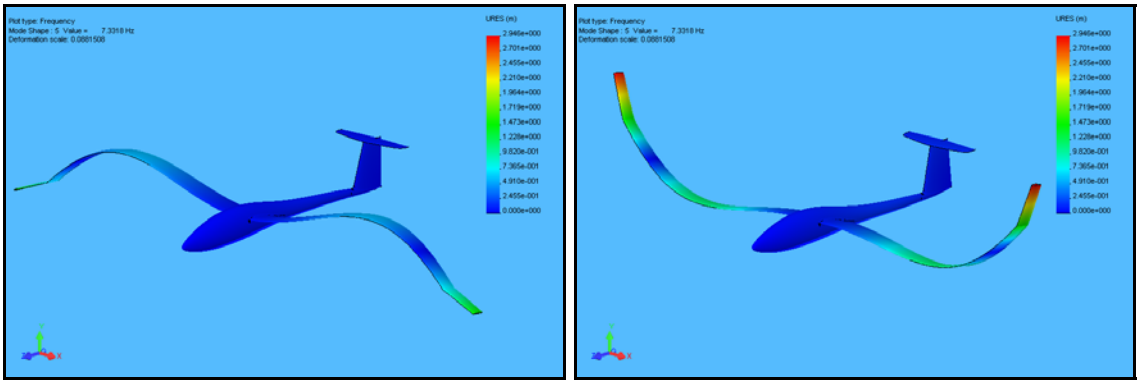

Fig. 7.63: Mode 5 (7.3318 Hz).

7.4.3 Impact Analysis

An impact analysis was conducted in order to determine the locations that may require additional reinforcement in the case of a crash landing. This analysis was conducted at flight velocity of 20 m/s and an impact angle of 45 degrees.

The results indicate that while the point of impact (i.e. the fuselage nose) appeared to incur severe damage, the impact stresses in this region were not substantial enough to cause permeant deformation. These stresses ranged from 0–10 MPa. Of particular interest is the resulting stresses at the wing/fuselage and fuselage/tail junctions. The effects of these stresses, although again not substantial enough to cause permanent damage (0–9.29 MPa), are still magnified in this region as a result of the inherent fuselage geometry (Fig. 7.64). As mentioned in the previous chapter these stresses are an obvious result of the component centre of mass location.

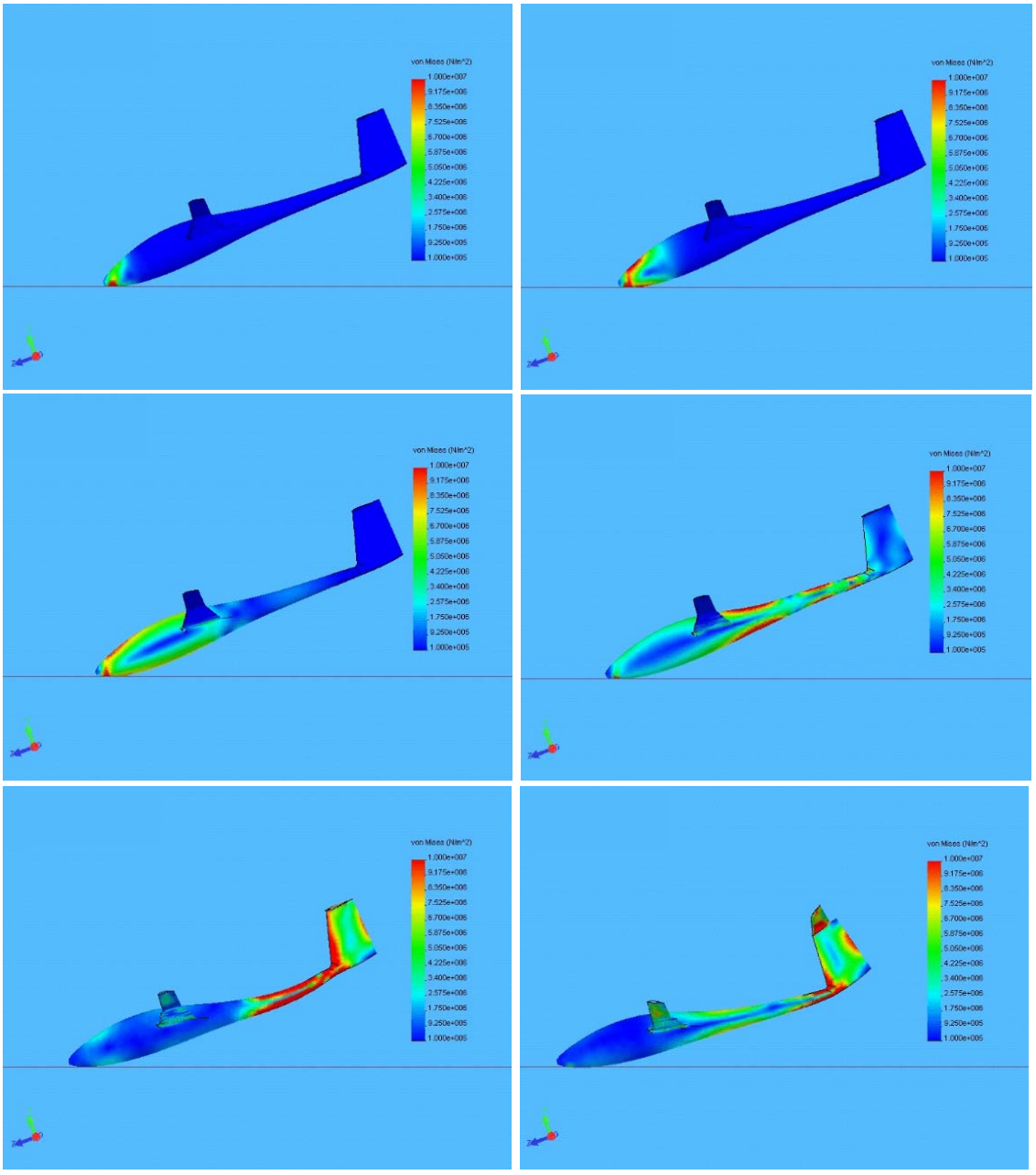

Fig. 7.64: Von Mises Stress throughout Sailplane During Impact.

In addition, Fig. 7.65 illustrates the distribution of stress into both the wings and horizontal stabilizer. This stress causes momentary deflection of both components but fortunately does not result in permeant deformation. For further time step plots, refer to Appendix F.

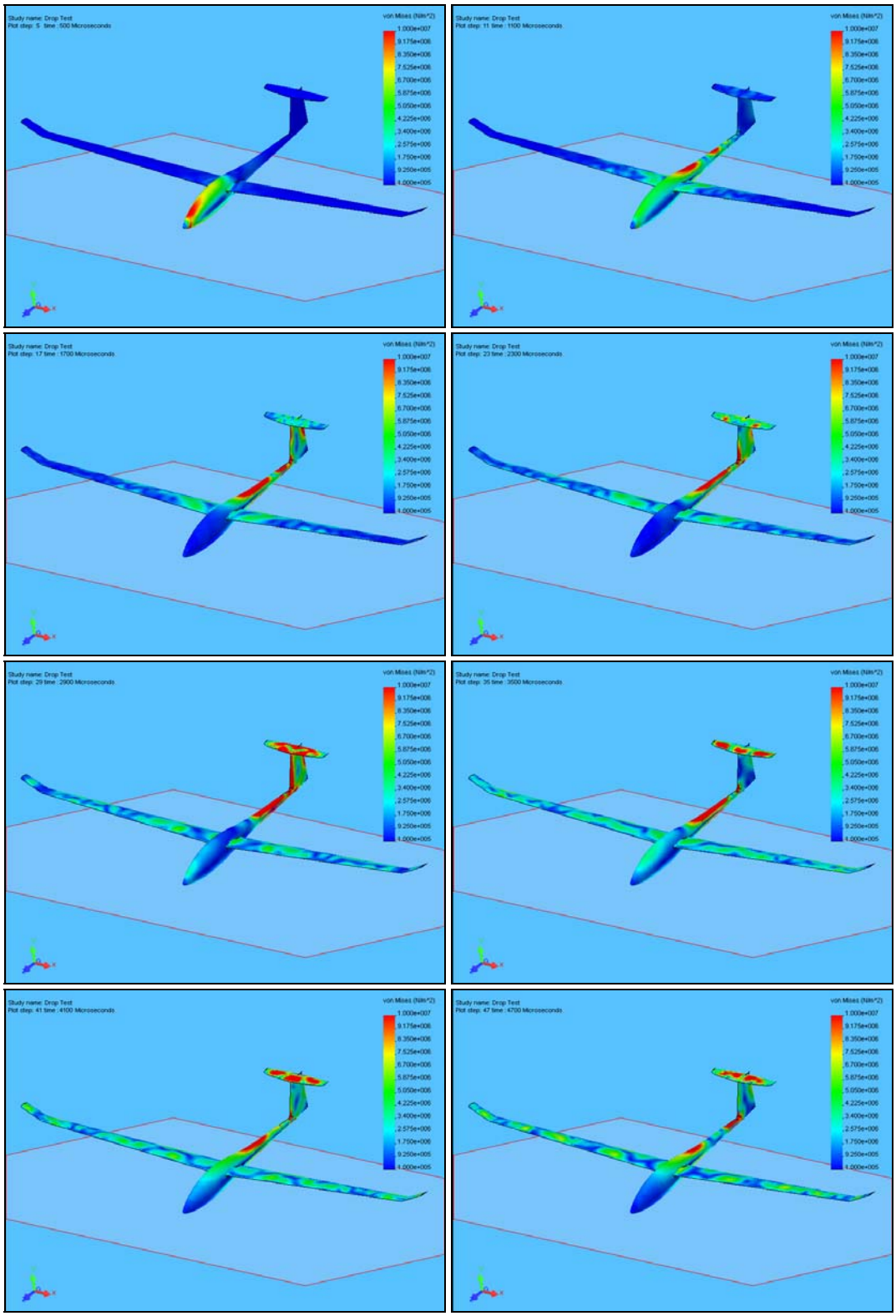

Fig. 7.65: Stress Dispersal into Wings and Horizontal Stabilizer During Impact.

7.4.4 Structural Analysis Summary

The results of the structural analysis illustrated the stresses and deformations associated with both typical and adverse operating conditions. The static analysis showed that the stresses associated with a flight speed of 20 m/s were almost three times below the material yield. This indicates the material type could be changed to reduce the overall weight, and in turn provide greater efficiency without significantly compromising the aircrafts structural integrity. Substantiating this, the impact analysis produced similar results. The impact analysis also indicated that in addition to the impact zone, the wing/fuselage and fuselage/tail junctions sustained significant levels of stress. Therefore, to ensure easy repairability, these areas would be the most appropriate locations for component connection points. Additionally, the results of the modal analysis revealed that the resonant frequencies determined were all well above those expected in flight.

In conclusion, the structural analysis provided greater insight into the aerodynamically optimal design, confirming its functionality in both typical and adverse operating conditions.

Chapter 8

Conclusion

This chapter provides a conclusion to the work undertaken throughout this project and details the achievement of the set objectives. In addition, this chapter presents ideas on the possible future work that maybe undertaken to further enhance the prototype design.

8.1 Achievement of Objectives

This study was initiated with the intent of designing and optimising a prototype sailplane with regard to its aerodynamic efficiency. In addition to the original goal, further studies were undertaken in order to achieve a more "complete" design. These studies included a stability and structural analysis. At the conclusion of this project, both the original and supplementary objectives were fully completed. The final outcomes of this investigation are summarised below.

8.2 Study Outcomes

In short, the results found that the HQ 3510 profile was the most optimal wing airfoil based on the aerodynamic and manufacturability considerations specified. From the three dimensional aerodynamic analysis, two possible optimal wing planforms were determined:

- *Double tapered wing (fixed geometry – 2.5 m span), and*
- *Tapered wing with winglet (varied geometry – 3.1 m span).*

However, when combined with the other sailplane components (i.e. fuselage and tail assembly) the design with the double tapered wing resulted in a marginally lower overall L/D ratio than the design which incorporated the tapered wing with winglet. Because of this, the tapered wing with winglet design was chosen as the most aerodynamically efficient design. Nevertheless, both configurations are valid optimal designs with regard to their respective geometric constraints. That is, the double tapered wing design is the most optimal prototype design with a wingspan of 2.5 m, and the design which incorporates the tapered wing with winglet is the most optimal design with regard to weight. In this way one design is optimised with regard to aerodynamic efficiency and wing span and the other optimised with regard to aerodynamic efficiency and weight. In addition, the NACA 0009 and S9033 profiles were found as the most optimal airfoils for

the horizontal and vertical stabilizers, respectively. Furthermore, the structural analysis found that the intended design could withstand the appropriate aerodynamic loads associated with the expected flight speeds and additionally indicated three potential locations for component connection points (i.e. wing planforms and tail assembly).
The properties of each design can be seen in the following tables and figures.

Table 8.1: Sailplane (Double Tapered Wing)

Body & Wing							Horizontal Stabilizer				Vertical Stabilizer				Aerodynamic				
fuselage length	wingspan, b	aspect ratio, AR	wing area, S	wing loading	root chord	taper ratio	span	area	aspect ratio	mean chord	height	area	aspect ratio	mean chord	wing L/D	aircraft L/D	min. velocity	sink rate	glide angle
(m)	(m)	(-)	(m^2)	(daN/m^2)	(m)	(-)	(m)	(m^2)	(-)	(m)	(m)	(m^2)	(-)	(m)	(-)	(-)	(m/s)	(m/s)	(deg)
1.13	2.5	19.470	0.321	5.45	0.14	0.6	0.375	0.029	5.51	0.08	0.20	0.29	1.36	0.170	12.5	7	10.7	1.7	9.8

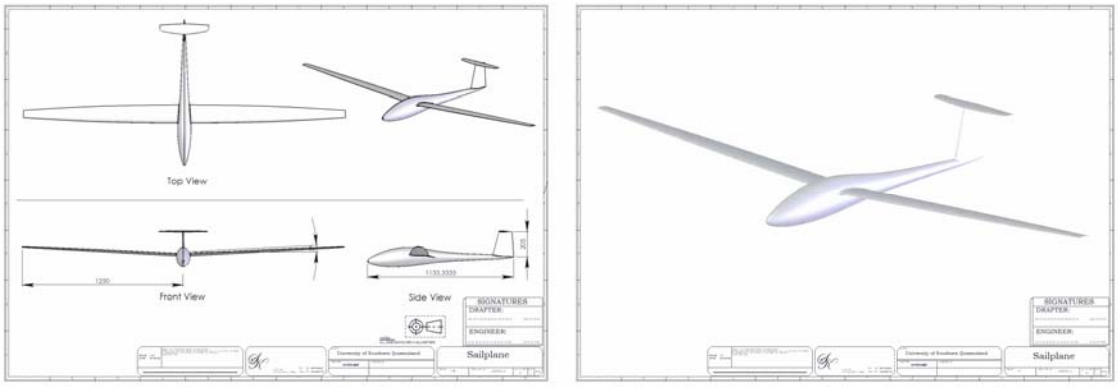

Fig. 8.1: Sailplane (Double Tapered Wing).

Table 8.2: Sailplane (Tapered Wing with Winglet)

Body & Wing							Horizontal Stabilizer				Vertical Stabilizer				Aerodynamic				
fuselage length	wingspan, b	aspect ratio, AR	wing area, S	wing loading	root chord	taper ratio	span	area	aspect ratio	mean chord	height	area	aspect ratio	mean chord	wing L/D	aircraft L/D	min. velocity	sink rate	glide angle
(m)	(m)	(-)	(m^2)	(daN/m^2)	(m)	(-)	(m)	(m^2)	(-)	(m)	(m)	(m^2)	(-)	(m)	(-)	(-)	(m/s)	(m/s)	(deg)
1.13	3.1	24	0.40	4.37	0.17	0.35	0.375	0.029	5.51	0.08	0.20	0.29	1.36	0.170	11.5	7.5	10	1	5.8

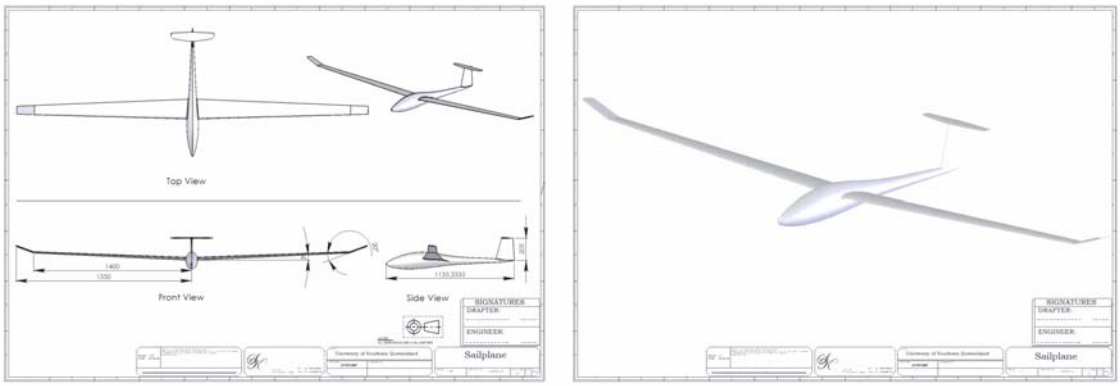

Fig. 8.2 : Sailplane (Tapered Wing with Winglet).

8.3 Recommendations for Future Work

Due to the time limitations associated with this study several additional areas were unable to be investigated in more detail. If investigated, these areas will provide further information to better help represent “real world” conditions and consequently enhance the prototype design both structurally and aerodynamically. These areas include:

- The use of two-way fluid structure interaction (FSI) to determine the likelihood and level of wing flutter
- Variations in flight angle
- Further impact tests with differing prototype orientations.
- Simultaneous design and optimisation of components rather than the step by step process used in this study
- Effects of variations in freestream flow including turbulence and cross-wind prior to prototype interaction.
- Design of control surfaces such as ailerons and rudders.
- Design and optimisation of fuselage and tail assembly
- Construction and wind tunnel testing of prototype
- Formulation of mathematical equation to optimise design with regard to aerodynamic efficiency and geometry.

In addition to the future work that could be undertaken in regard to the prototype, further work could be carried out for other fields. One such field is that of the automotive industry, were the design methods and results of this study may benefit the development of aerodynamic packages.

8.4 Conclusion

The primary objective to design and optimise a prototype sailplane was successfully completed. Towards that objective, a design approach was developed and subsequently carried out through the use of CFD software. The results from the investigation suggest that the final design is highly optimised and capable of sustained flight.

In closing, this investigation proved to be both challenging and interesting throughout its duration. It is hoped that the information contained within this study may aid to the betterment of the aerodynamic field.

References

1. Anderson, J.D.1985, "*Introduction to Flight*", 2nd edition, McGraw Hill.

2. Anderson, J.D. 1991, "*Fundamentals of Aerodynamics*", 2nd Edition, McGraw-Hill, New York.

3. Anderson, R.P. 1993, "*Sailplane Winglet Design Using Non-Linear, Non-Planar Techniques*", Master of Science Thesis, Department of Aerospace Engineering, The Pennsylvania State University, University Park, Pennsylvania.

4. Anderson J.D. 1999, "*A History of Aerodynamics*", University of Maryland, College Park.

5. Drela, M. 1989, "*XFOIL: An Analysis and Design System for Low Reynolds Number Airfoils*", Conference Proceedings on Low Reynolds Number Aerodynamics, Notre Dame, Indiana.

6. Drela, M. 2001, "*XFOIL Subsonic Airfoil Development System*", Massachusetts Institute of Technology, MA [http://raphael.mit.edu/xfoil. Accessed May 27, 2006].

7. Drela, M., Maughmer & Kunz, P., "*Sailplane Winglet Design*", The Pennsylvania State University, University Park, Pennsylvania.

8. Drela, M., Mortara, K. & Maughmer 1993, "*A Method for the Prediction of Induced Drag for Planar and Non-Planar Wings*", AIAA Paper 93-3420.

9. Eppler, R. 1990, "*Airfoil Design and Data*", Springer-Verlag, Berlin.

10. Ferziger J., Peric, M. 1998, "*Computational Methods for Fluid Dynamics*", Springer- Verlag, Berlin.

11. Fox, R., McDonald, A. & Pritchard, P. 2004, "*Introduction to Fluid Mechanics*", John Wiley & Sons, USA.

12. Holighaus, K. 1971, "*The Influence of Planform and Airfoil on the Design of High Performance Sailplane Wings with High Aspect Ratio*", Department of Aerospace Engineering.

13. Hoffstadt, B.A. 1997, "*Analysis and Design of Winglets for Standard-Class Sailplanes*", Master of Science Thesis, Department of Aerospace Engineering, The Pennsylvania State University, University Park, Pennsylvania.

14. Katz, Joseph, Plotkin & Allen 1991, "*Low Speed Aerodynamics: From Wing Theory to Panel Methods*", McGraw-Hill, New York.

15. Kroo, I., & Beckman, E. 1991, "*Development of the SWIFT-A Tailless Foot-Launched Sailplane*", Hang Gliding Jan. 1991.

16. Kuethe A., Chow, C. 1986, "*Foundations of Aerodynamics: Bases of Aerodynamic Design*", 4th Edition, John Wiley & Sons, Canada.

17. Lin, J, & Pauley, L 1996, "*Low-Reynolds-Number Separation on an Airfoil*", AIAA Journal, Vol. 34, No. 8.

18. Lores, M, Burdges, K & Shrewsbury, G 1978, "*Analysis of a Theoretically Optimised Transonic Airfoil*", NASA Contractor Report 3065.

19. Nicolai L.M. 1984, "*Fundamentals of Aircraft Design*", METS, Inc., San Jose, CA.

20. Potkanski, W. 1986, "*Flutter Analysis of Light Aircraft*", Springer Wein.

21. Pamadi, Bandu, N. 1998, "*Performance, Stability, Dynamics, and Control of Airplanes*", American Institute of Aeronautics and Astronautics, Inc, Reston, VA.

22. Raymer, D.P., 1999, "*Aircraft Design: A Conceptual Approach*", 3rd Edition, American Institute of Aeronautics and Astronautics, Reston, VA.

23. Selig M.S. 1995, "*Summary of Low Speed Airfoil Data*", Soartech Publications, VA, USA.

24. Simons, M. 1999, "*Model Aircraft Aerodynamics*", 4th ed., Special Interest Model Books, Dorset, England, UK.

25. Talay, Theodore A. 1975, "*Introduction to the Aerodynamics of Flight*", Scientific and Technical Information Office, National Aeronautics and Space Administration, Washington, D.C. [http://history.nasa.gov/SP-367/cover367.html. Accessed May 15, 2006].

26. Thomas, F. 1984, "*Fundamentals of Sailplane Design*", 2nd ed., Germany.

27. Willat, B. 1988, "*Theory of Glider Flight*".

28. "*A Brief History of Flight*" 2001, San Diego Aerospace Museum Education Department.

29. "*Aerodynamics*", [http://www.centennialofflight.gov. Accessed June 2, 2006].

30. "*Aerodynamics*", [http://www.professionalpilot.ca/aerodynamics.html., Accessed June 2, 2006].

31. "*Airfoil Aerodynamics*", [http://pbs.org/wgbh/nova.html. Accessed May 25, 2006].

32. "*Aerodynamics for Students*", [http://www.aeromech.usyd.edu.au/aero/aerointro.html. Accessed June 2, 2006].

33. "*History of Gliding*", [http://www.solarnavigator.net/inventors.html. Accessed June 2, 2006].

34. "*Gambit 2.2 Online Documentation*" 2006, Fluent Incorporated.

35. "*Fluent 6.2 Online Documentation*" 2006, Fluent Incorporated.

36. "*UIUC Airfoil Coordinates Database*" [http://amber.aae.uiuc.edu/~mselig/ads/coord_database.html. Accessed March 15, 2006].

Appendix A

University of Southern Queensland
Faculty of Engineering and Surveying

ENG 4111/4112 Research Project
PROJECT SPECIFICATION

FOR: SCOTT KRUGER

TOPIC: DESIGN AND OPTIMISATION OF A PROTOTYPE SAILPLANE

SUPERVISOR: Dr. Ruth Mossad

PROJECT AIM: This project seeks to design and optimise prototype sailplane in regard to aerodynamic efficiency.

PROGRAMME: **Issue A, 20th March 2006**

1. Research and document the basics of aerodynamics and flight mechanics including topics such as fluid dynamics, airfoil and wing theories, and aeroelasticity.

2. Conduct a literature review of the design requirements for sailplanes.

3. Commence preliminary conceptual design with particular emphasis on design optimisation based on previous design research including aspects associated with wing design, airfoil selection, wing planform, fuselage design, ailerons and horizontal stabilizers.

4. Review the available software tools for 3d model construction and CFD (Computational Fluid Dynamic) modelling and contrast their capabilities.

5. Generate preliminary design/s using an appropriate 3d modelling package.

6. Conduct computational fluid dynamic analysis using an appropriate CFD package paying particular interest to the L/D ratio.

7. Analyse and discuss the results obtained from the CFD analysis.

8. Based on various factors including CFD analysis and construction simplicity, finalise an appropriate design.

As time permits:

9. Review the available CNC (Computer Numerical Control) milling software and upon selection create and document the computational process.

10. Construct the finalised design using the CNC machine/s available and fabricate and assemble the prototype using the appropriate materials.

Supervisor: …… Student: ……

Appendix B

Numerical Calculations

The following contains numerical calculations pertaining to the fluid dynamic and geometric analysis of the airfoils, wings, fuselage, tail assembly and sailplane.

Units

Quantity	SI Unit	English Unit	Conversion Factor Equalities
Length	millimeter (mm) meter (m)	inch (in. or “) foot (ft or ‘)	1 in. = 0.0254 m 1 ft = 0.3048 m
Area	meter^2 (m^2)	inch^2 (in.^{2})	1 in.^{2} = 0.000645 m^2
Volume	meter^3 (m^3)	gallon (gal U.S.)	1 gal = 0.003785 m^3
Force	newton (N)	pound (lb)	1 lb = 4.448 N
Torque	newton-meter (N·m)	pound-foot (lb·ft)	1 lb·ft = 1.356 N·m
Stress, Pressure	pascal (Pa) megapascal (MPa)	pounds/in.^{2} (psi) thousand pounds/in.^{2} (ksi)	1 psi = 6895 Pa 1 ksi = 6.895 MPa
Mass	kilogram (kg)	lbm	1 lmb = 0.454 kg

Table B1 – Conversion Factors for SI and English Units

Quantity	Name	Symbol
Length	meter (m)	m
Mass	kilogram (kg)	kg
Time	second	s
Acceleration	meter per second squared	m/s^2
Area	square meter	m^2
Density	kilogram per cubic meter	kg/m^3
Energy	joule	J
Force	newton	N
Frequency	hertz	Hz
Moment	newton-meter	N·m
Pressure	pascal	Pa
Velocity	meter per second	m/s
Viscosity	pascal-second	Pa·s
Volume	cubic meter	m^3
Work	joule	J

Table B2 – Common SI Units

Name	Symbol	Factor
giga	G	1 000 000 000 = 10^9
mega	M	1 000 000 = 10^6
kilo	k	1 000 = 10^3
milli	m	0.001 = 10^{-3}
micro	μ	0.000 001 = 10^{-6}

Table B3 – Standard SI Prefixes

Full Size Sailplane

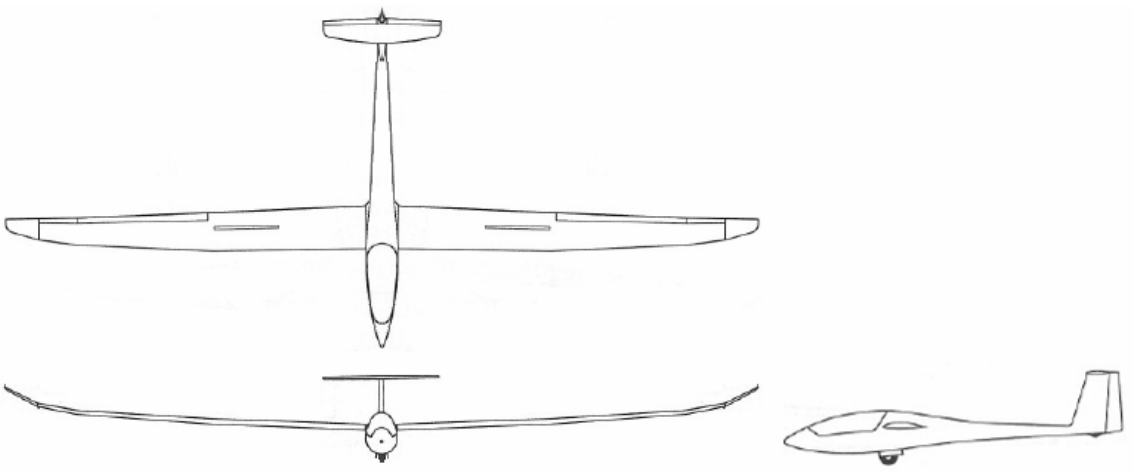

Figure B1 – Full Size Sailplane

Table B4 – Full Size Sailplane Details

Body & Wing							Horizontal Stabilizer				Vertical Stabilizer			
fuselage length	wingspan, b	aspect ratio, AR	wing area, S	wing loading	root chord	taper ratio	span	area	aspect ratio	mean chord	height	area	aspect ratio	mean chord
(m)	(m)	(-)	(m^2)	(daN/m^2)	(m)	(-)	(m)	(m^2)	(-)	(m)	(m)	(m^2)	(-)	(m)
6.81	15/18	22.1	10.16	32.3	0.85	0.27	2.30	0.96	5.51	0.42	1.16	0.99	1.36	0.85

Prototype Sailplane

Scale 1:6

Table B5 – 1:6 Prototype Sailplane Details

Body & Wing							Horizontal Stabilizer				Vertical Stabilizer			
fuselage length	wingspan, b	aspect ratio, AR	wing area, S	wing loading	root chord	taper ratio	span	area	aspect ratio	mean chord	height	area	aspect ratio	mean chord
(m)	(m)	(-)	(m^2)	(daN/m^2)	(m)	(-)	(m)	(m^2)	(-)	(m)	(m)	(m^2)	(-)	(m)
1.13	2.5/3	22.1	0.28	5.38	0.14	0.35	0.375	0.029	5.51	0.08	0.20	0.29	1.36	0.170

Note: The proceeding details are only an approximation of the final prototype and are not necessarily those of the final model.

2D Aerodynamic Calculations

Reynolds Numbers

Table B6 – Reynolds Numbers for Wing Airfoils

	1 m/s	5 m/s	10 m/s	15 m/s	20 m/s
Wing Root (0.143 m)	10 000	48 000	96 000	144 000	192 000
Wing Tip (0.050 m)	3 000	17 000	34 000	51 000	68 000

Table B7 – Reynolds Numbers for Horizontal Stabilizer Airfoils

	1 m/s	5 m/s	10 m/s	15 m/s	20 m/s
H. Stabilizer Root (0.085 m)	6 000	28 000	57 000	85 000	113 000
H. Stabilizer Tip (0.045m)	3 000	16 000	31 000	47 000	62 000

Table B8 – Reynolds Numbers for Vertical Stabilizer Airfoils

	1 m/s	5 m/s	10 m/s	15 m/s	20 m/s
V. Stabilizer Root (0.170 m)	11 000	57 000	113 000	170 000	226 000
V. Stabilizer Tip (0.100 m)	7 000	36 000	71 000	107 000	143 000

Aerodynamic Forces

Parameters

$$F_L = \tfrac{1}{2} C_L \rho V^2 S = W$$

$$\rho = 1.225\, kg/m^3 \qquad S = 0.28\, m^2 \qquad W \approx 1.85\, kg \approx 18.15\, N$$

Note: The proceeding parameters are only approximations of the final prototype and are not necessarily those of the final model.

Airfoil - HQ 3510

@ 1 m/s

$$F_L = \tfrac{1}{2} \times 0.4 \times 1.225 \times 1^2 \times 0.28 = 0.0686N << 18.15N$$

$$F_D = \tfrac{1}{2} \times 0.064 \times 1.225 \times 1^2 \times 0.28 = 0.011N$$

@ 5 m/s

$$F_L = \tfrac{1}{2} \times 0.85 \times 1.225 \times 5^2 \times 0.28 = 3.644N < 18.15N$$

$$F_D = \tfrac{1}{2} \times 0.038 \times 1.225 \times 5^2 \times 0.28 = 0.163N$$

@ 10 m/s

$$F_L = \tfrac{1}{2} \times 1.05 \times 1.225 \times 10^2 \times 0.28 = 18.00N \approx 18.15N$$

$$F_D = \tfrac{1}{2} \times 0.018 \times 1.225 \times 10^2 \times 0.28 = 0.309N$$

@ 15 m/s

$$F_L = \tfrac{1}{2} \times 1.05 \times 1.225 \times 15^2 \times 0.28 = 40.52N > 18.15N$$

$$F_D = \tfrac{1}{2} \times 0.012 \times 1.225 \times 15^2 \times 0.28 = 0.463N$$

@ 20 m/s

$$F_L = \tfrac{1}{2} \times 1.05 \times 1.225 \times 20^2 \times 0.28 = 72.03N >> 18.1485N$$

$$F_D = \tfrac{1}{2} \times 0.011 \times 1.225 \times 20^2 \times 0.28 = 0.755N$$

3D Aerodynamic Calculations

Aerodynamic Forces

Double Tapered Wing (Full Span)

Parameters

$b = 2.5\,m$ $S = 0.321\,m^2$ $AR = 19.470$ $c_\mu = 0.143\,m$

$W \approx 1.85\,kg \approx 18.15\,N$ $\lambda = 1:0.8:0.6$

Note: The proceeding parameters are only approximations of the final prototype and are not necessarily those of the final model.

@ 10 m/s $F_L = 18.33N \approx 18.15N$ $F_D = 1.408N$

@ 15 m/s $F_L = 41.482N > 18.15N$ $F_D = 3.090N$

@ 20 m/s $F_L = 74.282N >> 18.15N$ $F_D = 5.428N$

Minimum Flight Velocity and Sink Rate

$$V_{\min} = \sqrt{\frac{2W}{\rho S C_{L_{\max}}}} = \sqrt{\frac{2\times 18.15}{1.225\times 0.321\times 0.81}} = 10.68\,m/s$$

$$V_s = \frac{C_D}{C_L^{3/2}}\sqrt{\frac{2W}{\rho S}} = \frac{0.13}{0.81^{3/2}}\sqrt{\frac{2\times 18.15}{1.225\times 0.321}} = 1.7134\,m/s$$

Glide Angle

$$\gamma = \tan^{-1}\left(\frac{C_D}{C_L}\right) = 9.118^o$$

Lift-curve Slope

$$\frac{dC_{L_w}}{d\alpha_w} = \frac{2\pi AR}{AR + 2} = \frac{2\pi\times 19.470}{19.470+2} = 5.7$$

Wing Volume

$$V_w = \frac{dC_{L_w}}{d\alpha_w} c_\mu S_w = 5.7\times 0.143\times 0.321 = 0.262$$

Optimised Tapered Wing (Full Span)

Parameters

$b = 3.1\,m$ $S = 0.400\,m^2$ $AR = 24.025$ $c_\mu = 0.150\,m$

$W \approx 1.85\,kg \approx 18.15\,N$ $\lambda = 0.35$

Note: The proceeding parameters are only approximations of the final prototype and are not necessarily those of the final model.

@ 10 m/s $F_L = 19.248N \approx 18.15N$ $F_D = 2.214N$

@ 15 m/s $F_L = 44.328N > 18.15N$ $F_D = 4.552N$

@ 20 m/s $F_L = 79.616N >> 18.1485N$ $F_D = 7.660N$

Minimum Flight Velocity and Sink Rate

$$V_{\min} = \sqrt{\frac{2W}{\rho S C_{L_{\max}}}}$$
$$= \sqrt{\frac{2\times 18.15}{1.225\times 0.400\times 0.73}}$$
$$= 10.07\,m/s$$

$$V_s = \frac{C_D}{C_L^{3/2}}\sqrt{\frac{2W}{\rho S}}$$
$$= \frac{0.074}{0.73^{3/2}}\sqrt{\frac{2\times 18.15}{1.225\times 0.400}}$$
$$= 1.021\,m/s$$

Glide Angle

$$\gamma = \tan^{-1}\left(\frac{C_D}{C_L}\right)$$
$$= 5.788^o$$

Lift-curve Slope

$$\frac{dC_{L_w}}{d\alpha_w} = \frac{2\pi AR}{AR + 2}$$
$$= \frac{2\pi\times 24.025}{24.025+2}$$
$$= 5.8$$

Wing Volume

$$V_w = \frac{dC_{L_w}}{d\alpha_w} c_\mu S_w$$
$$= 5.8\times 0.150\times 0.2$$
$$= 0.174$$

Horizontal Stabilizer

Parameters

$b = 0.375\ m \qquad S = 0.029\ m^2 \quad AR = 4.85 \qquad \ell_H = 0.640\ m$

Lift-curve Slope

$$\frac{dC_{L_H}}{d\alpha_H} = \frac{2\pi AR}{2 + \sqrt{AR^2 + 4}}$$
$$= \frac{2\pi \times 4.85}{2 + \sqrt{4.85^2 + 4}}$$
$$= 4.21$$

Wing Volume

$$V_H = \frac{dC_{L_H}}{d\alpha_H} \ell_H S_H$$
$$= 4.21 \times 0.640 \times 0.029$$
$$= 0.078$$

Recommended Aspect Ratio

$4.5 \le AR_H \le 8$

Vertical Stabilizer

Parameters

$b = 0.2\ m \qquad S = 0.029\ m^2 \quad AR = 1.38 \qquad \ell_V = 0.620\ m$

Lift-curve Slope

$$\frac{dC_{L_V}}{d\beta} = \frac{2\pi AR}{2+\sqrt{AR^2+4}}$$
$$= \frac{2\pi \times 1.38}{2+\sqrt{1.38^2+4}}$$
$$= 1.95$$

Wing Volume

$$V_V = \frac{dC_{L_V}}{d\beta_V}\ell_V S_V$$
$$= 1.95 \times 0.620 \times 0.029$$
$$= 0.035$$

Effective Aspect Ratio

$$AR_{eff} = \frac{AR_{geom}}{K}$$
$$= \frac{1.38}{0.575}$$
$$= 2.4$$

Recommended Aspect Ratio

$$1.5 \le AR_V \le 2$$

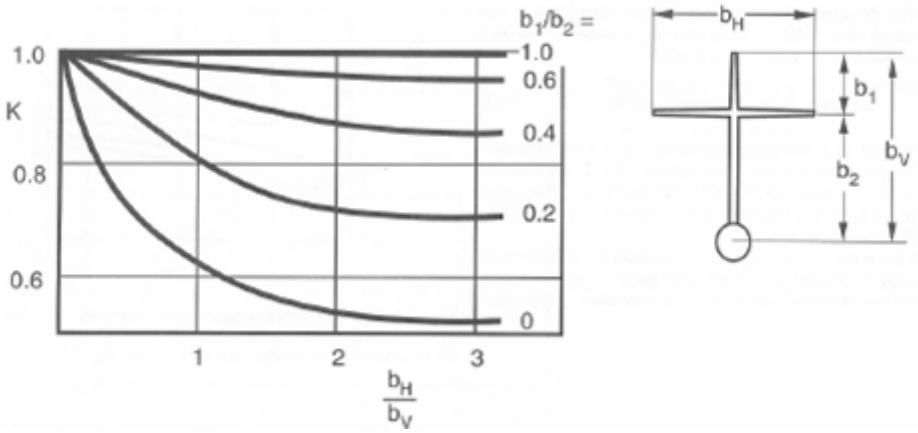

Figure B6 – Increase in Effective Aspect Ratio due to End Plate Effect

Miscellaneous Relationships

Wing/H. Stabilizer Volume

$$\frac{V_H}{V_W} = \frac{0.078}{0.174}$$
$$= 0.448$$

$$0.35 \le V_H / V_W \le 0.55$$

V. Stabilizer/Wing Volume

$$\frac{V_V}{Sb_w} = \frac{0.035}{0.2 \times 3.1}$$
$$= 0.056$$

$$0.045 \le V_V / S_w b_w \le 0.075$$

H. Stabilizer Moment arm

$$\frac{\ell_H}{c_\mu} = \frac{0.64}{0.15}$$
$$= 4.26$$

$$4 \le \ell_H / c_\mu \le 6$$

Stability

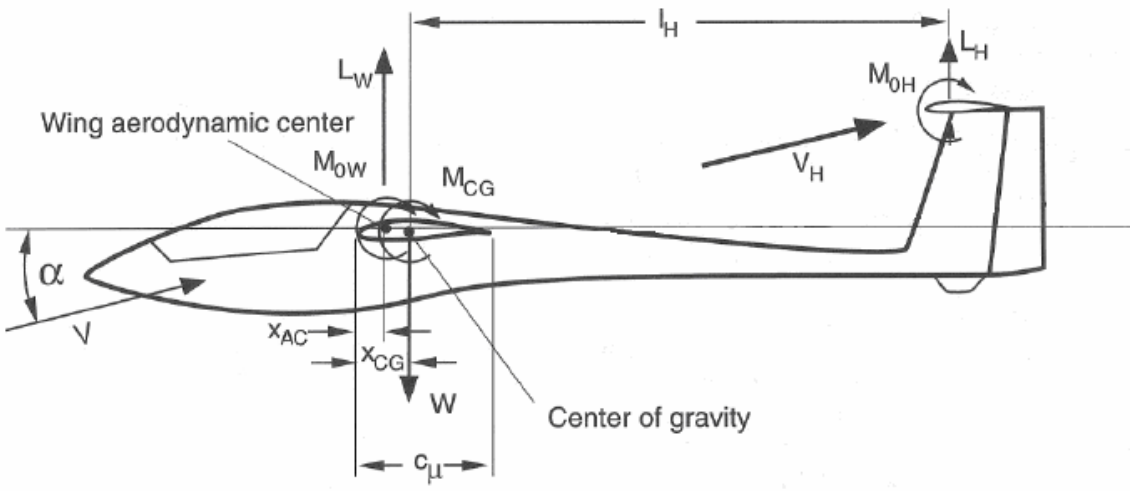

Figure B2 – Force and Moment Definitions for Longitudinal Stability

Static Stability

Stability Margin $\left(x_{CG} - x_N\right)/c_\mu = -0.05$, $\quad \dfrac{x_{CG}}{c_\mu} = 0.5$

$$\sum M_{CG} = L_w\left(x_{CG} - x_{AC}\right) + M_{0w} - M_H = 0 \quad \text{or} \quad C_{L_H}\frac{dC_{L_w}/d\alpha_w}{dC_{L_H}/d\alpha_H}\frac{V_H}{V_W} = C_{L_w}\left(\frac{x_{CG}}{c_\mu} - 0.25\right) + C_{M_{0w}}$$

Horizontal Stabilizer contribution for static stability at 10 m/s

$$\sum M_{CG} = 19.248\left(0.0750 - 0.0375\right) + \left(\tfrac{1}{2} \times -0.07 \times 1.225 \times 10^2 \times \left(0.0750 - 0.0375\right)\right) - \left(0.640 \times L_H\right)$$

$$0 = 0.722 - 0.161 - 0.64L_H$$

$$L_H = 0.877\ N$$

Corresponds to Horizontal Stabilizer at $AOA \approx 6$ deg

Similarly, at 15 m/s and 20 m/s respectively,

$L_H = 2.03\ N$, $\quad AOA \approx 6$ deg

$L_H = 3.660\ N$, $\quad AOA \approx 7$ deg

Therefore, cross referencing with Figures D681 and D684 we see the stabilizer remains in the pre-stall region.

Dynamic Stability

$$C_{L_H}\frac{dC_{L_w}/d\alpha_w}{dC_{L_H}/d\alpha_H}\frac{V_H}{V_W}=C_{L_w}\left(\frac{x_{CG}}{c_\mu}-0.25\right)+C_{M_{0w}}$$

Using the proceeding formula the range for lift coefficient of the horizontal stabilizer for dynamic stability can be found as illustrated below.

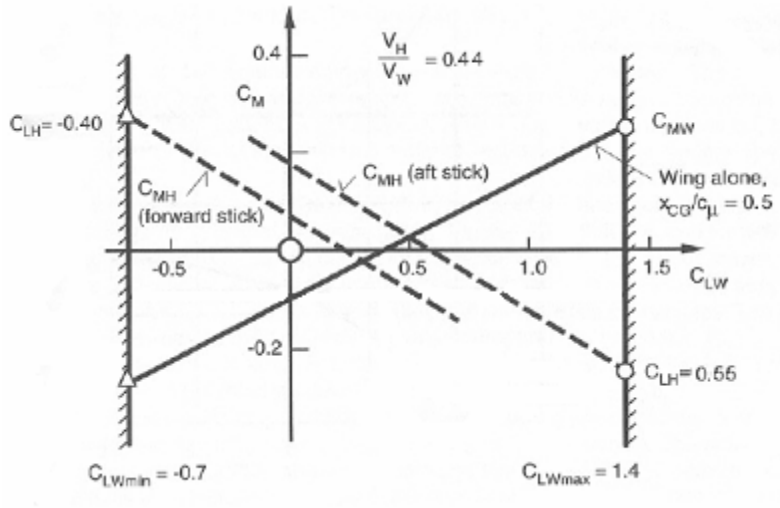

Figure B3 – Equilibrium Conditions for Minimum and Maximum Wing Lift Coefficient

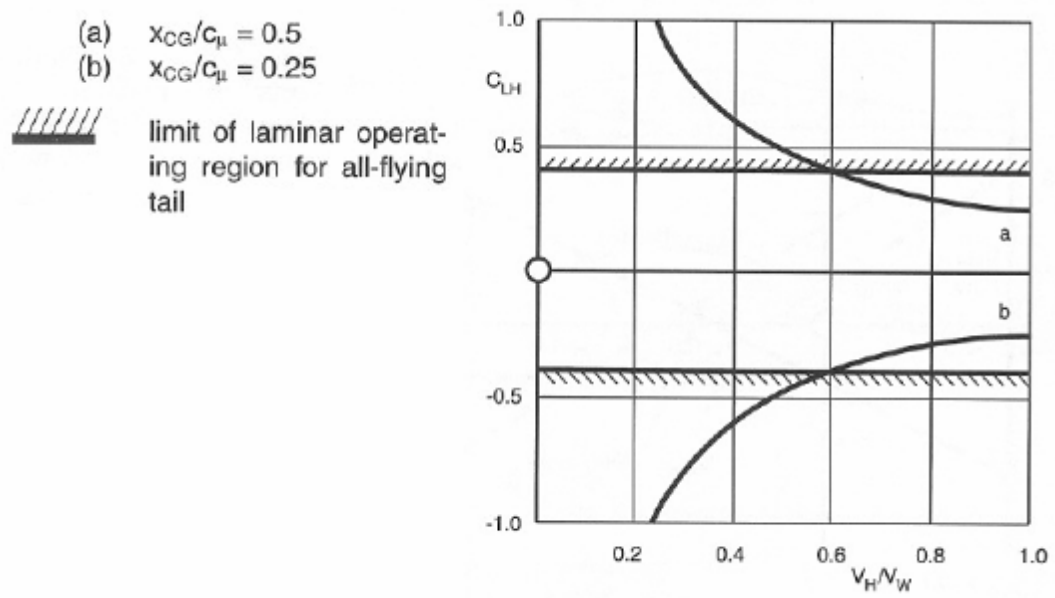

Figure B4 – Required Maximum Stabilizer Lift Coefficient as a Function of Stabilizer Volume

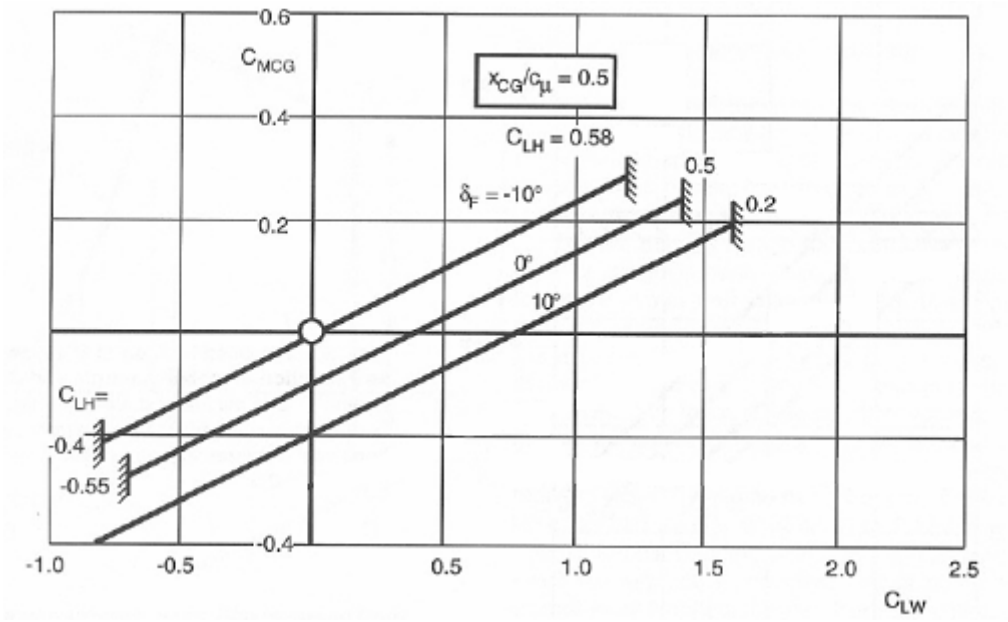

Figure B6 – Pitching Moment Curve for Various Wing Flap Deflections

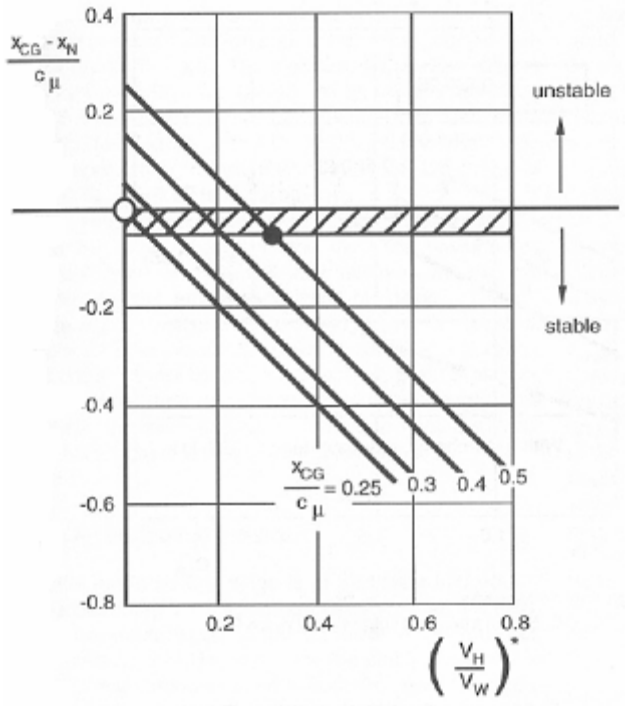

Figure B5 – Minimum Stabilizer Volume as a Function of Stability Margin and CG Location